

# Hundness versus Mottness in a three-band Hubbard-Hund model: On the origin of strong correlations in Hund metals $\star$

K. M. Stadler<sup>a,\*</sup>, G. Kotliar<sup>b</sup>, A. Weichselbaum<sup>a,c</sup>, J. von Delft<sup>a</sup>

<sup>a</sup>Physics Department, Arnold Sommerfeld Center for Theoretical Physics and Center for NanoScience,  
Ludwig-Maximilians-Universität München, 80333 München, Germany

<sup>b</sup>Department of Physics and Astronomy, Rutgers University, Piscataway, NJ 08854, USA

<sup>c</sup>Condensed Matter Physics and Materials Science Department, Brookhaven National Laboratory, Upton, New York 11973,  
USA

---

## Abstract

Hund metals are multi-orbital systems with moderate Coulomb interaction,  $U$ , among charges and sizeable Hund's rule coupling,  $J(< U)$ , that aligns the spins in different orbitals. They show strong correlation effects, like very low Fermi-liquid coherence scales and intriguing incoherent transport regimes, resulting in bad-metallic behavior. But to what extent are these strong correlations governed by Mottness, i.e. the blocking of charge fluctuations close to a Mott insulator transition (MIT) induced by  $U$ , or by Hundness, a new route towards strong correlations induced by  $J$ ? To answer this question, we study the full phase diagram of a degenerate three-band Hubbard-Hund model on a Bethe lattice at zero temperature using single-site dynamical mean-field theory and the numerical renormalization group as efficient real-frequency multi-band impurity solver. Hund metal behavior occurs in this minimal model for a filling close to  $n_d = 2$ , moderate  $U$  and sizeable  $J$ , the "Hund-metal regime". In particular, strong correlations manifest themselves there by an unusually low quasiparticle weight. Generalizing previous results on this model, we show that "spin-orbital separation" (SOS) is a generic Hund's-coupling-induced feature in the whole metallic regime of the phase diagram for  $1 < n_d < 3$  and sizeable  $J$ . There orbital screening always occurs at much higher energies than spin screening below which Fermi-liquid behavior sets in. The low quasiparticle weight can then be directly explained in terms of the Hund's-coupling-reduced Fermi-liquid scale. We carefully analyze the effect of  $J$  (Hundness), and the effect of the MIT at  $n_d = 2$  and  $n_d = 3$  (Mottness) on the energy scales and the nature of SOS. *In the Hund-metal regime, far from any MIT, Hundness – the localization of large spins – is shown to be the key player to induce strong correlations.* There, physical properties are governed by a broad incoherent energy regime of SOS where intriguing Hund metal physics occurs: large, almost unscreened spins are *coupled* to screened orbital degrees of freedom. With increasing proximity to an MIT correlations are further enhanced and the Fermi-liquid scale is further reduced. However, in the Hund-metal regime, this effect of Mottness is minor. In contrast, very close to the MIT at  $n_d = 2$ , the incoherent spin-orbital separation regime is strongly downscaled and becomes negligibly small, whereas Mottness – the localization of charges – becomes dominant in inducing strong correlations. Close to the MIT at  $n_d = 3$ , the SOS regime widens up because the orbital degrees of freedom get blocked by the formation of an  $S=3/2$  impurity spin, but its nature changes: the orbital and spin dynamics get decoupled. Our results confirm Hundness as a distinct mechanism towards strong correlations in the normal state of Hund metals, leading to various interesting implications for the nature of electronic transport.

*Keywords:* Hundness, Hund metal, multi-orbital model, Mott-insulator transition, numerical renormalization group, dynamical mean-field theory

*PACS:* 71.10.Fd, 71.27.+a, 71.30.+h, 75.20.Hr

---

## 1. Introduction and Motivation

### 1.1. Bad-metal superconductors

Iron-based high-temperature superconductors [1, 2] (HTSCs) are “bad metals”. On the one hand, in their superconducting state (with critical temperatures up to 56K [3–5]), they are perfect conductors with dissipationless supercurrents; on the other hand, in their normal state they conduct surprisingly badly. But which fundamental physical mechanism causes this bad-metallic behavior? Interestingly, this bad-metallic behavior is not found in conventional BCS-like superconductors, but it is reminiscent of the unconventional normal state of (doped) cuprate HTSCs. These are known to be strongly correlated and the conventional superconducting mechanism based on electron-phonon coupling is most likely not strong enough to generate their high critical temperatures.

There is firm evidence that strong correlation effects play a key role in iron-based HTSCs, as well. In their paramagnetic phase, these materials exhibit anomalous and bad transport properties that are characterized by very low Fermi-liquid (FL) coherence scales [6–9]. Above the FL scale puzzling non-Fermi-liquid (NFL) behavior [6–17] occurs in a large intermediate (paramagnetic) energy window, typically at or slightly below room temperature, together with poorly screened, large fluctuating local moments, as observed in observed in X-ray emission spectroscopy measurements [18–20]. At higher temperatures, the resistivity reaches unusually large values that exceed the Mott-Ioffe-Regel limit [6, 9]. In accordance, various experiments revealed particularly large mass enhancements [8, 9, 16, 17, 21–28].

### 1.2. Hundness versus Mottness in multi-orbital bad metals

Since the “standard model” of a Fermi liquid in condensed matter theory breaks down in the presence of strong correlations, both the superconducting and the bad-metal normal state are still poorly understood in the iron-based HTSCs. In particular, one widely but controversially debated fundamental question pertains to the origin of strong correlations: is it “Hundness” or “Mottness”?

Cuprate HTSCs are widely considered as doped charge-transfer Mott insulators [29, 30]. Strong correlations arise here due to Mottness: the proximity to a Mott-insulator transition (MIT), i.e. a transition at a critical interaction strength  $U_c$  from an (increasingly correlated) metal to an insulator, which is driven by a large Coulomb repulsion,  $U$ . In theoretical descriptions, the original multi-band electronic structure of cuprates is usually reduced to a low-energy effective (two-dimensional) one-band Hubbard model, such that  $U$  acts only between electrons in one orbital per lattice site and the MIT occurs at half-filling for undoped cuprates.

In contrast, doped *and* undoped iron-based HTSCs are (bad) metallic materials with an effective *multi*-band description that allows for an additional type of interaction: Hund’s rule coupling,  $J$  (Hundness), which favors the alignment of spins in different orbitals on the same (iron) atom and consequently correlates the electron hopping in terms of a non-trivial interplay of orbital and spin degrees of freedom [6, 7, 31]. In iron-based HTSCs and other multi-band materials, the strong correlation effects may thus be caused by either Hundness, or Mottness, or a combination of both.

Therefore, the following question has been raised [7, 32]: what is the role of “Hundness versus Mottness” as origin of strong correlations in multi-orbital bad metals? Here we address this question from a fundamental model-based point of view: we investigate the zero-temperature properties of a toy model, the degenerate three-band Hubbard-Hund model Hamiltonian (3HHM) [7, 31, 33], using single-site dynamical mean-field theory (DMFT) and a highly-efficient multi-band numerical renormalization group (NRG) impurity solver

---

\*K.M.S., A.W., and J.v.D. acknowledge support from the excellence initiative NIM; A.W. was also supported by WE4819/1-1 and WE4819/2-1 until 12/2017 and by US DOE under contract number DE-SC0012704 since. G.K. was supported by National Science Foundation grant DMR-1733071. Author contributions: K.M.S. and G.K. proposed this project; K.M.S. performed the DMFT+NRG calculations; A.W. developed the NRG code and assisted K.M.S. in the initial stages of the DMFT+NRG computation. K.M.S. drafted the manuscript with the help of G.K., A.W and J.v.D.

\*Corresponding author.

*Email addresses:* Katharina.M.Stadler@physik.uni-muenchen.de (K. M. Stadler), kotliar@physics.rutgers.edu (G. Kotliar), weichselbaum@bnl.gov (A. Weichselbaum), vondelft@lmu.de (J. von Delft)

[33–36] to tackle the correlated many-body problem. A central theme of our work is spin-orbital separation (SOS). It was first revealed and argued to be related to anomalous power law behavior for the Matsubara self-energy in Ref. [7], further analyzed using perturbative scaling arguments in Ref. [31], and conclusively established by a detailed DMFT+NRG analysis in Ref. [33]. (For a complementary study, where we focussed on finite-temperature properties not addressed in this paper, see Ref. [37].)

We next summarize the state of research on multi-band models motivating and providing the basis for this article.

## 2. Scope and Aim

### 2.1. Hund metals

For a long time strong electronic correlations in materials have exclusively been associated with the proximity to a MIT evoked by  $U$ , i.e. to the suppression of charge fluctuations. The MIT was extensively studied in one-band systems [38–41], including the cuprate HTSCs. But a MIT also occurs at any integer filling of multi-orbital materials. Examples are various 3d (and 4d) transition metal oxides with the prototypical Mott material  $V_2O_3$  [37, 42–45].

Soon after the discovery of the iron pnictides [1, 2], it was realized that the special multi-orbital character of these HTSCs (and many other strongly correlated materials) allows for a new mechanism towards heavy effective masses: Hundness [6]. This new class of materials was dubbed “Hund metals” [46, 47] and includes multi-orbital materials like iron pnictides and chalcogenides [6, 7, 14, 15, 46–50], as well as various transition metal oxides of the 3d and 4d series, such as ruthenates [7, 47, 51–55]. Hund metals are characterized by rather broad bands leading to sizeable Hund’s coupling strengths compared to only moderate Coulomb interactions, which are strongly screened in these materials due to the large spatial extension of the correlated orbitals [52, 56].

Interestingly, bad-metal behavior can be found in essentially all these Hund metals. Although the importance of Hund’s coupling in realistic materials is increasingly being appreciated there is still an ongoing debate whether Hundness or Mottness is the key player in renormalizing the electron masses of Hund metals. This debate is strongly driven by the fact that, indeed, striking analogies in the (doping-temperature) phase diagrams of cuprate and iron-based HTSCs hint towards a common framework. For instance, in both cases superconductivity emerges in the vicinity of an incoherent metallic regime with NFL properties and unconventional spin dynamics. So, ultimately, understanding the normal state of Hund metals might lead to deeper insights into the superconducting mechanism in HTSCs.

### 2.2. Hund models

A very basic approach to address the issue of “Hundness versus Mottness” in Hund metals is to study the paramagnetic phase diagram of Hubbard-Kanamori-like model Hamiltonians (for a review, see Ref. [47]). These take into account two spin and *multiple* ( $N_c$ ) orbital degrees of freedom, a Coulomb interaction,  $U$ , and, most importantly, a finite ferromagnetic Hund’s coupling,  $J$ . Hund-metal physics is then captured by these models for a filling,  $n_d$ , close to one charge away from half-filling:  $n_d \approx N_c \pm 1$ . This is motivated by the particle-hole asymmetry of real Hund materials. For instance, the average occupancy of the five Fe 3d orbitals is  $d6$  for the undoped stoichiometric parent compounds of almost all iron-based HTSC families [50]. Small to moderate crystal field splittings, as well as hole or electron doping lead to variations in the occupancy, such that the electron densities can range between 5.5 and 6.3 electrons per iron atom [46, 50]. Assuming a fully filled  $e_g$  duplet, this leaves  $n_d \sim 2$  electrons for three active  $t_{2g}$  orbitals. Similarly, ruthenates have an average filling of approximately four electrons in  $t_{2g}$ -orbitals.

Here we study the minimal model [7, 31] with relevance for Hund metals, the 3HHM, presented in Sec. 2.6. It involves three degenerate orbitals. We thus fully neglect any material-specific details like crystal-field splitting or realistic band structures, although undoubtedly present in real materials. Our aim in this study is to focus attention on the most generic aspects of Hundness and Mottness in the maximally simple context of full orbital degeneracy, in order to reveal which many-body effects can be understood on this simple model level and which ones require full information of the electronic structure. Since Hund’s

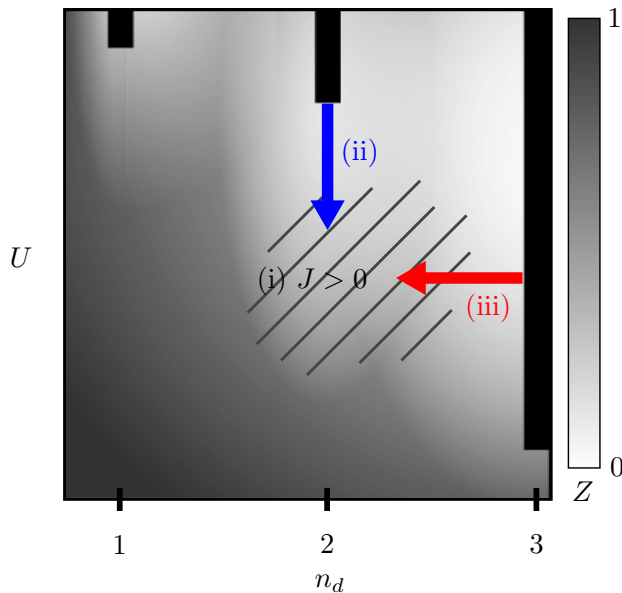


Figure 1: Schematic sketch of the  $n_d$ - $U$  phase diagram for the 3HHM at finite  $J$ . We only show half of the phase diagram, as it is symmetric with respect to half-filling. The shading reflects the quasiparticle (QP) weight  $Z$ . Darker regions (large  $Z$ ) indicate good metallic, lighter regions (small  $Z$ ) bad-metallic behavior. The black bars mark Mott insulating phases. At all integer fillings, a MIT occurs above a (different) critical interaction strength,  $U_c$ . Interestingly, an extended light region exists also at moderate  $U \ll U_c^{(2)}$  around  $n_d = 2$  (and reaches to  $n_d = 3$ ). In this “Hund-metal regime” (hatched area), where most Hund metals can be placed [53], strong electronic correlations might either be induced by Hundness, (i) the presence of sizeable  $J$ , or Mottness, (ii) the influence of the MIT at  $n_d = 2$  (blue arrow), and (iii) the influence of the MIT at  $n_d = 3$  (red arrow), or a combination of these scenarios.

rule coupling is only effective for a site occupation that is larger than one electron (and smaller than one hole), we simulate fillings  $1 < n_d < 3$  with particular emphasis on  $n_d = 2$ . (By the particle-hole symmetry of the model with respect to half-filling, this also describes the fillings  $3 < n_d < 5$ .)

### 2.3. Phase diagram and bad-metal regime

Our work is motivated by the results of various single-site dynamical mean-field theory (DMFT) [47, 51, 53, 57] and slave-boson [32, 50, 58] studies of degenerate three-band Hubbard-Kanamori-type models that reproduced basic Hund metal physics: in the  $n_d$ - $U$  phase diagram at finite  $J$ , they found strongly correlated, bad-metallic behavior in an extended region around a filling of  $n_d = 2$ , which we dub “Hund-metal regime” (hatched area in Fig. 1 at moderate  $U \ll U_c^{(2)}$ ). Naturally, bad-metallic behavior (light regions in Fig. 1) occurs close to the MIT at  $n_d = 2$ , but interestingly, it also ranges down to rather small Coulomb interaction strengths  $U \ll U_c^{(2)}$ , provided that Hund’s coupling  $J$  is sizable (in a sense defined at the end of Sec. 2.6.1). Most Hund metals can be placed there, around one charge away from half-filling and at moderate  $U$ . Further, the bad-metallic regime (light area) also reaches out to the insulating state at half-filling,  $n_d = 3$ , where the MIT develops already at a very low critical interaction strength,  $U_c^{(3)}$ .

Bad-metal behavior manifests itself by a small quasiparticle (QP) weight  $Z$ . Based on a coherent FL QP picture,  $Z$  quantifies the weight of the coherent quasiparticle peak (QPP) of the local spectral function (correlated density of states). Within DMFT and slave-boson methods, the inverse QP weight is equivalent to the electronic mass enhancement,  $Z^{-1} = m^*/m$ , and thus serves as measure for strong electronic correlations. For Hund models with  $N_c > 3$  bands, equivalent regions of low  $Z$  (hatched area) were revealed around all integer fillings  $1 < n_d < N_c$  [32, 47, 58], but they are most prominent at  $n_d = N_c \pm 1$  (see supplement of Ref. [32]).

We note that in the presence of crystal-field splitting  $Z$  and the filling can acquire an orbital dependence: various simulations [7, 11, 12, 32, 46, 48, 59–67] and measurements [8, 9, 17, 27, 28] suggest the occurrence of

orbital differentiation and even orbital selective Mott phases (OSMP), depending on the type and strength of the splitting [64, 67]. In the phase diagram, both effects seem to intensify with increasing  $J$ , increasing  $U$ , and decreasing distance to half-filling. A thorough understanding of the physics of degenerate multi-orbital models is a prerequisite for exploring these effects of orbital selectivity. However, pronounced orbital differentiation is considered to be relevant only for some Hund metals, e.g. for ruthenates. In contrast, for iron-pnictides, it might be less important. In the class of the iron-based HTSCs, only iron chalcogenides are expected to be at the verge of an orbital-selective MIT [46, 61]. Interestingly, many materials with large orbital differentiation are either no superconductors or exhibit only low transition temperatures: indeed, large orbital differentiation is argued to be harmful for superconductivity [46].

#### 2.4. The Hund-metal problem

In principle, three scenarios seem possible to induce strong correlation effects and to lead to the bad-metallic behavior (low  $Z$ ) in the Hund-metal regime (hatched area in Fig. 1) of a 3HHM also sufficiently far way from any Mott insulating state (black bars in Fig. 1):

- (i) Hundness: sizeable  $J$  is the key player to induce strong correlations with considerable electronic mass enhancements.
- (ii) Mottness at  $n_d = 2$ : the interaction-induced MIT at one charge away from half-filling,  $n_d = 2$ , triggers the strong correlations (blue arrow in Fig. 1).
- (iii) Mottness at  $n_d = 3$ : the strong correlations are emanated by the half-filled Mott insulator (red arrow in Fig. 1).

Scenario (i) suggests a new route towards strong correlations: Hundness. Sizeable Hund’s rule coupling,  $J$ , leads to the formation of high-spin states and to the suppression of  $Z$ . It goes back to Ref. [6] and is supported in various publications [7, 15, 33, 37, 46, 47, 52, 53, 55, 68].

Scenario (ii) is not much discussed in the literature, as  $U_c^{(N_c-1)}$  is large while  $U$  has moderate values for Hund metals.

Scenario (iii) is motivated by the cuprate picture of doped half-filled Mott-insulators and advocated by several authors [12, 32, 50, 58]. In this scenario the existence of finite  $J$  would have a subordinate role in correlating the electrons by lowering  $U_{c1}^{(3)}$ .

Although all the model calculations cited above confirmed that strong correlation effects dominate the Hund-metal regime of the phase diagram their origin and nature have been under debate even for this toy model until today, either based on different physical interpretations or just on inconsistent terminology. In particular, scenarios (i)-(iii) have been discussed in the context of (D1) the existence of a spin-freezing phase [51], (D2) the “Janus-faced” influence of Hund’s rule coupling [47, 53, 57], and (D3) various proximity effects of the half-filled MIT [32, 50, 58], such as Hund’s-coupling-induced Fermi-liquid instabilities [58]. In this work we will elucidate the role of another very fundamental effect: (D4) spin-orbital separation (SOS) [7, 31, 33]. We will show that the phenomena (D1), (D2), and (D3) are directly connected to (D4). Based on this insight, we will study scenarios (i)-(iii) by revisiting (D1)-(D3) from the perspective of SOS in Sec. 2.7.

##### (D1) Spin-freezing phase

The so-called spin-freezing phase characterizes the Hund-metal regime in terms of a spin-spin correlation function with an unusually slow (imaginary-time) decay, which does not approach zero but a constant at finite temperature. In this picture, scattering off Hund’s-coupling-induced large composite and very long-lived (or even frozen, static) magnetic moments leads to the incoherent transport behavior.

The spin-freezing scenario was introduced in 2008 in a first (finite-temperature) DMFT study [51] of the  $n_d$ - $U$  phase diagram of a degenerate three-band Hubbard-Kanamori model using a Quantum Monte Carlo (QMC) impurity solver. Later it was extended to (realistic) five-band calculations for iron-pnictides [11, 12, 14, 19] (demonstrating the importance of Hund’s rule coupling and electronic correlations for the formation of local moments in the paramagnetic phase [19]) and to models with crystal-field-splitting [66]

and spin-orbit coupling [69]. In 2015 it led to the proposal of a fluctuating-moment-induced spin-triplet superconducting mechanism for strontium ruthenates and uranium compounds [70].

The transition into the Hund-metal regime was first interpreted as a quantum phase transition from a paramagnetic metallic FL phase (at small  $n_d$  and/or small  $U$ ) to an incoherent metallic NFL phase with frozen local moments (at larger  $n_d$  and/or larger  $U$ ) [51]. Since 2011, the existence of a FL ground state (with fully screened local moments) has been anticipated in the Hund-metal regime and has led to the picture of a spin-freezing crossover at finite temperatures – although the complete decay of the imaginary-time spin-spin correlation function to zero has not been explicitly demonstrated until recently [71], because, in general, QMC solvers do not have access to low enough temperatures [14, 53]. However, a new QMC technique using (super) state-sampling [71] was able to show the FL ground state in the spin freezing-phase for fillings up to  $n_d = 2.63$ .

Spin-freezing has been assumed to originate, in principle, from (i) Hundness. However, similar to  $Z$ , the spin-freezing phenomenon is considered to be strongly doping dependent and is very pronounced in the vicinity of the half-filled Mott insulator [51, 70]. Interestingly, the crossover towards spin-freezing near  $n_d = N_c - 1$  is characterized by a steep drop of  $Z$  as a function of  $n_d$ . A detailed quantitative analysis if and how the spin-freezing phenomenon is connected to  $Z$ , induced by (i) Hundness and/or influenced by Mottness of kind (ii) or (iii) has not yet been performed. One reason for this is that the mass enhancement could only be computed in an approximate manner because the QMC solver did not reach the FL regime [70]. Further, data was only available on the imaginary Matsubara frequency axis.

#### *(D2) Janus-faced influence of Hund’s rule coupling*

The “Janus-faced” influence of Hund’s rule coupling was a major result of a first more detailed DMFT+QMC study of the phase diagram of the degenerate three-band Hubbard-Kanamori model [47, 53, 57] (including a realistic classification of various 3d and 4d transition metal oxides via their mass enhancements). A detailed exploration in terms of the QP weight,  $Z$ , revealed that Hund’s coupling induces apparent conflicting tendencies at  $n_d = 2$ . On the one hand, increasing  $J$  promotes metallicity by shifting the critical interaction strength,  $U_c^{(2)}$ , of the MIT at  $n_d = 2$  to higher values. On the other hand, at moderate  $U$ , increasing  $J$  reduces  $Z$ , supporting scenario (i) that Hund’s-coupling-induced strong correlations lead to bad-metallic behavior far from a Mott phase. Together, this Janus-faced behavior results in an interesting MIT for sizeable  $J$  upon increasing  $U$  that is qualitatively different from the MIT of one-band and multi-band Hubbard models without Hund’s coupling: starting from a weakly correlated metal at small  $U$ , the system first evolves into a strongly correlated metal which is stable for an extended range of  $U$  values and characterized by very small  $Z$ , before it eventually reaches the Mott insulating phase at large  $U_c^{(2)}$ .

The degenerate three-band study of Refs. [53, 57] was followed by similar analyses for up to five bands, both with [32, 47, 58] and without [58, 60, 63, 72] orbital degeneracy, revealing qualitatively similar behavior as in the three-band case. For degenerate models, Janus-faced behavior emerges for any integer filling away from single and half-filling.

But even for the degenerate three-band model the origin of the Janus-faced behavior has not been fully revealed. Obviously both the QPP itself and the opening of the insulating Mott gap are affected at the same time by changing  $J$ . Previous studies [47, 50, 53, 57] quantified these changes by performing a Hubbard-I-type analysis for the gap dependence and by calculating  $Z$  to characterize the QPP. However, without access to (reliable) real-frequency spectral data, the Hubbard-I predictions could never be explicitly verified and the physical origin of the low  $Z$  could only be speculated about. A connection to the low coherence scale in Hund metals was assumed but never proven, and the nature of the incoherent regime remained unclear. Although considered, a clear connection between spin-freezing and the Janus-faced behavior has not yet been demonstrated. Moreover, we note that the value of  $Z$  can have an error of up to 10% in these DMFT+QMC simulations (see supplement of Ref. [53]), also strongly affecting the values of  $U_c$ .

We therefore conclude that both scenarios (i) and (ii) should be revisited. In particular, the Janus-faced behavior has to be disentangled by identifying a measure for Mottness (ii) which does not change with  $J$ , in order to study the pure effect of Hundness (i), and to analyze the difference in nature between strongly correlated Hund metals at moderate  $U$  and strongly-correlated systems close to the MIT. Scenario (iii) will

be considered in the context of (D3).

*(D3) Proximity to the half-filled MIT*

At half-filling,  $n_d = 3$ ,  $U_c^{(3)}$  is strongly reduced. The region of low  $Z$  in Fig. 1 directly starts at the border of the MIT at  $n_d = 3$  and extends, even at moderate  $U$ , from there to  $n_d = 2$  with  $Z$  slightly increasing when passing from  $n_d = 3$  to  $n_d = 2$ . Such a filling-dependence is observed in simulations and experiments of iron-based superconductors: their correlations are enhanced with hole-doping (i.e. approaching half-filling) [19, 27, 65, 73, 74]. Furthermore, also the spin-freezing phenomenon [51] is strongly doping dependent: the spin freezing phase occurs in the vicinity of the half-filled MIT.

Motivated by this behavior it has been argued in Refs. [32, 50, 58] that the suppression of  $Z$  around  $n_d = 2$  at moderate  $U$  is connected to the MIT at half-filling,  $n_d = 3$ . In particular, the effect of suppressing intra-orbital double occupancy by  $J$  has been regarded as a direct link to the MIT at  $n_d = 3$  [32]. However, it has been noted that in contrast to the one-band Hubbard model, the reduction of  $Z$  in Hund metals does not imply the general suppression of charge fluctuations (far from the MIT, as shown in Ref. [37]) and  $Z$  is thus not a good measure for the latter: the origin of low  $Z$  and its filling dependence is subtle. Again, DMFT+NRG real frequency data can help to further investigate this issue by complementing the slave-boson approaches of Refs. [32, 50] and quantitatively revealing the connection between spin-freezing and  $Z$ .

We note that for non-degenerate models, low  $Z$  is argued to be induced by the ‘‘proximity to a half-filled MIT’’, as well, but here, the half-filled MIT denotes an orbital selective Mott transition: when an orbital is individually half-filled it can become insulating, independently of the other orbitals [65]. This orbital decoupling effect is enhanced by Hund’s coupling, but will not be discussed further in this work.

In a slave-boson study [58] of degenerate and non-degenerate multi-band Hund models, a zone of negative compressibility,  $\kappa_{\text{el}} = \frac{\partial n_d}{\partial \mu} < 0$ , is observed at zero temperature for nonzero  $J$  in the  $n_d$ - $U$  phase diagram, above  $U \geq U_c$ , reaching (depending on  $N_c$ ) from half-filling towards  $n_d = N_c + 1$ . The transition from  $\kappa_{\text{el}} > 0$  to  $\kappa_{\text{el}} < 0$  is realized through a divergence of the compressibility, which occurs in the phase diagram together with a strong reduction in  $Z$ . In the absence of symmetry breaking in the model, this divergence is interpreted as a genuine thermodynamic Hund’s-coupling-induced instability towards a phase separation. The enhancement of  $\kappa_{\text{el}}$  has even been argued to be directly connected to the enhanced critical  $T_c$  of HTCS [57–59, 64]. This strong statement of a negative compressibility is solely the result of slave-boson approaches (rotationally invariant form of the Kotliar-Ruckenstein slave-bosons for the full Hubbard-Kanamori model involving two bands, and slave-spin mean-field approximation for the Hubbard-Kanamori model without spin flip and pair hopping term involving up to five bands). It has so far not been validated by another (zero-temperature) method.

In order to investigate if the suppression of  $Z$  in the Hund-metal regime is mediated by the MIT at half-filling and to check if a negative compressibility is a generic Hund’s-coupling-induced effect (i.e. independent of details of the model and the method), we will also study scenario (iii), the effect of the MIT at  $n_d = 3$  on  $Z$  and  $\kappa_{\text{el}}$ .

*(D4) Spin-orbital separation (SOS)*

Besides the phenomena (D1), (D2), and (D3), also a Hund’s-coupling-induced coherence-incoherence crossover with increasing temperature has been discussed as a new and generic normal state property of Hund metals in the literature [6, 7]. Further an incoherent frequency regime with anomalous power-law exponents in the Matsubara self-energy was revealed for  $1.5 \lesssim n_d \lesssim 2.5$ , which is most pronounced at  $n_d = 2$  [7, 51]. The incoherent temperature and frequency regime was proposed to be induced by two degrees of freedom that behave in different ways: the orbital degrees of freedom are quenched and fluctuate very rapidly while the spin degrees of freedom are unquenched and fluctuate albeit slowly (accordingly the local spin susceptibility has Curie-Weiss form and a large static value) [7, 37]. An analytic RG analysis in the Kondo regime [31] provided a simple understanding of the origin of the incoherent regime and established how the Kondo scales depend on the representations of the spin and orbital operators.

However, still, several issues needed to be clarified: in particular, the DMFT+QMC calculations could not reach sufficiently low temperatures to fully reveal the FL phase. To settle this issue, zero- (and finite-)

temperature, real-frequency DMFT+NRG calculations were performed in 2015 in Ref. [33] for the 3HHM of Eq.(1) at  $n_d = 2$ . These calculations clearly confirmed that, at zero temperature, finite Hund’s coupling leads to SOS [see Fig. 13(a)] – a two-stage screening process, in which orbital screening occurs at much higher energies than spin screening – thus strongly reducing the coherence scale below which a FL ground state is formed. Importantly, at intermediate energies above the coherence scale, a broad incoherent regime opens up involving screened, delocalized orbitals which are non-trivially coupled to almost unscreened, large, localized spins. The incoherent frequency regime is strongly particle-hole asymmetric and displays approximate power-law behavior in the self-energy for positive real frequencies only, leading to apparent fractional power laws on the imaginary Matsubara axis. SOS also occurs in pure impurity calculations without DMFT self-consistency. With increasing temperature, SOS in frequency space translates to a coherence-incoherence crossover for temperature-dependent quantities. Only recently, this two-stage crossover was confirmed in realistic DFT+DMFT+QMC simulations of the temperature dependence of the thermopower, entropy [55] and the local spin and orbital susceptibilities [37] for  $\text{Sr}_2\text{RuO}_4$ . SOS is thus considered to be relevant not only for degenerated toy models but also for realistic Hund materials featuring tetragonal crystal-field splitting of the  $t_{2g}$  orbitals.

However, in Ref. [33] SOS was studied only at  $n_d = 2$  for a small set of parameters  $U$  and  $J$ , which (as will be shown in Fig. 6) lie at the border of the coexistence region of the phase diagram, thus close to the MIT. Therefore many open questions remained: Is SOS a generic phenomenon of Hund metals? Where does it occur in the phase diagram and how is it influenced by  $J$  and the proximity to the MIT at  $n_d = 2$  and  $n_d = 3$ ? How is it connected to the phenomena of (D1)-(D3) and how to the low  $Z$  in the Hund-metal regime? And most importantly, what is the origin of SOS, scenario (i), (ii), or (iii), or a combination of these?

### 2.5. Aim of this paper

The aim of this work is to identify the origin of strong correlations in the Hund-metal regime of the 3HHM, based on real-frequency data, and to develop from this a global, unified and consistent scenario for strong correlation effects in Hund metals. For this we study scenarios (i)-(iii), i.e. “Hundness versus Mottness”, by scanning the full phase diagram of the 3HHM at zero temperature, using DMFT+NRG. In DMFT the lattice model (the 3HHM) is mapped self-consistently onto a quantum impurity model [the Anderson-Hund model (AHM) of Eq. (A.1)], which we solve with NRG, a powerful *real-frequency* multi-band impurity solver. NRG is well suited for the investigation of Hund and Mott physics as it both reveals the spectral properties of Hund metals down to its very low coherence scales and still captures the main features of the Hubbard side bands. We thus provide, for the first time, detailed and *unbiased* real-frequency spectral data in a large parameter space of the phase diagram instead of only measuring the strength of strong correlations by analyzing the behavior of  $Z$ , as done in previous studies [32, 47, 53, 57]. This allows us to reveal the origin of those correlations and the physical nature of the incoherent regime in Hund metals.

The paper is structured as follows. In Sec. 2.6 we give a detailed description of our model and discuss its local multiplet level structure at  $n_d = 2$  (in particular its dependency on  $J$ ) and at  $n_d = 3$ . The DMFT+NRG method is introduced in Appendix A. In Sec. 2.7 we present our main insights: we will show that the low  $Z$  in the Hund-metal regime results directly from the suppression of the coherence scale due to SOS. SOS therefore forms the basis of our main study and scenarios (i)-(iii) will be investigated from that perspective. In particular, we follow a three-fold approach in Sec. 2.7. We revisit (D1) the spin-freezing phase in Sec. 3, (D2) the Janus-faced influence of Hund’s rule coupling in Sec. 4, and the influence of (D3) the MIT at half-filling in Sec. 5, and explain these aspects step by step within the SOS framework.

### 2.6. Model and Methods

For our 3HHM we use the Hamiltonian of Refs. [7, 31, 33, 37] in the form



$$\hat{H}_{\text{HHM}} = \sum_i \left( -\mu \hat{n}_i + \hat{H}_{\text{int}}[\hat{d}_{i\nu}^\dagger] \right) + \sum_{\langle ij \rangle \nu} t \hat{d}_{i\nu}^\dagger \hat{d}_{j\nu}, \quad (1a)$$

$$\begin{aligned} \hat{H}_{\text{int}}[\hat{d}_{i\nu}^\dagger] &= U \sum_{\langle m \rangle} \hat{n}_{im\uparrow}^\dagger \hat{n}_{im\downarrow} + (U - J) \sum_{m \neq m'} \hat{n}_{im\uparrow}^\dagger \hat{n}_{im'\downarrow} + (U - 2J) \sum_{m < m', \sigma} \hat{n}_{im\sigma}^\dagger \hat{n}_{im'\sigma} \\ &- J \sum_{m \neq m'} \hat{d}_{im\uparrow}^\dagger \hat{d}_{im\downarrow} \hat{d}_{im'\downarrow}^\dagger \hat{d}_{im'\uparrow} \end{aligned} \quad (1b)$$

$$= \frac{1}{2} \underbrace{\left( U - \frac{3}{2}J \right)}_{\equiv \tilde{U}} \hat{n}_i (\hat{n}_i - 1) - J \hat{\mathbf{S}}_i^2 + \frac{3}{4} J \hat{n}_i. \quad (1c)$$

This is a minimal version of the generalized Kanamori Hamiltonian of Ref. [47], with  $U(1)_{\text{ch}} \times SU(2)_{\text{sp}} \times SU(3)_{\text{orb}}$  symmetry for its charge (ch), spin (sp) and orbital (orb) degrees of freedom.  $\hat{d}_{i\nu}^\dagger$  creates an electron on site  $i$  of flavor (fl)  $\nu = (m\sigma)$ , which is composed of a spin ( $\sigma = \uparrow, \downarrow$ ) and an orbital ( $m = 1, 2, 3$ ) index.  $\hat{n}_{i\nu} \equiv \hat{d}_{i\nu}^\dagger \hat{d}_{i\nu}$  counts the electrons of flavor  $\nu$  on site  $i$ .  $\hat{n}_i \equiv \sum_\nu \hat{n}_{i\nu}$  is the total number operator for site  $i$  with  $n_d \equiv \langle \hat{n}_i \rangle$ , and  $\hat{\mathbf{S}}_i$  its total spin, with components  $\hat{S}_i^\alpha = \sum_{m\sigma\sigma'} \hat{d}_{im\sigma}^\dagger \frac{1}{2} \sigma_{\sigma\sigma'}^\alpha \hat{d}_{im\sigma'}$ , where  $\sigma^\alpha$  are Pauli matrices. We study a Bethe lattice with degenerate bands, each of bandwidth  $W = 4t$ , i.e we assume negligible crystal field splitting and a uniform hopping amplitude  $t$  restricted to nearest-neighbor hopping between the same kind of orbital and spin degrees of freedom. Both the chemical potential  $\mu$  and the hopping amplitude  $t$  are then equal for all flavors, leading to a locally  $SU(6)_{\text{fl}}$  symmetric kinetic term in Eq. (1a).  $t = 1$  serves as energy unit.

The onsite interaction term,  $\hat{H}_{\text{int}}$ , incorporates Hund's rule and Mott physics in its most basic form and reduces the symmetry to  $SU(2)_{\text{sp}} \times SU(3)_{\text{orb}}$  for  $J > 0$ . It was first introduced by Dworin and Narath in a generalization of the Anderson impurity model to study magnetic impurities [75]. The first three terms of Eq. (1b) are density-density interactions.  $U$  is the intraorbital Coulomb interaction between electrons with opposite spins in the same orbital,  $U - J < U$  the interorbital Coulomb interaction between electrons with opposite spins in different orbitals, and  $U - 2J$  the Coulomb interaction between electrons with parallel spins in different orbitals, where the interorbital Coulomb interaction is further reduced by the ferromagnetic coupling  $J$  due to Hund's first rule that favors the alignment of spins. The last term of Eq. (1b) is a spin exchange term.

The generalized Kanamori Hamiltonian of Ref. [47] involves some additional terms not present in Eq. (1), which reduce the  $SU(3)_{\text{orb}}$  symmetry in the orbital sector to  $SO(3)_{\text{orb}}$ . However, these additional terms do not affect the low-energy physics, since they are irrelevant in a renormalization group sense [76].

Eq. (1c) is a more compact notation of Eq. (1b) and summarizes the two main aspects of our model. The first term is known to trigger Mott physics, whereby  $U$  penalizes double occupancy of orbitals. The second term directly reflects Hund's first rule: it favors a large spin per site for  $J > 0$ . Note that the third term only shifts the chemical potential,  $\mu$ .

We choose  $\mu$  such that we obtain a total filling per lattice site,  $n_d = \langle \hat{n}_i \rangle$ , of  $1 \leq n_d \leq 3$ . For  $n_d > 1$ , Hund's first rule reduces the atomic ground state degeneracy and thus strongly influences the physics of the system. The orbital and spin degrees of freedom of electrons can show very distinct behavior and conspire in a highly non-trivial way, leading to striking new phenomena like spin-orbital separation [33]. In contrast, at half-filling,  $n_d = 3$ , a fundamentally different ground state emerges: a large spin state is formed and orbital degrees of freedom are fully blocked [47].

We treat the 3HHM of Eq. (1) with single-site DMFT and use full-density-matrix (fdm)NRG [34] as real-frequency impurity solver. For methodological details and further definitions of physical quantities used in the main paper, see Appendix Appendix A.

### 2.6.1. Multiplet structure at filling $n_d = 2$

The physical behavior of the system depends in a crucial manner on the multiplet structure of the local Hamiltonian, and can change in dramatic ways when parameters are tuned such that level crossings occur [77]. This section is therefore devoted to a detailed discussion of this multiplet structure.

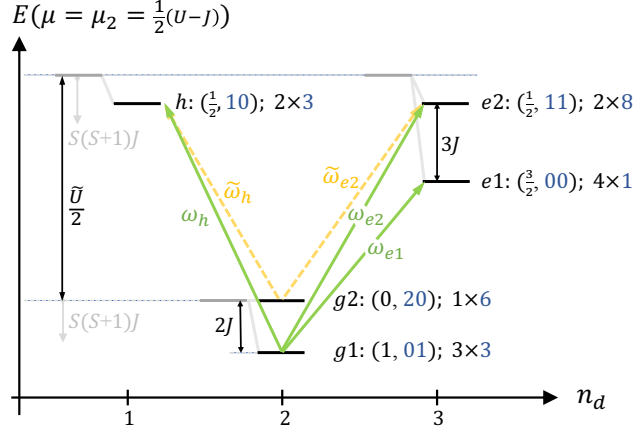


Figure 2: Local multiplet structure of a single 3HHM site at filling  $n_d = 2$  using  $\mu = \mu_2$ , with  $\tilde{U} \equiv U - \frac{3}{2}J$  as specified in Eq. (2). The energies for  $J = 0$  are indicated by the thick grey levels, which are split when turning on  $J$  as indicated. The individual multiplets are given labels  $g$  for “ground state”,  $h$  for hole-like, and  $e$  for electron (particle) like, which are specific to the current filling, here  $n_d = 2$ . Each multiplet is followed by its symmetry labels  $(S, q)$  and the combined multiplet dimension of spin times SU(3), with the SU(2) spin  $S$  and SU(3) representation  $q \equiv (q_1, q_2) \equiv (q_1 q_2)$ . The grey downward arrows indicate a lowering of the energy levels by the Hund’s term  $-J\hat{\mathbf{S}}_i^2$ . The shown multiplet structure is complete for  $n_d = 1, 2, 3$ . Together with the vacuum state at  $n_d = 0$  and the symmetry relative to half-filling, this yields a total number of states (relative to  $n_d = 0, 6$  and  $1, 5$  and  $2, 4$  and  $3$ ) of  $2 \cdot (1 \times 1) + 2 \cdot (2 \times 3) + 2 \cdot (1 \times 6 + 3 \times 3) + 1 \cdot (2 \times 8 + 4 \times 1) = 64 = 4^3$ , i.e. the complete state space of three spinful fermionic levels. Note that 1-particle excitations from  $g2$  (yellow lines) cannot reach the  $S = \frac{3}{2}$  multiplet  $e1$ .

The local Hamiltonian of a single site  $i$  is given by  $\hat{H}_{\text{loc}}^{(i)} \equiv \hat{H}_{\text{int}}[\hat{d}_{i\nu}^\dagger] - \mu \hat{n}_i$ . With focus on the specific filling  $n_d = 2$ , this Hamiltonian can be written as

$$\hat{H}_{\text{loc}}^{(i)} = \frac{\tilde{U}}{2}(\hat{n}_i - 2)^2 - J\hat{\mathbf{S}}_i^2 - \underbrace{(\mu - \mu_2)}_{\equiv \delta\mu_2} \hat{n}_i - 2\tilde{U}. \quad (2)$$

with  $\mu_2 \equiv \frac{3}{2}(U - J)$ . Here the Coulomb interaction in the first term on the r.h.s. has been written such that for  $\mu = \mu_2$ , i.e.  $\delta\mu = 0$  and small  $J$ , this Hamiltonian clearly favors the desired filling of  $n_d = 2$ . By writing the local states space in terms of symmetry multiplets, the above Hamiltonian reduces to one-dimensional multiplet blocks and hence already becomes diagonal. The symmetry labels of SU(3) follow the Dynkin convention where the irreducible representation  $q = (q_1, q_2) \equiv (q_1 q_2)$  corresponds to a Young diagram with  $q_1 + q_2$  ( $q_2$ ) boxes in its first (second) row.

For the case  $\mu = \mu_2$ , the multiplet structure of the local Hamiltonian in Eq. (2) is sketched in Fig. 2. There the two low-energy multiplets at  $n_d = 2$  are labeled by  $g1$  and  $g2$ , also referred to as the  $g$ -levels. The actual ground state multiplet  $g1$  is in triplet configuration across two out of the three orbitals. The singlet configuration  $g2$ , split off by an energy  $2J$ , also includes the pair singlets within a single orbital. This therefore results in a total of  $d_{g2} = 6$  symmetric states described by the single irreducible multiplet  $q = (20)$ . By removing an electron, this leads to the hole-like level, denoted by  $h$ . It contains just one electron,  $n_d = 1$ , which can be in any spin and orbital, hence  $S = \frac{1}{2}$  and the defining representation  $q = (10)$ . Conversely, by adding a particle to the  $g$ -multiplets, one obtains half-filling  $n_d = 3$ . This allows states with one particle per orbital, resulting in one  $S = \frac{3}{2}$  multiplet, labeled  $e1$  with  $(S, q) = (\frac{3}{2}, 00)$ , and two  $S = \frac{1}{2}$  multiplets. By symmetry, the latter ones need to be grouped with the six  $S = \frac{1}{2}$  multiplets with a double and a singly occupied orbital into the single SU(3) multiplet  $q = (11)$  with 8 states total, forming the single multiplet  $e2$ .

In what follows, we now slightly alter the chemical potential towards finite  $\delta\mu_2$  in Eq. (2), using the specific choice  $\delta\mu_2 = -\frac{3J}{2}$ . This raises the  $e$ -levels in Fig. 2 and lowers the  $h$ -level by equal amounts relative to the  $g$ -levels at  $n_d = 2$ , to the extent that level  $h$  and  $e1$  become aligned, i.e. degenerate. This simplified setting is the reason for our choice of  $\delta\mu_2$ .

The resulting excitation energies from the ground state multiplet  $g1$  can be simply determined from

Fig. 2 while also accounting for the plain shift due to  $\delta\mu_2$  in Eq. (2),

$$\begin{aligned}
\circ & \quad \omega_{e1}^{(2)} \equiv +(E_{e1} - E_{g1}) = \frac{U}{2} - J, \\
+ & \quad \omega_{e2}^{(2)} \equiv +(E_{e2} - E_{g1}) = \frac{U}{2} + 2J, \\
\triangle & \quad \omega_h^{(2)} \equiv -(E_h - E_{g1}) = -\omega_{e1}^{(2)},
\end{aligned} \tag{3a}$$

where we added the superscript (2) to these transition frequencies for later reference to emphasize the current setting of having  $n_d = 2$  (this filling is implicit for the  $g$ -,  $e$ -, and  $h$ -multiplet labels in the present discussion, for readability). The signs in Eqs. (3a) are taken in consistency with the definition of the spectral function  $A(\omega)$ , and is thus opposite for particle- and hole-like excitations. The symbols to the left will be used in Sec. 4 and Sec. 5 to mark the positions of the multiplet excitation energies in the spectral function  $A(\omega)$ .

Similarly, also the transition energies w.r.t. level  $g2$  are simply derived from Fig. 2,

$$\begin{aligned}
+ & \quad \tilde{\omega}_{e2}^{(2)} \equiv +(E_{e2} - E_{g2}) = \omega_{e2}^{(2)} - 2J = \frac{U}{2}, \\
\triangle & \quad \tilde{\omega}_h^{(2)} \equiv -(E_h - E_{g2}) = \omega_h^{(2)} + 2J = -(\frac{U}{2} - 3J),
\end{aligned} \tag{3b}$$

where we note that the transition  $\tilde{\omega}_{e1}^{(2)} = -\tilde{\omega}_h^{(2)}$  is forbidden for 1-particle spin-half excitation processes.

The above picture of well-separated ground-state multiplets breaks down entirely, once  $\omega_{e1}^{(2)}$  in Eqs. (3a) becomes negative, i.e. levels  $h$  and  $e1$  cross  $g1$  as the new ground state. Hence we will mostly constrain our discussion to the regime  $J/U < 0.5$ . This regime, nevertheless, already reaches up to extraordinarily large Hund's coupling from a materials point of view where one typically encounters  $J/U \lesssim 0.2$  [47].

For  $J \ll U$ , the  $g$ -levels are typically considered well-separated from the  $e$ - and  $h$ -levels. However, this picture already breaks down earlier, namely once the degenerate  $e1$ - and  $h$ -levels pass across  $g2$ . According to the excitation energies in Eqs. (3b), this occurs at  $\tilde{\omega}_h^{(2)} = 0$  which defines the crossover energy scale  $J^* \equiv \frac{U}{6}$ . The regime  $J \gtrsim J^*$  quantifies what we mean by *sizeable* Hund's coupling in the 3HHM at  $n_d = 2$ . There for  $J \gtrsim J^*$ , we expect a qualitative change in the emerging physics of the 3HHM.

### 2.6.2. Multiplet structure at filling $n_d = 3$

We now focus on the filling  $n_d = 3$  with the Hamiltonian

$$\hat{H}_{\text{loc}}^{(i)} = \frac{\tilde{U}}{2}(\hat{n}_i - 3)^2 - J\hat{S}_i^2 - \underbrace{(\mu - \mu_3)}_{\equiv \delta\mu_3} \hat{n}_i - \frac{9}{2}\tilde{U}, \tag{4}$$

and  $\mu_3 \equiv \frac{5}{2}U - 3J$ . By construction,  $\mu = \mu_3$ , i.e.  $\delta\mu_3 = 0$  directly leads to a particle-hole symmetric excitation spectrum, and therefore to exact half-filling at  $n_d = 3$ . The multiplets in Fig. 2 are shifted relative to each other for different  $n_d$  such that  $n_d = 3$  becomes the new ground state symmetry sector with the lowest energy excitations in  $n_d = 2$  and 4 split off symmetrically by  $\tilde{U}/2$  at  $J = 0$ . Hence the  $g$ - and  $e$ -multiplets in the previous discussion for  $n_d = 2$  as in Fig. 2 acquire the new respective labels  $h$  and  $g$  here at  $n_d = 3$ .

In the following we only focus on the case of sizeable  $J$ , and there, for simplicity, only on the lowest levels  $h$ ,  $g$ , and  $e$  at  $n_d = 2, 3, 4$ , respectively. The level  $g$  has maximal spin  $S = 3/2$  linked with an orbital singlet configuration  $q = (00)$  [level  $e1$  in Fig. 2]. The lowest hole level  $h$  at  $n_d = 2$  has  $(S, q) = (1, 01)$  [i.e. level  $g1$  in Fig. 2]. The lowest particle level  $e$  at  $n_d = 4$  is given by  $(S, q) = (1, 10)$ , i.e. the particle-hole transformed level  $h$ .

The excitation energies from the ground state multiplet  $g$  at  $\mu = \mu_3$  can be simply determined from Eq. (4), analogous to Eq. (3a),

$$\begin{aligned}
* & \quad \omega_e^{(3)} \equiv +(E_e - E_g) = \frac{U}{2} + J, \\
\diamond & \quad \omega_h^{(3)} \equiv -(E_h - E_g) = -\omega_e^{(3)},
\end{aligned} \tag{5}$$

where the reference point of a filling of  $n_d = 3$  is implied, yet also explicitly indicated with the superscript in the transition frequencies. We will refer to them in Sec. 5.

## 2.7. Overview of Results

In the following three sections we present our real-frequency-based DMFT+NRG results for the 3HHM. In Sec. 3 we reveal the connection between SOS and spin-freezing. We argue that while both terminologies describe in principle the same Hund physics, the latter term has the drawback that it was proposed based on QMC results that did not account for a Fermi-liquid ground state. In Sec. 4 we study the  $U$ - $J$ -phase diagram at  $n_d = 2$  and systematically disentangle the Janus-faced effects of (i) Hundness and (ii) Mottness. Thereby we quantitatively explain the existence of the low QP weight,  $Z$ , by SOS, which is revealed to occur in the whole metallic regime, but at different scales. We explain the difference between Hund- and Mott-correlated systems. In particular, we show that sizeable  $J$  leads to low  $Z$  also far away from the MIT at  $n_d = 2$  and opens up a *large* incoherent frequency regime where intriguing Hund-correlated physics occurs: large, almost unscreened spins are coupled to screened orbital degrees of freedom. In Sec. 5, we study the doping-dependence of  $Z$  and the compressibility,  $\kappa_{el}$ . We demonstrate that, in principle, SOS also occurs and determines the low  $Z$  behavior at intermediate fillings,  $1 < n_d < 3$ . We give evidence that SOS is generically based on a two-stage screening process involving the formation and the full screening of effective  $3/2$  spins. The details of this process, however, vary with filling.  $\kappa_{el}$  is shown to be positive at finite  $J$  for all fillings and values of  $U$ , that we have studied. Thus we assume that no Hund's-coupling-induced instabilities emerge in the system.

Overall, we scan the parameter space of the phase diagram in two orthogonal directions (indicated by the arrows in Fig. 1): we either vary  $n_d$  (along the horizontal direction of the red arrow) for different parameter sets of  $U$  and  $J$  as in Sec. 3 and Sec. 5, or we vary  $U$  (along the vertical direction of the blue arrow) and  $J$  for fixed  $n_d = 2$  as in Sec. 4.

To summarize, we will develop a global picture of spin-orbital separation that strongly supports (i) Hundness as a new mechanism towards strong correlations in the normal state of Hund metals.

## 3. Spin-freezing and spin-orbital separation - two terminologies for the same Hund physics

To set the scene, we first revisit SOS [33] and explain its connection to the spin-freezing theory introduced in 2008 in a finite-temperature DMFT+QMC study [51] of the  $n_d$ - $U$  phase diagram of a degenerate three-band Hund model.

### 3.1. Spin-orbital separation at $n_d = 2$ revisited

We calculate the dynamical real-frequency spin and orbital susceptibilities

$$\chi_{\text{sp}} = \frac{1}{3} \sum_{\alpha} \langle \hat{S}^{\alpha} \| \hat{S}^{\alpha} \rangle_{\omega}, \quad (6a)$$

$$\chi_{\text{orb}} = \frac{1}{8} \sum_a \langle \hat{T}^a \| \hat{T}^a \rangle_{\omega}, \quad (6b)$$

respectively, where  $\hat{T}^a = \sum_{mm'\sigma} \hat{d}_{m\sigma}^{\dagger} \frac{1}{2} \tau_{mm'}^a \hat{d}_{m'\sigma}$  are the impurity orbital operators with the SU(3) Gell-Mann matrices,  $\tau^a$ , normalized as  $\text{Tr}[\tau^a \tau^b] = 2\delta_{ab}$ .

Fig. 3(a) depicts the zero-temperature results of the imaginary parts,  $\chi''(\omega) \equiv -\frac{1}{\pi} \text{Im} \chi(\omega)$ , of the dynamical impurity orbital (dashed curve) and spin (solid curve) susceptibilities for  $U = 5$ ,  $J = 1$  and a filling of  $n_d = 2$ . The filled circle and the open square mark the orbital and spin Kondo scales,  $T_{\text{K}}^{\text{orb}}$  and  $T_{\text{K}}^{\text{sp}}$ , which are defined as the peak positions of  $\chi''_{\text{orb}}$  and  $\chi''_{\text{sp}}$ , respectively. Clearly, these two energy scales are very distinct: in Fig. 3(a) we revisit the central result of our DMFT+NRG study of the 3CAHM – *spin-orbital separation* [see Fig. 3(c) in Ref. [33] and also Fig. 13]. *Orbital screening sets in at much higher energies than spin screening,  $T_{\text{K}}^{\text{orb}} \gg T_{\text{K}}^{\text{sp}}$ , opening a non-trivial intermediate NFL regime exhibiting “Hund metal physics”: slowly fluctuating (not frozen), Hund's-coupling-induced large spins are coupled to screened orbital degrees of freedom.* The existence of large, composite spins which are only poorly screened, manifests itself in an enhancement of  $\chi''_{\text{sp}}$  with decreasing frequencies. Interestingly, the fluctuations of these spins influence the physics of the screened orbitals, leading to an intriguing interplay of spin and orbital degrees of freedom:

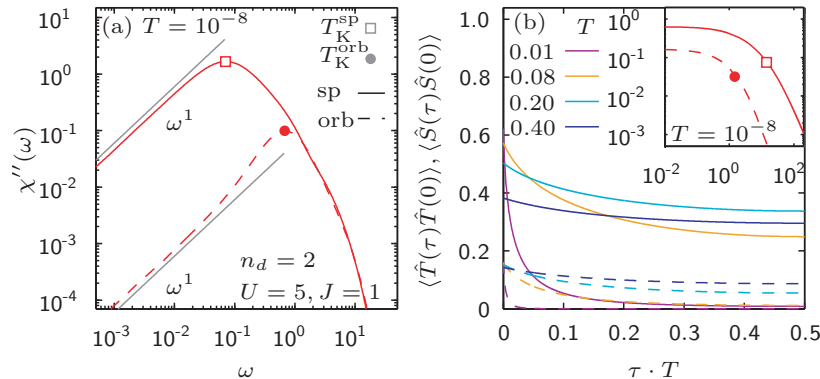


Figure 3: (a) The imaginary part of the dynamical real-frequency orbital  $\chi''_{\text{orb}}$  (dashed) and spin  $\chi''_{\text{sp}}$  (solid) susceptibility for  $U = 5$ ,  $J = 1$ ,  $n_d = 2$  and  $T = 0$ . The orbital Kondo scale  $T_K^{\text{orb}}$  (filled circle) and the spin Kondo scale  $T_K^{\text{sp}}$  (open square) are defined as the peak positions of  $\chi''_{\text{orb}}$  and  $\chi''_{\text{sp}}$ , respectively, and show SOS, i.e.  $T_K^{\text{orb}} \gg T_K^{\text{sp}}$ . Grey guide-to-the-eye lines indicate Fermi-liquid power laws. (b) The imaginary-time impurity orbital-orbital  $\langle \hat{T}(\tau)\hat{T}(0) \rangle$  (dashed) and spin-spin  $\langle \hat{S}(\tau)\hat{S}(0) \rangle$  (solid) correlator plotted as a function of the rescaled imaginary time  $\tau \cdot T$  for the same parameters as in (a), but at different temperatures. The solid yellow and blue curves show spin-freezing:  $\langle \hat{S}(\tau)\hat{S}(0) \rangle$  approach large constant values at times  $\tau = 1/(2T)$ . The inset shows the zero-temperature results of  $\langle \hat{T}(\tau)\hat{T}(0) \rangle$  (dashed) and  $\langle \hat{S}(\tau)\hat{S}(0) \rangle$  (solid) calculated from (a) the real-frequency susceptibilities. Both approach zero in the FL regime at very large imaginary times. The filled circle and the open square mark  $1/T_K^{\text{orb}}$  and  $1/T_K^{\text{sp}}$ , respectively.

below  $T_K^{\text{orb}}$ ,  $\chi''_{\text{orb}}$  decreases as the frequency is lowered, indicating the screening of the orbital degrees of freedom. However, for  $\omega > T_K^{\text{sp}}$ ,  $\chi''_{\text{orb}}$  does not follow FL scaling, as the orbital degrees of freedom still “feel” the slowly fluctuating, large local moments. Below the very small, Hund’s-coupling-reduced coherence scale,  $T_K^{\text{sp}} \approx 0.072$ , both the spin and orbital degrees of freedom get fully screened and FL behavior is restored [ $\chi''_{\text{orb}}(\omega) \propto \omega$  and  $\chi''_{\text{sp}}(\omega) \propto \omega$ , see Fig. 3(a), grey lines].

From the real-frequency orbital and spin susceptibility we also calculate the imaginary-time impurity orbital-orbital and spin-spin correlators,

$$\begin{aligned} \langle \hat{T}(\tau)\hat{T}(0) \rangle &\equiv \frac{1}{8} \langle \hat{\mathbf{T}}(\tau) \cdot \hat{\mathbf{T}}(0) \rangle = \int d\omega n_B(\omega) \chi''_{\text{orb}}(\omega) e^{\omega\tau}, \\ \langle \hat{S}(\tau)\hat{S}(0) \rangle &\equiv \frac{1}{3} \langle \hat{\mathbf{S}}(\tau) \cdot \hat{\mathbf{S}}(0) \rangle = \int d\omega n_B(\omega) \chi''_{\text{sp}}(\omega) e^{\omega\tau}, \end{aligned} \quad (7)$$

respectively, with the Bose-Einstein distribution  $n_B(\omega) = 1/(e^{\beta\omega} - 1)$ . In the inset of Fig. 3(b) we plot both correlators for zero temperature and the same parameters as in Fig. 3(a). In accordance with the real-frequency susceptibilities, the orbital-orbital correlator (dashed curve) is much smaller than the spin-spin correlator (solid curve). The latter approaches zero rather slowly, thus, the FL regime is only reached at very long imaginary times,  $\tau > 100$ .

### 3.2. Spin-freezing at $n_d = 2$

In order to understand the connection of SOS and the spin-freezing phenomenon that was based on *finite-temperature* DMFT+QMC [51] data, we have performed similar calculations at higher temperatures [see Fig. 3(b)]. For temperatures well below the FL coherence scale,  $T < T_K^{\text{sp}}$ ,  $\langle \hat{S}(\tau)\hat{S}(0) \rangle$  decays to zero on the scale  $\tau = 1/(2T)$  (solid purple curve). For  $T_K^{\text{orb}} \geq T \geq T_K^{\text{sp}}$ , in contrast,  $\langle \hat{S}(\tau)\hat{S}(0) \rangle$  approaches a large constant value at times  $\tau \approx 1/(2T)$  (solid yellow and blue curves). This finite-temperature finding – a spin-spin correlation function which does not decay to zero at long times – was called “spin freezing” in Ref. [51] and interpreted as the existence of *frozen* local moments leading to an incoherent metallic state.

As exemplified in Fig. 3 (a,b) and further demonstrated in this work, spin freezing was a phenomenological interpretation of the spin-spin correlator based on a QMC solver that didn’t reach low enough temperatures

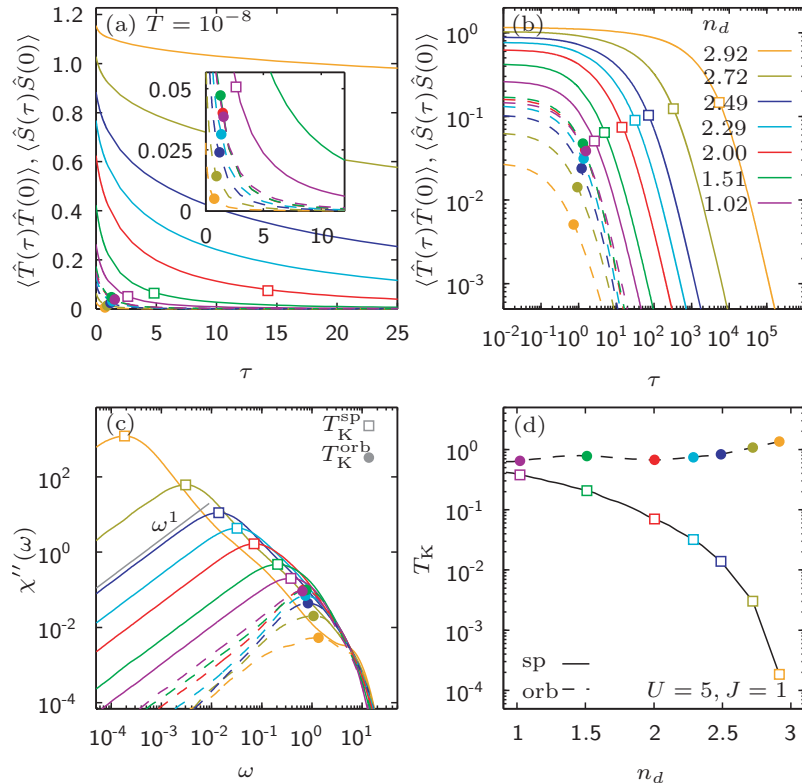


Figure 4: (a,b) The imaginary-time impurity orbital-orbital  $\langle \hat{T}(\tau)\hat{T}(0) \rangle$  (dashed) and spin-spin  $\langle \hat{S}(\tau)\hat{S}(0) \rangle$  (solid) correlators calculated from (c) the real-frequency susceptibilities for  $U = 5$ ,  $J = 1$ , and  $T = 0$  at various fillings  $n_d$ . The filled circles and the open squares mark  $1/T_K^{\text{orb}}$  and  $1/T_K^{\text{sp}}$ , respectively. The inset in (a) shows a zoom to better resolve the orbital-orbital correlators. (a) For short imaginary times, the curves for  $\langle \hat{S}(\tau)\hat{S}(0) \rangle$  seem to remain constant, a phenomenon which was interpreted as spin-freezing in Ref. [51]. (b) In contrast, for large imaginary times, they clearly show FL behavior. (c) The imaginary parts of the dynamical real-frequency orbital  $\chi''_{\text{orb}}$  (dashed) and spin  $\chi''_{\text{sp}}$  (solid) susceptibilities. The orbital Kondo scales  $T_K^{\text{orb}}$  and the spin Kondo scales  $T_K^{\text{sp}}$  are marked as filled circles and open squares, respectively. (d) The orbital Kondo scales  $T_K^{\text{orb}}$  (dashed line with filled circles) and spin Kondo scales  $T_K^{\text{sp}}$  (solid line with open squares) plotted versus the filling  $n_d$ . SOS is revealed for all  $1 < n_d < 3$ .

(or equivalently long enough times) to reveal the FL ground state for many parameters in the phase space. However, *the spins are not frozen, they fluctuate slowly above  $T_K^{\text{sp}}$  and get fully screened in the FL regime below  $T_K^{\text{sp}}$ .*

Moreover, a detailed analysis of  $\langle \hat{T}(\tau)\hat{T}(0) \rangle$  at  $n_d = 2$  in Fig. 3(b) shows that the orbital-orbital correlators (dashed yellow and dashed light and dark blue curves) do not fully decay to zero in the incoherent temperature regime  $T > T_K^{\text{sp}}$ , but remain finite, as well (as opposed to the statement in Ref. [51]). This finding supports the interpretation obtained from the real-frequency orbital susceptibility and further revises the spin-freezing picture: *the orbital degrees of freedom are screened below  $T < T_K^{\text{orb}}$ , but they are not fully decoupled from the spin dynamics.*

### 3.3. Spin-freezing for varying $n_d$

Originally, without access to the FL ground state, it was argued that the Hund-metal regime of the phase diagram in Fig. 1 is a spin-freezing NFL phase and that a quantum phase transition connects a paramagnetic FL phase (at small  $n_d$  and small  $U$ ) and a paramagnetic NFL phase featuring frozen local moments (at larger  $n_d$  and larger  $U$ ) [51].

In Fig. 4 we revisit this transition with our NRG solver at  $T = 0$ . We calculate the imaginary-time orbital-orbital and spin-spin correlators for intermediate  $U = 5$ ,  $J = 1$  and vary  $n_d$  from 1.02 to 2.92. Indeed, at short times,  $\tau \lesssim 25$ , our DMFT+NRG results in Fig. 4(a) seem to confirm this FL-to-NFL transition. For  $n_d < 2$ ,  $\langle \hat{S}(\tau)\hat{S}(0) \rangle$  decays to zero (solid purple and green curves) while at larger  $n_d$  it grows and remains finite (solid red to yellow curves), seemingly indicating frozen local moments.

However, in contrast to QMC solvers, we have direct access to exponentially long times (low temperatures) and can explicitly reveal the existence of a FL ground state for any given filling. In Fig. 4(b) we confirm that for sufficiently long times,  $\tau \gg 1/T_K^{\text{sp}}$ ,  $\langle \hat{S}(\tau)\hat{S}(0) \rangle$  approaches zero for all fillings,  $1 < n_d < 3$  (solid curves). Equivalently, all real-frequency spin susceptibilities exhibit FL behavior below  $T_K^{\text{sp}}$  [ $\chi''_{\text{sp}}(\omega) \propto \omega$ , see Fig. 4(c), grey line]. Clearly, the NFL regime is not governed by the proximity to a quantum critical point.

The general existence of a FL ground state for all fillings was later conjectured [14, 53, 70] and only recently demonstrated [71] based on DMFT+QMC Hund-model studies, and spin freezing was reinterpreted as the existence of long-lived magnetic moments. Instead of a quantum phase transition, a “spin-freezing crossover” from a FL to a NFL state at finite temperatures was suggested [70] (which is called “coherence-incoherence crossover” by others [6, 7, 33]). The present work demonstrates directly and completely that *the time-dependence of orbital-orbital and spin-spin correlation functions reveal FL behavior in the long-time limit for all fillings  $1 < n_d < 3$ .*

#### 3.4. Spin-orbital separation for varying $n_d$

Interestingly, we observe in Fig. 4 that *SOS*, *i.e.*  $T_K^{\text{orb}} \gg T_K^{\text{sp}}$ , occurs at all fillings  $1 < n_d < 3$  (in Ref. [33], it was only explicitly revealed at  $n_d = 2$ ).  $T_K^{\text{sp}}$  is found to be strongly doping dependent [see Fig. 4(c,d), open squares]. It decreases very fast with increasing filling  $n_d \rightarrow 3$ , such that the decay of  $\langle \hat{S}(\tau)\hat{S}(0) \rangle$  with imaginary time becomes very weak and is therefore almost invisible on short time scales [Fig. 4(a), e.g. solid, yellow curve]. In contrast,  $T_K^{\text{orb}}$  is almost independent of the filling [see Fig. 4(c,d), filled circles]. It even increases slightly from  $n_d = 2$  to  $n_d = 3$ . In summary, this leads to an intermediate regime of SOS that expands with larger  $n_d \rightarrow 3$ , mainly towards smaller energies [Fig. 4(d)].

Based on these insights we conclude that SOS is a generic feature in the whole Hund-metal regime, evolving with  $n_d$  in the following way. With increasing  $n_d$ , larger local moments form in the intermediate SOS regime and lead to the increase of the maximum of  $\chi''_{\text{sp}}$  (or equivalently  $\langle \hat{S}(\tau)\hat{S}(0) \rangle$ ) [see solid curves Fig. 4(a-c)]. At the same time,  $T_K^{\text{sp}}$  is lowered, because, heuristically, it is more difficult to screen these larger spins. In contrast, the height of  $\chi''_{\text{orb}}$  (or equivalently  $\langle \hat{T}(\tau)\hat{T}(0) \rangle$ ) decreases with increasing  $n_d \rightarrow 3$  [see dashed curves in Fig. 4(a-c) and inset of (a)]. This reflects the reduction of the phase space for orbital fluctuations due to the formation of large spins composed of electrons in different orbitals. Consequently, the interplay of spin and orbital degrees of freedom is diminished for  $n_d$  close to 3.

This first crude analysis of our results with varying  $n_d$  will be refined in Sec. 5. There, we will show in more detail how it is connected to the SOS scenario introduced above for  $n_d = 2$ .

#### 3.5. The connection between spin-freezing and spin-orbital separation

In sum, we argue that *the two terminologies, “spin-freezing” and “spin-orbital separation”, ultimately describe the same physics of the Hund-metal regime.* The large spins that appear as “frozen” at short imaginary times (which are accessible for QMC) were revealed by our real-frequency finite and zero-temperature DMFT+NRG approach as long-lived, slowly fluctuating, large local moments in the incoherent regime, that get fully screened at long imaginary times to form a FL ground state. In this picture, the intermediate energy regime of Hund metals with its incoherent transport properties is governed by scattering off (almost) free, large and long-lived magnetic moments that are non-trivially coupled to (almost) screened orbital degrees of freedom. A local spin susceptibility showing Pauli behavior at low and (quasi) Curie-Weiss behaviour at intermediate temperatures in Refs. [37, 78] supports this viewpoint.

We note that various DMFT+QMC findings on spin-freezing, such as spin-freezing in (realistic) five-band calculations for iron-pnictides [11, 12, 14, 19], spin-freezing in models with crystal-field-splitting [66], and spin-orbit coupling [69] eventually demonstrate the importance of SOS. In 2015, a fluctuating-moment-induced s-wave spin-triplet superconducting mechanism was proposed for Hund metals, where equal-spin

electrons are paired in different local orbitals. It was shown to be connected to the emergence of local magnetic moments in the NFL regime [70]. In 2016, it was even conjectured that the relevant model for cuprates, the single-orbital Hubbard model on the square lattice, can be mapped onto an effective multi-orbital problem with strong ferromagnetic Hund’s coupling, suggesting that spin-freezing (or equivalently SOS) is the universal mechanism which controls the properties of unconventional superconductors [79].

The insights gained above are relevant for a wide range of fillings  $n_d$  and interaction strengths  $U$  and  $J$ , as will be further demonstrated in Sec. 4 and Sec. 5. In these sections we will also clearly show that, indeed, SOS causes the numerically observed bad-metallic behavior in the 3HHM. SOS therefore constitutes the framework for our main study of Hund metals.

#### 4. Janus-faced influence of Hund’s rule coupling: Hundness versus Mottness at $n_d = 2$

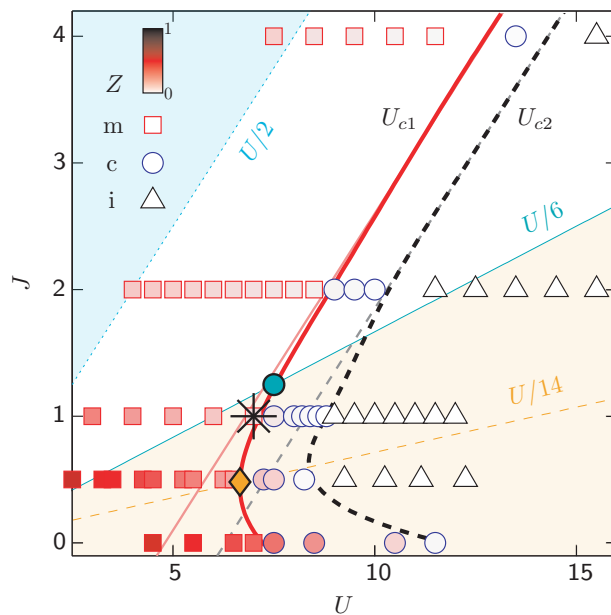


Figure 5: The zero-temperature phase diagram of the 3HHM at  $n_d = 2$  reveals three phases in the  $J$ - $U$ -plane: a metallic phase (squares), a coexistence region (circles), and an insulating phase (triangles), separated by two non-monotonic phase transition lines,  $U_{c1}$  (solid red curve) and  $U_{c2}$  (dashed black curve), obtained when initiating the DMFT self-consistency with an insulating and metallic seed, respectively. The color intensity of the symbols in the metallic and the coexistence region indicates the value of  $Z \in [0, 1]$ : the lower  $Z$  the more faded is the red color. Based on the discussion of the multiplet structure in Fig. 2, we added guides at  $J = U/2$  [ $\omega_{e1} = \omega_h = 0$ ] and  $J = U/6$  [ $\tilde{\omega}_h = 0$ ] and shaded the areas separated by these. The crossing point of  $U_{c1}$  with the  $U/6$  (cyan circle) occurs at  $(U, J) \approx (7.5, 1.25)$ . We also added a guide  $U/14$  (see text), whose crossing point with  $U_{c1}$  (orange diamond) occurs very close to the minimum of  $U_{c1}$  at  $(U, J) \approx (6.66, 0.48)$ . The black star marks the parameters for which SOS has first been revealed in Ref. [33]. [Note that Ref. [33] used a slightly different definition of the Coulomb energy which, while keeping the definition of  $J$  the same, corresponds to  $U = 7$  here.]

In this section we derive SOS as a consistent explanation for the extended bad-metallic behavior (low  $Z$ ) in the phase diagram at  $n_d = 2$  that reaches from a high critical  $U_c^{(2)}$  down to an unusually low  $U$ , i.e. we explain the Janus-faced behavior. By introducing clear measures for (i) Hundness and (ii) Mottness we are able to show that sizeable  $J$ , thus (i), leads to low  $Z$  also far away from the MIT at  $n_d = 2$  and opens up a large incoherent SOS regime with intriguing Hund-correlated physics.

In this section, all results are calculated at  $T = 0$ . Further, we note that we will neglect the superscript (2) in  $U_c^{(2)}$  because we will mainly refer to the filling,  $n_d = 2$ , in the following. The few exceptions where we refer to other fillings will be clear from the context.



#### 4.1. $U$ - $J$ phase diagram

As an overview, Fig. 5 presents the full  $U$ - $J$  phase diagram for  $n_d = 2$  at  $T = 0$ . We find a metallic (squares), coexistence (circles) and insulating (triangles) region, which are separated by two distinct Mott transition lines,  $U_{c1}$  (solid red line) and  $U_{c2}$  (black dashed line), respectively. We note that, so far, only  $U_{c2}$  has been studied in the context of three-band Hund models in the literature, because it can be simply derived from the QP weight  $Z$ . The black star in Fig. 5 marks the parameters of the main result in Fig. 3 of Ref. [33], for which SOS was revealed. It lies at the border of the coexistence region close to  $U_{c1}$ , raising the question how stable this feature is at lower  $U$ .

In Landau’s Fermi-liquid theory, the quasiparticle weight

$$Z = (1 - \partial_\omega \text{Re} \Sigma(\omega)|_{\omega=0})^{-1} = \frac{m}{m^*}$$

is obtained from the frequency-dependent self-energy  $\Sigma(\omega)$ , which is directly accessible in NRG, and measures the inverse mass enhancement within single-site DMFT. Landau’s Fermi-liquid theory is based on a one-to-one correspondence between long-lived, coherent but renormalized Landau QPs and the low-energy excitations of a free Fermi gas.  $Z \in [0, 1]$  reflects the weight of the Lorentzian-shaped coherent QPP of the momentum-dependent local spectral function in a first order expansion, while the additional incoherent part has weight  $1 - Z$ . In Fig. 5 the value of  $Z$  is indicated by the color intensity of the red squares and blue triangles in the conducting regime  $U < U_{c2}$ .

Similar to the case of the one-band Hubbard model, the MIT shows hysteresis at low temperatures in the multi-band case. Starting with an “insulating seed” (iS) [i.e. a real-frequency local spectral function  $A(\omega)$ , with an insulating Mott gap,  $\Delta$ , around the Fermi level], the MIT transition occurs at a lower critical interaction strength,  $U_{c1}$ , at which  $\Delta$  closes with decreasing  $U$ . Starting with a “metallic seed” (mS) [i.e. a metallic input spectral function with finite weight at  $\omega = 0$ ] leads, in contrast, to a larger critical value,  $U_{c2}$ , above which the QP resonance is lost (accordingly  $Z = 0$ ) and a stable gap is formed with increasing  $U$ . Therefore  $Z$  can be used to quantitatively track the MIT at  $U_{c2}$  when initiating the DMFT loop with a mS. The coexistence region between  $U_{c1}$  and  $U_{c2}$  is characterized by two solutions, a metallic solution for mS and an insulating solution for iS. This is typical for DMFT. As mean-field approach with an iterative solution scheme it can have more than one stable fixed point, depending on the initialization. Fig. 5 demonstrates that the coexistence region is broad at  $J = 0$ , reaching from moderate to large values of  $U$ ; for finite but small  $J$ , it strongly narrows, shifting to lower  $U$  values; and at  $J > 1$ , it eventually approaches a fixed width while shifting linearly with  $J$  to ever larger  $U$  values [80, 81]. It is known that for  $J = 0$  both  $U_{c1}$  and  $U_{c2}$  grow as a function of  $N_c$  at *all* fillings of multi-orbital models [80]. In contrast, for given  $N_c$ , the effect of a finite  $J$  on  $U_{c1}$  and  $U_{c2}$  is strongly filling dependent [47, 53]. At half-filling  $U_{c1}$  and  $U_{c2}$  is strongly reduced, as finite  $J$  increases correlations by forming large  $S = N_c/2$  spin states that block the orbitals. For one electron/hole,  $U_{c1}$  and  $U_{c2}$  increases with  $J$ , as  $J$  reduces the effective Coulomb interaction in the system. At all intermediate fillings  $1 < n_d < N_c$ , the special non-monotonic dependence of  $U_{c1}$  and  $U_{c2}$  on  $J$  occurs, which has been mentioned by several previous studies (especially for  $U_{c2}$ ) [32, 47, 50, 53].

This non-monotonic behavior can be understood to a great extent from the local multiplet structure of the underlying local Hamiltonian. For  $n_d = 2$ , the relation of the local multiplet structure in Fig. 2 with the phase diagram is discussed in Fig. 5 (bright blue, white and orange regimes). As pointed out with Eqs. (3) in Sec. 2.6.1, we expect a strong qualitative change in the physics of the 3HHM once  $\tilde{\omega}_h$  turns negative. For the local multiplet structure, this occurs at the sizeable Hund’s coupling  $J \geq U/6$ . Accordingly, in the 3HHM, one can distinguish two regimes in the  $U$ - $J$  phase diagram of Fig. 5, by relating the  $U_{c1}$  phase boundary with the reference line  $J = U/6$ , for which a single crossing point exists at  $(U, J) \approx (7.5, 1.25)$  [cyan circle in Fig. 5]. Therefore, for the *sizeable* Hund’s coupling

$$J > J_{c1}^* \cong 1.25, \quad (8)$$

which we define as the “Hund regime” in the 3HHM, the high-lying  $h$ - and  $e1$ -multiplets have crossed below the  $g2$ -level. In this regime, a qualitatively different behavior occurs all the way up to  $U_{c1}$  as compared to standard Mott physics. Specifically,  $Z$  is low in the entire “Hund regime” [see color shading of symbols in

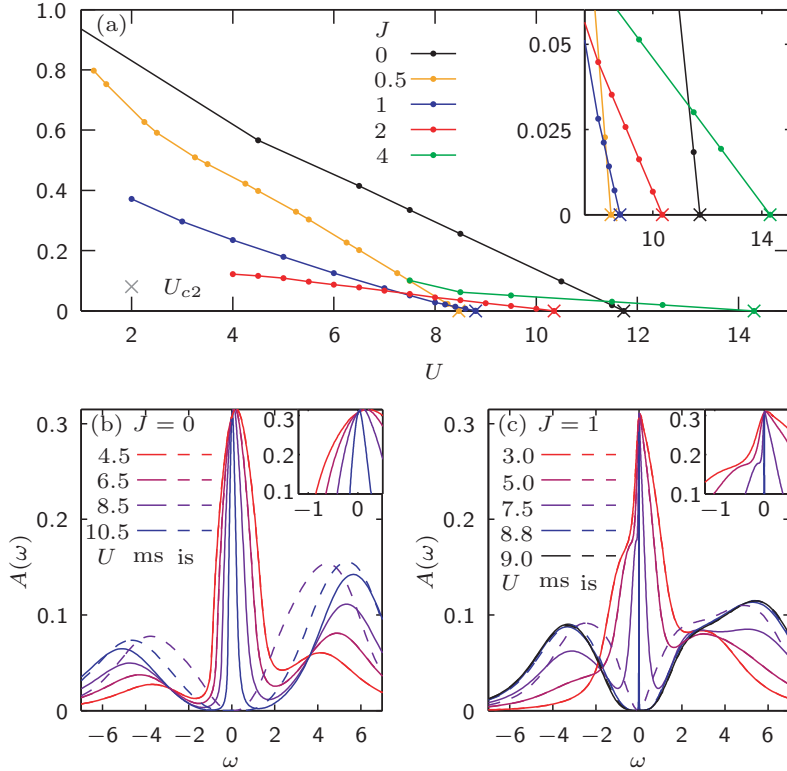


Figure 6: (a) The QP weight,  $Z$ , of the 3HHM at  $n_d = 2$ , plotted as a function of  $U$ , shows Janus-faced behavior when  $J$  is increased: on the one hand, at small to moderate  $U$ ,  $Z$  decreases (metallicity worsens), on the other hand,  $U_{c2}$  (marked by crosses) increases (metallicity improves). Each dot on the curves represents a DMFT+NRG data point. The inset is a zoom of the  $U_{c2}$ -behavior. (b,c) The local spectral function,  $A(\omega)$ , shows a MIT with growing  $U$  for (b)  $J = 0$  and (c)  $J = 1$ . Solid (dashed) lines are DMFT results for a metallic (insulating) seed. The insets zoom into the QP. For  $J = 1$ , the QP in  $A(\omega)$  shows a shoulder characteristic of SOS.

Fig. 5]. In contrast, for  $J < J_{c1}^*$ , which we refer to as “good-metal regime”,  $Z$  reaches up to much larger values [squares are colored in intensive red in Fig. 5]. More generally, one may already expect the crossover to the Hund regime to set in earlier. For example, considering the approaching  $h$ -level at  $\tilde{\omega}_h \sim 2\delta\omega_g$  with  $\delta\omega_g \equiv \omega_{g2} - \omega_{g1} = 2J$ , this results in  $J = U/14$  [also indicated by an orange dashed line in Fig. 5]. Its crossing point with  $U_{c1}$  occurs around  $(U, J) \approx (6.66, 0.48)$  [orange diamond in Fig. 5] which turns out to be in close proximity to the point where the non-monotonic behavior of  $U_{c1}$  versus  $J$  reaches a minimum, i.e. turns around at  $U_{c1}^{\min} \simeq 6.66$ . In summary, we see that as the Hund’s coupling exceeds the moderate value of  $J \gtrsim J_{c1}^* \sim 1$ , the 3HHM is dominated by Hund physics: sizeable  $J$  leads to a qualitative change in the local multiplet structure and thus to a strong change in the physics of the 3HHM, affecting both the phase boundaries,  $U_{c1}$  and  $U_{c2}$ , and the regime far from the MIT at much lower  $U$ , where  $Z$  is low.

The scaling of  $U_{c1}$  and  $U_{c2}$  for large  $J$ , eventually, is linked to a further stark change in the local multiplet structure, namely when the  $h$ - and  $e$ -levels actually become the new local ground states having  $\omega_{e1} < 0$ . Allowing for a shift by kinetic energy this suggests  $U_{c1} \simeq 2J + \text{const}$ . This scaling is approximated by thin solid red and dashed grey lines in Fig. 6(a), respectively, and will be further corroborated in Fig. 8(c).

#### 4.2. Janus-faced behavior of $Z$

In Fig. 6(a) we plot  $Z$  versus  $U$  for various values of  $J \in [0, 4]$ . In general,  $Z$  is finite in the metallic phase (with an upper limit of  $Z = 1$  for the non-interacting case) and zero in the insulating phase.  $U_{c2}$  is defined by the transition point between both phases [marked by  $\times$  in Fig. 6(a)]. We note, however, that near

the MIT Landau's Fermi-liquid theory might break down as a valid physical description of the excitations and  $Z$  only remains as a heuristic indicator of the MIT. For all  $J$ , we observe in Fig. 6(a) that  $Z$  decreases with increasing  $U$  in the metallic phase, thus strong correlation effects increase with increasing proximity to  $U_{c2}$ , as known from the half-filled one-band Hubbard MIT. However, the strength of correlations strongly differs for different values of  $J$ . For small  $J$ ,  $Z$  is still large at small to moderate  $U$ , while for large  $J$ ,  $Z$  is generally small [compare e.g. black and yellow curve to red or green curve in Fig. 6(a)]. Moreover,  $J$  induces competing effects. While  $Z$  strongly decreases with  $J$  at moderate  $U$  [see e.g. black to red curve at  $U = 6$  in Fig. 6(a)],  $U_c$  increases with  $J$  (for  $J \geq 0.5$ , after a slight decrease for very small  $J$ ) [see inset in Fig. 6(a)]. We thus observe Janus-faced behavior in our data similar to Ref. [53]: on the one hand  $J$  promotes bad metallicity by a loss of coherence, on the other hand it promotes metallicity by increasing  $U_{c2}$ . In sum, this Janus-faced behavior leads to a strongly reduced  $Z$  for sizeable  $J$  in a large interval of  $U$  (including the Hund-metal regime at  $n_d = 2$ ) [as seen e.g. for the red or green curve in Fig. 6(a)]. We will clarify its physical origin and nature in the following by disentangling the opposing Janus-faced effects.

#### 4.3. Real-frequency study of MIT at zero and finite $J$

For each data point in our  $U$ - $J$  phase diagram, NRG yields a set of detailed frequency-dependent information of the system, in contrast to previous QMC or slave-boson studies. This is useful, because  $Z$  only measures the strength but not the type, Hundness or Mottness, of strong correlations.

Much additional information about the MIT can be gained from the real-frequency local spectral function,  $A(\omega)$ , defined in Eq. (A.6). For example, the dual character of strongly correlated electrons is directly reflected in the shape of  $A(\omega)$ . In Fig. 6(b,c) we track the MIT in  $A(\omega)$ , i.e. how this dual character changes with  $U$ , for  $J = 0$  and  $J = 1$ , respectively. The metallic, delocalized behavior of electrons in the solid is characterized by a finite spectral weight at the Fermi level in form of a well-defined QPP [see e.g. solid and dashed red curves in Fig. 6(b,c)]. Local Kondo-type screening processes of the ground state multiplet dominate the low-energy physics of the self-consistent impurity model and lead in the 3HHM to a Fermi-liquid ground state with coherent QP excitations in the whole metallic phase, as will be discussed in detail later. The localized behavior of the electrons is manifest at high energies in terms of local (atomic) multiplet excitations which are broadened by the solid-state environment and form the Hubbard side bands (see discussion of Fig. 7). At small to moderate  $U$ , these incoherent high-energy bands are close to the Fermi level and even overlap, and the QPP is broad. With increasing  $U$ , the Hubbard side bands move to larger  $|\omega|$  and the QPP narrows [compare red versus blue curves in Fig. 6(b,c)]. Above  $U_{c1}$  or  $U_{c2}$  (depending on the seed) the DMFT self-consistency opens a Mott gap in  $A(\omega)$  around the Fermi level, the QPP vanishes and  $A(\omega)$  then consists solely of the high-energy bands [see e.g. black curve in Fig. 6(c)]. Heuristically, this decrease of the QPP width with increasing  $U$  is tracked by the QP weight,  $Z$ , as the peak height is pinned to a fixed value at zero frequency (Luttinger pinning [82, 83]) for all  $U < U_c$ .

As part of the MIT, we also directly observe the coexistence region  $U_{c1} < U < U_{c2}$  in Fig. 6(b,c). While the purely metallic and the purely insulating phase have only one solution of the DMFT self-consistency, independent of the seed, we find two differing solutions in the coexistence region, an insulating for iS and a metallic one for mS, respectively [see dashed versus solid purple and blue curves in Fig. 6(b,c)]. We note that NRG is perfectly suited for pinpointing  $U_{c1}$  and  $U_{c2}$  via  $A(\omega)$ , as its energy resolution is exponentially refined around the Fermi level, capturing the QPP down to its smallest width. Thus the iterative DMFT procedure does not break down before its solution becomes thermodynamically unstable. However, the broadening of discrete spectral data in NRG might minimally shift additional spectral weight to the Fermi level, thus artificially but only slightly shifting the coexistence region to larger  $U$  values.

At first glance, the MITs for  $J = 0$  and  $J = 1$  seem to behave overall similarly with changing  $U$ . However, we find striking differences between the spectra in Fig. 6(b) and Fig. 6(c), corresponding to the black and blue lines in Fig. 6(a), respectively.

As discussed above,  $Z$  is much lower for the  $J = 1$  MIT than for the  $J = 0$  MIT. Accordingly, we observe qualitative differences in the shape of the QPP. For finite  $J$ , in Fig. 6(c), the QPP has a shoulder at negative frequencies and a slight kink at positive frequencies. The shoulder (and the kink) drastically narrow the top of the QPP while the bottom remains broad. These features are present for all values of  $U$ , but they are more pronounced for smaller  $U$ , for which the overall width of the QPP is broader [see inset of Fig. 6(c)].

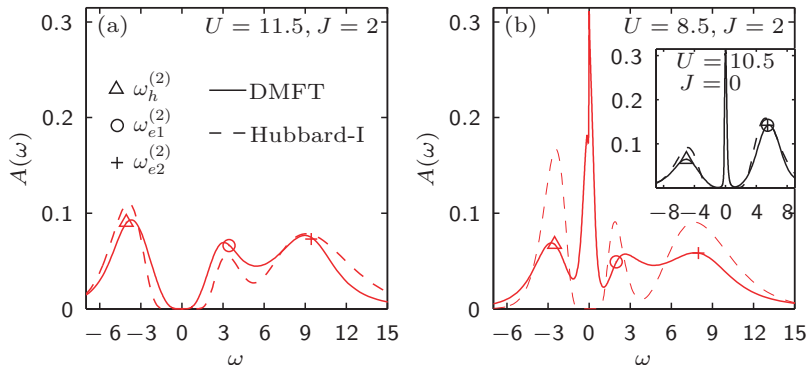


Figure 7: (a) Insulating and (b) metallic local spectral function,  $A(\omega)$ , for  $J = 2$ , obtained from DMFT+NRG (solid) and via Hubbard-I approximation (dashed). The symbols, as specified in the legend, correspond to the local multiplet excitations listed in Eqs. (3a). The inset in (b) shows results for  $J = 0$ . Here, the symbols correspond additionally to the transition frequencies in Eqs. (3b), i.e. triangles and pluses also correspond to  $\tilde{\omega}_h$  and  $\tilde{\omega}_{e2}$ . In order to directly compare the Hubbard-I approximation with the log-Gaussian broadened DMFT+NRG results, we convoluted the Hubbard-I spectral function with a log-Gaussian broadening Kernel of width  $\alpha = 0.4$ , as defined in Ref. [34].

At  $J = 0$ , however, these features are absent [see Fig. 6(b) and its inset]. From Ref. [33] we know that the shoulder emerges due to SOS, which only occurs for finite  $J > 0$ . Fig. 6(c,d) thus give a first hint that *there is a direct connection between the Janus-faced low  $Z$  and SOS*.

Further, we find differences in the shape of the Hubbard side bands. For  $J = 0$  there are two bumps in Fig. 6(b). The lower Hubbard band at negative frequencies is less pronounced than the upper Hubbard band at positive frequencies. With growing  $U$ , the distance between these Hubbard bands increases, reminiscent of the single-band Hubbard model. For  $J = 1$  there are in principle two Hubbard side bands, as well, in Fig. 6(c), however the band at positive frequencies consists of two bumps, so that, at large  $U$ , we observe *three* peaks altogether. For small  $U$ , the negative frequency and the lower positive frequency peaks are hidden in the QPP [red curve in Fig. 6(c)] and only one positive-frequency bump is visible. But with growing  $U \geq 4$  the lower peak is shifted to lower frequencies and the two-peak structure at positive frequencies clearly develops [see purple, blue and black curves in Fig. 6(c)].

#### 4.4. Peak structure of Hubbard bands: Hubbard-I analysis

The peak structure of the Hubbard bands (at zero temperature) can be fully understood in terms of a Hubbard-I approximation of the lattice Green’s function, i.e. from its local multiplet excitations, as demonstrated in Fig. 7. (This was stated in previous studies but never demonstrated explicitly, due to the lack of reliable real-frequency data [47, 50, 53]. So far, a similar real-frequency analysis was only carried out for a three-band Hund model at  $n_d = 1$  using Fork Tensor Product States as real-time DMFT solver [84]).

To obtain the local multiplet excitations spectrum of the underlying atomic problem, i.e. in the “atomic limit”,  $t = 0$ , we diagonalize the local Hamiltonian as discussed in Sec. 2.6.1 with Eq. (2) and schematically depicted in Fig. 2.

The positions of the peaks in the Hubbard bands shown in Fig. 7 are well captured by the discrete multiplet excitations indicated by the symbols provided with Eqs. (3). Thus *the structure of the incoherent side-bands can be understood from atomic physics*. In order to explicitly demonstrate this, i.e. to reproduce the form of the Hubbard bands, we use the Hubbard-I approximation around the atomic limit to disperse the atomic eigenstates by embedding them in a lattice environment. In this approximation the lattice self-energy is replaced in Eq. (A.5) by the purely atomic self-energy corresponding to the limit  $t = 0$  in Eq. (1):  $\Sigma(\omega) = \Sigma_{\text{atom}}(\omega)$ . The atomic self-energy is given by  $\Sigma_{\text{atom}}(\omega) = \omega + \mu - G_{\text{atom}}^{-1}(\omega)$  in terms of the atomic Green’s function,  $G_{\text{atom}}(\omega) = \sum_M p_M / (\omega - \omega_M + i0^+)$ , summing over the atomic multiplet excitation poles with  $p_M$  the probability for a one-particle excitation from the ground state into the excited state  $M$ .

The resulting Hubbard-I spectral functions are plotted with dashed lines in Fig. 7. The insulating DMFT spectral function for  $U = 11.5$  and  $J = 2$  is reproduced very well [Fig. 7(a)]. The structures of the Hubbard bands in the metallic states for  $U = 8.5$  and  $J = 2$  [Fig. 7(b)] and for  $U = 10.5$  and  $J = 0$  [inset of Fig. 7 (b)] are still matched reasonably well, but the QPP is not captured at all within the Hubbard-I approximation because finite-lifetime effects are not contained in the purely real atomic self-energy. For smaller  $U$  in the metallic regime, thus for a broader QPP in the spectral functions, the deviations between the DMFT and the Hubbard-I results therefore naturally increase.

The atomic excitation energies listed in Eqs. (3) fully explain the qualitatively different structure of the corresponding Hubbard bands: while two bumps are well-separated and pronounced at  $J = 0$  (with a larger peak at positive frequency due to the higher degeneracy of the corresponding atomic excitation), the three-peaked Hubbard bands form a broad incoherent background for sizeable  $J$ , because  $J$  shifts the inner side-peaks at  $\omega_{e1} = -\omega_h = \frac{U}{2} - J$  towards the Fermi level, while the peak at  $\omega_{e2} = \frac{U}{2} + 2J$  is shifted to higher frequencies. This difference was also recently revealed for two archetypal correlated materials, the Mott material  $V_2O_3$  and the Hund material  $Sr_2RuO_4$  [37]. We note that additional structures at the low-energy edges of the Hubbard bands with doublon-holon origin [85] are principally expected, but presumably a higher resolution using adaptive broadening [86] and/or extensive z-averaging [87] would be needed to resolve them.

#### 4.5. The “bare gap” as a measure of Mottness

In a next step we use the atomic excitation spectra for sizeable  $J \gtrsim J_{c1}^*$  to derive a measure of Mottness. Following Refs. [47, 50, 53, 57], we define the “bare gap”,  $\Delta_b \equiv \omega_{e1} - \omega_h = U - 2J$ , as the distance between the lowest atomic excitations at positive and negative frequencies. [Incidentally,  $\Delta_b$  is equal to the atomic interaction of the energetically most favored atomic configuration in line three of Eq. (1b)]. Up to an offset,  $\Delta_b$  measures the distance to the MIT. In this sense it is similar to the true Mott insulating gap  $\Delta$  which closes at the MIT. Here  $\Delta = \omega^+ - \omega^-$  is defined from the criterion that  $A(\omega) < 10^{-3}$  holds for  $\omega^- < \omega < \omega^+$ .

In the inset of Fig. 8(a) we plot  $\Delta$  versus  $U$  (for iS) for various values of  $J$  and derive  $U_{c1}$  from the closure of the Mott insulating gap,  $\Delta(U_{c1}) = 0$  (marked by crosses) using a well-suited linear extrapolation to the data points. Obviously,  $U_{c1}$  strongly depends on  $J$  (as seen already in Fig. 6). However, when  $\Delta$  is plotted versus  $\Delta_b$  [see Fig. 8(a)] the different lines lie ever closer to each other at large  $J$  and the critical value of the bare gap,  $\Delta_b^{c1} \equiv U_{c1} - 2J$ , approaches a constant value,  $W_1 = 4.8$ . This is also demonstrated in Fig. 8(b). For large  $J \gg J_{c1}^*$ , the critical interaction  $\Delta_b^{c1}$  (solid red line) is  $J$ -independent. Consequently,  $\Delta_b$  serves as measure for Mottness, in the sense that  $W_1 - \Delta_b$  quantifies the distance to the MIT at  $U_{c1}$  ( $\Delta_b^{c1}$ ). Thus, the larger  $\Delta_b$ , the closer the system is to the MIT and the stronger the influence of Mottness. We demonstrate that this idea also works for an mS: for  $J > J_{c1}^*$ ,  $\Delta_b^{c2} = U_{c2} - 2J$  approaches a constant value  $W_1 = 6.3$  [see dashed black line in Fig. 8(b) and  $\times$ -signs in Fig. 8(c)]. We thus switch from  $U$  to  $\Delta_b(J, U)$  as independent parameter in the following to quantify Mottness. However, we note that for  $J < J_{c1}^*$ ,  $\Delta_b^{c1}$  and  $\Delta_b^{c2}$  do still depend on  $J$ , thus  $\Delta_b$  breaks down as a simple measure for Mottness for small  $J$  in the above sense.

The reason for the  $\Delta_b^{c,i}$  with  $i = 1, 2$  becoming a constant for large  $J$  can again be roughly understood by simply looking at the local multiplet structure, where for  $J > U/2$  the excited levels  $h$  and  $e1$  actually pass across  $g1$  (see discussion at end of Sec. 2.6.1). Therefore one may expect a qualitative change of behavior at  $\Delta_b = U - 2J \sim \text{const}$ , as already mentioned in Sec. 4.1.

The finite offset for  $\Delta_b^{c1}$  can be explained with the Hubbard criterion [88] for the breakdown of the Mott insulating state, which uses  $\Delta = \Delta_b - \tilde{W}(J) \equiv 0$  to conclude that  $\Delta_b^{c1} \equiv \tilde{W}(J)$ : the system becomes metallic when the effective kinetic energy in the system,  $\tilde{W}(J)$ , is large enough to overcome the energy cost of hopping, given by the energy scale of the bare gap  $\Delta_b$ .  $\tilde{W}(J)$  sets the scale for the dispersion of the Hubbard bands and can be regarded as the effective bandwidth of the system. As shown in Fig. 8(b),  $\tilde{W}(J)$  has a large value  $\tilde{W}(0) = 7.3$  at  $J = 0$  and decreases with increasing but small  $J$ , approaching a constant  $W_1 = 4.8$  for sizeable  $J > J_{c1}^*$ . From Fig. 2 we know that at the SU(6) symmetric point  $J = 0$  the atomic excitation spectrum becomes more degenerate:  $g2$  becomes degenerate with  $g1$ , and thus also a true ground state; furthermore, all three excited levels  $h$ ,  $e1$ , and  $e2$  become degenerate. Accordingly, the widths

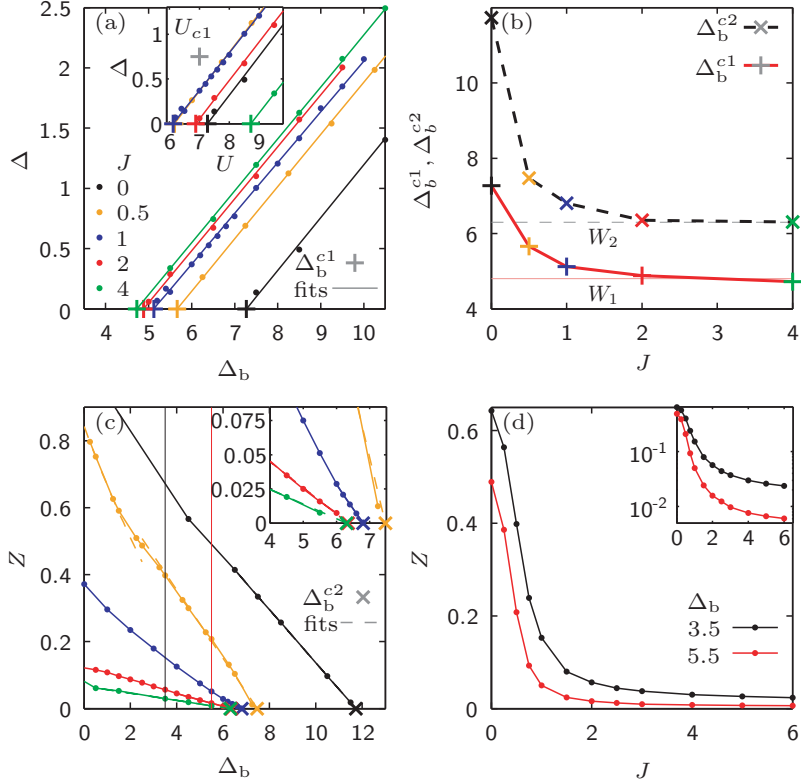


Figure 8: (a) Mott insulating gap,  $\Delta$ , as a function of the bare gap,  $\Delta_b = U - 2J$ , for several values of  $J$ . Each dot on the curves represents a DMFT+NRG data point using iS. The lines are linear fits from which the critical  $\Delta_b^{c1}$  values (pluses) are defined as  $\Delta(\Delta_b^{c1}) = 0$ . The inset shows the same data as a function of  $U$ . (b)  $\Delta_b^{c1}$  and  $\Delta_b^{c2}$  as functions of  $J$ : both first decrease roughly exponentially at small  $J < J_{c1}^*$  [see also Sec. 4.7] and then approach fixed values,  $W_1 = 4.8$  (thin solid red line) and  $W_2 = 6.3$  (thin dashed grey line), respectively, at large  $J > J_{c1}^*$ . (c)  $Z$  is plotted as a function of  $\Delta_b$  to disentangle the Janus-faced behavior of Fig. 6(a): the slope of  $Z$  decreases with increasing  $J$ , while  $\Delta_b^{c2} = W_2$  is  $J$ -independent for sizeable  $J > J_{c1}^*$  (and grows with decreasing  $J$  for  $J < J_{c1}^*$ ). Thus  $Z$  is small far away from the MIT due to Hundness rather than Mottness. The dashed yellow lines are quadratic and linear fits to the  $J = 0.5$  behavior of  $Z$  at small  $U$  and larger  $U$ , respectively. The inset is a zoom of the  $\Delta_b^{c2}$ -behavior. (d)  $Z$  is plotted as a function of  $J$ , for two fixed values of  $\Delta_b$ , indicated by the thin black and red lines in (c). Inset: same data in a semilog-plot of  $Z$ , revealing its roughly exponential decrease with increasing  $J$  for  $J < J_{c1}^*$ , whereas  $Z$  is very small but rather constant for  $J > J_{c1}^*$ .

of the Hubbard bands, i.e.  $\tilde{W}(J)$ , are larger at small  $J$ , because more hopping processes are allowed than for  $J > J_{c1}^*$ . In contrast, sizeable  $J$  favors high-spin states, reducing the atomic ground state degeneracy by quenching its orbital fluctuations and blocking many excitations. We note that a similar analysis was performed in Refs. [47, 50].

As in Ref. [47], we conclude that the non-monotonic behavior of  $U_{c1}$  can be summarized as follows: with growing  $J$ ,  $U_{c1}$  decreases at small  $J$  due the reduction of the kinetic energy by orbital blocking, whereas it increases again at large  $J$ , due to the reduction of  $\Delta_b$  by reducing the energy cost for the double occupancy of *different* orbitals. The turnaround occurs around  $J \sim 1$ , i.e. when  $J$  is on the order of the lattice hopping,  $t = 1$ . At the same time, as we point out at the end of Sec. 2.6.1, the non-monotonic behavior in  $U_{c1}$  can also be directly linked to a qualitative change in the underlying multiplet structure: the turn-around of  $U_{c1}$  coincides with the point in the parameter regime where the ‘excited’ levels  $h$  and  $e1$  pass across the ‘low-energy’ level  $g2$  in the metallic regime  $J > U_{c1}/6$ . This occurs when  $J \gtrsim 1$ . The behavior of  $U_{c2}$ , which is similar to  $U_{c1}$ , will be revisited and explained in Sec. 4.8 in the context of SOS.

#### 4.6. Hundness as origin of strong correlations

In contrast to previous studies, we now use  $\Delta_b$  as a measure for Mottness in Fig. 8(c,d) to disentangle the Janus-faced effects of  $J$  in  $Z$  and to analyze the “pure” effect of Hundness for strong correlations.

Fig. 8(c) shows  $Z$  versus  $\Delta_b$  for various values of  $J$ . We observe that, as visible for  $J = 0.5$ , the reduction in  $Z$  with  $\Delta_b$  first follows a quadratic behavior for small  $\Delta_b < 4J$  (which coincides with  $U < 6J$ ) followed, as visible for all values of  $J$ , by a linear behavior for moderate  $\Delta_b$  up to  $\Delta_b^{c2}$  (for  $J = 0.5$  this behavior is illustrated by fits, shown as the upper and lower dashed yellow lines, respectively). For  $J > J_{c1}^*$ ,  $\Delta_b^{c2}$  is  $J$ -independent [see inset of Fig. 8(c)], and  $W_2 - \Delta_b$  again measures the distance to the MIT.

For fixed  $\Delta_b$ , we observe in Fig. 8(c) that increasing  $J$  reduces  $Z$ , with the decay in  $Z$  significantly slowed down for  $J > J_{c1}^*$  (see inset).

The data along the thin red and black vertical lines is further summarized in Fig. 8(d). Note that the curve for  $\Delta_b = 5.5$  already proceeds midway in between  $U_{c1}$  and  $U_{c2}$  in the coexistence region in Fig. 5 for large  $J$  (e.g., see intercept at  $J = 0$  for their linear extrapolation), whereas  $\Delta_b = 3.5$  is still in the metallic phase.

Interestingly, for fixed  $\Delta_b$ , the overall suppression of  $Z$  with increasing  $J$  is more pronounced for smaller  $\Delta_b$ , where the values of  $Z$  are still very large for small  $J$ , but strongly reduced for large  $J$  [compare e.g. the  $Z$  values following the thin vertical lines for  $\Delta_b = 3.5$  and  $\Delta_b = 5.5$  in Fig. 8(c) or compare black and red curve in Fig. 8(d)]. This behavior can be inferred from the important insight that increasing  $J$  reduces the *slope* of  $Z$  when plotted as a function of  $\Delta_b$  (or  $U$ ) in Fig. 8(c) for *all*  $J > 0$ , while  $\Delta_b^{c2}$  is first reduced and then approaches a fixed value. As another major result of this work we thus summarize: *for sizeable  $J$ ,  $Z$  is strongly lowered also far from the MIT, at small  $\Delta_b$ , because Hundness promotes the reduction of the slope of  $Z$ .* The latter effect holds for *any* nonzero  $J$  [yellow, blue, red and green curve in Fig. 8(b)], even independently of the fact whether  $\Delta_b$  is a valid measure of Mottness (green and red curve) or not (yellow curve). Therefore, *Hundness, i.e. scenario (ii), is the origin of strong correlations in the Hund-metal regime far from the MIT at  $n_d = 2$ .*

In the next section, we focus also on small  $J < J_{c1}^*$ . As seen in Fig. 8(d), in this regime,  $Z$  is reduced roughly exponentially with increasing  $J$  (see also inset). However, here, we cannot fully disentangle the Janus-faced behavior of  $Z$  using  $\Delta_b$ .

#### 4.7. Spin-orbital separation in the $U$ - $J$ phase diagram

In order to better understand the strong reduction of  $Z$  at small  $J$  and to reveal the physical nature causing the low  $Z$  for  $J > J_{c1}^*$ , we now systematically analyze the underlying DMFT+NRG real-frequency spectral data in the metallic (and coexistence) region of the  $U$ - $J$  phase diagram. In particular, we consider  $\chi''_{\text{orb}}(\omega)$  and  $\chi''_{\text{sp}}(\omega)$ , the imaginary parts of the dynamical impurity orbital and spin susceptibilities, defined in Eqs. (6), the local spectral function  $A(\omega)$ , and the imaginary part of the self-energy,  $\text{Im} \Sigma(\omega)$ , defined in Eqs. (A.4). Similar to Ref. [33], we plot  $\chi''_{\text{orb}}(\omega)$  and  $\chi''_{\text{sp}}(\omega)$  in Fig. 9(a) and Fig. 10(a) to deduce  $T_K^{\text{orb}}$  and  $T_K^{\text{sp}}$  from their respective maxima.  $A(\omega)$  is plotted in Fig. 9(b-d) and Fig. 10(b-d), and  $\text{Im} \Sigma(\omega)$  in Fig. 9(e,f) and Fig. 10(e,f). In Fig. 9  $\Delta_b = 3.5$  is fixed and  $J$  is varied, while in Fig. 10  $J = 2$  is fixed and  $U$  ( $\Delta_b$ ) is varied [the latter is similar to Fig. 6(c), there for  $J = 1$ ].

SOS, i.e.  $T_K^{\text{orb}} \gg T_K^{\text{sp}}$ , occurs in the whole metallic regime for nonzero  $J$ , as seen in Fig. 9(a) and Fig. 10(a). It is a generic consequence of finite Hund’s coupling in particle-hole asymmetric *multi*-band systems, as anticipated early on [89]. Since  $T_K^{\text{sp}}$  is finite, the ground state is a FL [see thin grey  $|\omega|^1$ -guide-to-the-eye lines in Fig. 9(a) and Fig. 10(a)] for all values of  $U$  and  $J$  at  $n_d = 2$ , independently of the proximity to the MIT. This strongly contradicts the spin-freezing phase scenario proposed in Ref. [51], but confirms the expectations of Refs. [6, 7, 14, 53].

For fixed  $\Delta_b$ , the SOS regime opens up with increasing  $J$  [the maxima of  $\chi''_{\text{sp}}(\omega)$  are shifted to smaller  $|\omega|$  in Fig. 9(a)]. This effect is accompanied by the formation of a shoulder at  $\omega < 0$ , and a weak kink at  $\omega > 0$  in  $A(\omega)$ , which narrow the top of the QPP [see Fig. 9(b-d)], and reveal a strong particle-hole asymmetry in the system. Accordingly, the imaginary part of the self-energy,  $\text{Im} \Sigma(\omega)$ , develops a pronounced shoulder (bump) in the SOS regime at  $\omega < 0$  [Fig. 9(e)], and a kink at  $\omega > 0$  [Fig. 9(e)], as well. Note that the kink is only visible for  $J > 1$ , while at smaller  $J$ ,  $\text{Im} \Sigma(\omega)$  seems to follow apparent power-laws (as indicated by the

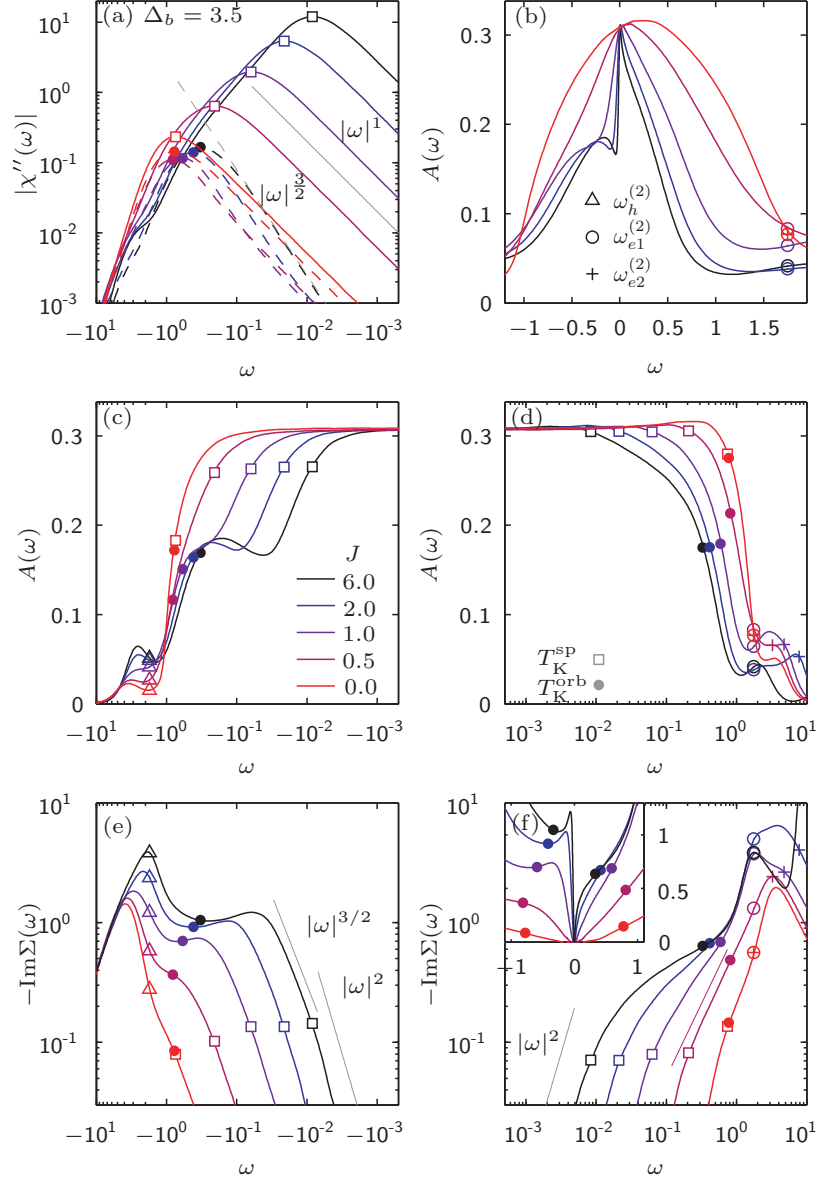


Figure 9: (a) The imaginary parts of the dynamical impurity orbital and spin susceptibilities,  $|\chi''_{\text{orb}}(\omega)|$  (dashed) and  $|\chi''_{\text{sp}}(\omega)|$  (solid), (b-d) the local spectral function  $A(\omega)$ , and (e,f) the imaginary part of the self-energy,  $\text{Im}\Sigma(\omega)$ , for fixed  $\Delta_b = 3.5$  and various choices of  $J$ . (a)  $T_K^{\text{orb}}$  (filled circles) and  $T_K^{\text{sp}}$  (open squares) are defined from the maxima of  $\chi''_{\text{orb}}(\omega)$  and  $\chi''_{\text{sp}}(\omega)$ , respectively. With increasing  $J > 0$ , an SOS regime clearly develops,  $T_K^{\text{orb}} > |\omega| > T_K^{\text{sp}}$ , with complex NFL behavior.  $\chi''_{\text{orb}}(\omega)$  follows an apparent  $|\omega|^{3/2}$  power law in the SOS regime (dashed grey guide-to-the-eye line), which we believe is just a cross-over behavior (see discussion in Sec. 5.5). Below  $T_K^{\text{sp}}$ , the expected  $|\omega|^1$  FL power-law behavior sets in, indicated by a solid grey guide-to-the-eye line. (b,c,d) With increasing  $J$  a  $SU(6)$  Kondo resonance in  $A(\omega)$  splits into a  $SU(3)$  Kondo peak (shoulder for  $\omega < 0$  and kink for  $\omega > 0$ ) and a sharp  $SU(2)$  Kondo QPP, reflecting two-stage screening of orbital and spin degrees of freedom due to SOS. These features are shown on (b) linear and (c,d) logarithmic frequency scales for (c) negative and (d) positive frequencies. (e,f)  $\text{Im}\Sigma(\omega)$  is plotted versus (e) negative and (f) positive frequencies. Solid grey guide-to-the-eye lines indicate  $|\omega|^2$  FL power-law behavior and apparent  $|\omega|^{3/2}$  behavior at  $\omega < 0$ , the magenta guide-to-the-eye line in (f) shows an apparent fractional-power law at  $\omega > 0$  for  $J = 0.5$ . The latter fractional power laws presumably originate just from a cross-over behavior. The symbols, as specified in the legend in (b), correspond to the local multiplet excitations listed in Eqs. (3a). For  $J = 0$ , triangles and pluses also correspond to the transition frequencies in Eqs. (3b), i.e to  $\tilde{\omega}_h$  and  $\tilde{\omega}_{e2}$ .



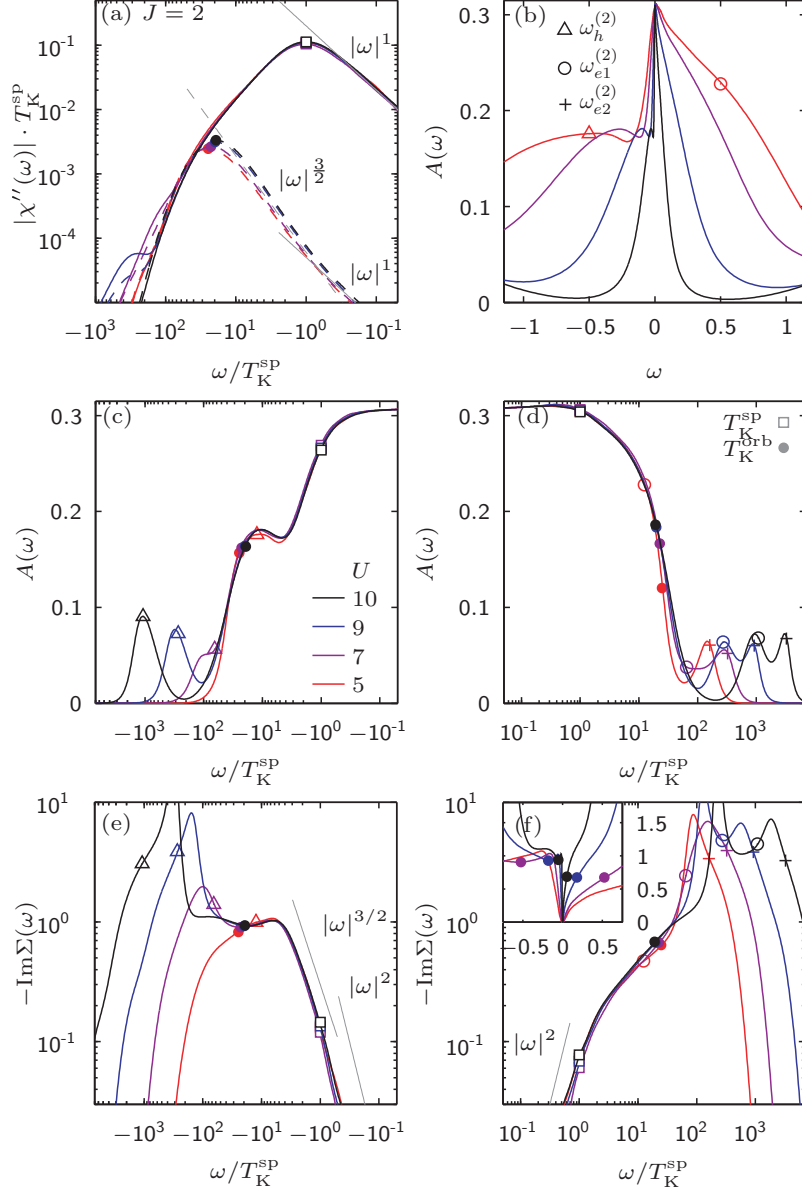


Figure 10: Similar data as in Fig. 9, but for fixed  $J = 2$  and various choices of  $U$  ( $\Delta_b$ ), plotted as a function of  $\omega/T_K^{\text{SP}}$  on a logarithmic frequency scale in (a,c,d,e,f), and in (b) as a function of  $\omega$  on a linear frequency scale. All curves are identical for  $|\omega/T_K^{\text{SP}}| < T_K^{\text{orb}}/T_K^{\text{SP}} \approx 20$  while, nevertheless, the low-energy physics moves to smaller energies with increasing  $U$  on a linear scale (panel b). (c-f) Thus, “QP Hund features” in  $A(\omega/T_K^{\text{SP}})$  and  $\text{Im}\Sigma(\omega/T_K^{\text{SP}})$  are independent of  $U$  in both the rescaled SOS regime, and the rescaled FL regime for  $|\omega| < T_K^{\text{SP}}$  (narrow, sharp peak in  $A(\omega T_K^{\text{SP}})$ ). The symbols, as specified in the legend in (b), correspond to the local multiplet excitations listed in Eqs. (3a).

magenta guide-to-the-eye line for  $J = 0.5$  in Fig. 9(f) and observed in Fig. 3(b,e) of Ref. [33]). For  $J = 0$ , the QPP is formed by one broad  $SU(6)$  Kondo resonance. With increasing  $J$ , this Kondo resonance is split into a narrow  $SU(2)$  spin Kondo resonance on top of a wider  $SU(3)$  orbital Kondo resonance (e.g., the shoulder), corresponding to spin and orbital screening, respectively [see Fig. 13(a) for a schematic sketch]. The orbital features become strongly particle-hole asymmetric with increasing  $J$ , with lesser effects on the spin resonance. Thus, SOS is manifest in a two-tier QPP with a wide base and a narrow “needle” of (half-) width  $T_K^{\text{orb}}$  and  $T_K^{\text{sp}}$ , respectively. We see from the behavior of  $T_K^{\text{orb}}$  in Fig. 9(a) that the “full” width of the QPP is rather stable with increasing  $J$  (at least for negative frequencies). In contrast, the width of the needle strongly reduces with  $J$  [compare e.g. red and black curves in Fig. 9(b-d)].

We note that the orbital and spin screening in the 3HHM are non-trivial screening processes that differ from standard  $SU(N)$  Kondo-type screening processes. The Kondo model corresponding to the 3HHM with specific representations of the impurity spin and orbital operators has been worked out in Refs. [31, 90], e.g. resulting in a ferromagnetic bare spin coupling. In particular, a complex, protracted RG flow has been revealed where orbital and spin degrees of freedom are *not* decoupled, leading to a subtle spin-orbital Kondo effect (see also Fig. 13): first, at higher energies, the intermediate-coupling NFL fixed point of an underlying effective 2 (spin)-channel  $SU(3)$  Coqblin-Schrieffer model is reached, where the ferromagnetic spin coupling is quenched. Then, at much lower energies, the spin coupling renormalizes to an anti-ferromagnetic value and the RG flow results in a strong-coupling FL fixed point. For  $J = 0$ , the Kondo model reduces to the single-channel antiferromagnetic  $SU(3 \times 2)$  Coqblin-Schrieffer model. Therefore, when for  $J > 0$ , we refer to a  $SU(3)$  orbital and a  $SU(2)$  spin Kondo resonance, or, for  $J = 0$ , to a  $SU(6)$  Kondo resonance, we have this non-trivial spin-orbital Kondo effect in mind.

Fig. 10 shows similar data as in Fig. 9, but now for a fixed  $J$  and different values of  $U$  ( $\Delta_b$ ), plotted as a function of  $\omega/T_K^{\text{sp}}$  in (a,c,d,e,f) and  $\omega$  in (b). Here,  $U$  affects  $T_K^{\text{orb}}$  and  $T_K^{\text{sp}}$  in the same way: their ratio,  $T_K^{\text{orb}}/T_K^{\text{sp}} \approx 20$ , is essentially independent of  $U$ , such that the curves in Fig. 10(a) lie on top of each other for  $|\omega| < T_K^{\text{orb}}$  (see also the discussion of Fig. 12, and the expressions for the orbital and spin Kondo scales derived in Ref. [31]). As a consequence, the shapes of the QPPs in  $A(\omega)$  and the self-energies  $\text{Im} \Sigma(\omega)$  are scale invariant for  $|\omega| \leq T_K^{\text{orb}}$ , too, when plotting both quantities as a function of  $\omega/T_K^{\text{sp}}$  [see Fig. 10(c,d) and (e,f), respectively], reminiscent of the universal behavior in the single-band Hubbard model. The reason for this is that the ratio  $T_K^{\text{orb}}/T_K^{\text{sp}}$  is constant in the underlying Kondo model [31] of the 3HHM (for a fixed  $n_d = 2$  corresponding to a certain spin and orbital operator representation). This universal behavior of the Kondo scales is not changed by the DMFT self-consistency: the SOS is characteristic of impurity physics, i.e. it also emerges in the impurity AHM in the absence of an MIT [33]. The DMFT self-consistency just adjusts the overall width of the QPP, by affecting the value of  $T_K^{\text{orb}}$ , but not its internal structure, governed by  $T_K^{\text{orb}}/T_K^{\text{sp}}$ . In Fig. 10(b), on a linear frequency scale, the SOS features are more pronounced for larger  $T_K^{\text{orb}}$ , i.e. smaller  $U$ , when compared to bare energy scales in the system.

We summarize the effect of spin-orbital separation at  $n_d = 2$  in Fig. 11. There we show the structure factor  $A(\epsilon_k, \omega)$ , as experimentally accessible by angle-resolved photoemission spectroscopy (ARPES), for  $J = 0$  [panel (a)] and  $J = 2$  [panel (b)]. Within DMFT,  $A(\epsilon_k, \omega)$  is directly obtained from the self-energy  $\Sigma(\omega)$ :  $A(\epsilon_k, \omega) = -\frac{1}{\pi} \text{Im} [\omega + \mu - \epsilon_k - \Sigma(\omega)]^{-1}$ . The QP dispersion (white curve) is defined as the solution to the equation  $\omega + \mu - \epsilon_k - \text{Re} \Sigma(\omega) = 0$  [91]. For fixed  $\omega$ , this trivially yields a single value for  $\epsilon_k$ , but not necessarily a unique value for  $\omega$  for fixed  $\epsilon_k$ . Considering the latter solution(s),  $E(\epsilon_k)$ , for given  $\epsilon_k$ , then for  $J = 0$ ,  $E$  shifts linearly with  $\epsilon_k$ , i.e. the band corresponding to the QPP is fully characterized by a linear FL dispersion relation with constant slope  $\frac{\partial E}{\partial \epsilon_k} \sim \frac{1}{m_{J=0}^*} \sim Z \sim T_K^{\text{sp}}$ , in the whole frequency regime plotted in Fig. 11(a). In contrast, for  $J = 2$ ,  $T_K^{\text{sp}}$  is reduced by more than one order of magnitude compared to  $J = 0$ . Thus  $\frac{\partial E}{\partial \epsilon_k} \sim \frac{1}{m_{J=2}^*}$  is constant only in a very small energy regime [as indicated by the black dashed line in the inset of Fig. 11(b)]. Further, this slope is much smaller than for  $J = 0$ , indicating a strong reduction of the effective mass,  $m^*$ , for finite  $J$  (due to Hund’s-coupling-induced strong correlations). Interestingly, when entering the SOS regime for frequencies  $|\omega|$  above the FL regime, the slope becomes steeper: the spin degrees of freedom become unscreened, the QPs thus “undressed” and the effective mass smaller. For  $\omega > 0$ , this change in the slope is manifest in a slight kink, followed by a rather constant behavior of  $\frac{\partial E}{\partial \epsilon_k}$ . For  $\omega < 0$ , the shoulder (bump), observed in  $A(\omega)$  and  $\text{Im} \Sigma(\omega)$ , leads to a somewhat artificial s-shaped dispersion,  $E$ ,

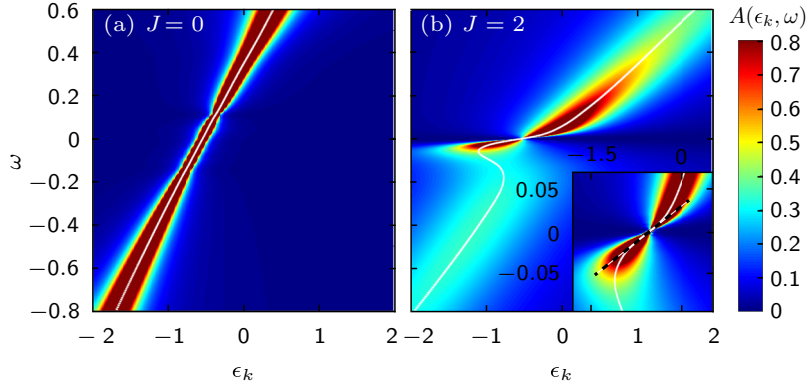


Figure 11: The structure factor,  $A(\epsilon_k, \omega)$ , at  $\Delta_b = 3.5$  and  $T = 0$  for (a)  $J = 0$  and (b)  $J = 2$ . The white curves show the QP dispersion,  $E$  (see text for a definition). The inset in (b) zooms into the FL regime at  $J = 2$ . FL behavior is indicated by the black dashed guide-to-the-eye line.

including a divergence in the slope and negative effective masses (due to the Bethe lattice). In this regime, three maxima are observed in  $A(\epsilon_k, \omega)$  at fixed  $\epsilon_k$ . All these SOS features of  $A(\epsilon_k, \omega)$  are completely absent for  $J = 0$ .

#### 4.8. Spin-orbital separation as origin of low $Z$

We are now ready to reveal the connection of SOS and  $Z$ . We corroborate and summarize our findings of the previous Sec. 4.7 by directly analyzing the behavior of  $T_K^{\text{orb}}$  and  $T_K^{\text{sp}}$  as functions of  $\Delta_b$  and  $J$ . Importantly, we expect, as pointed out earlier [see Luttinger pinning [82, 83], here with  $A(\omega = 0) = 1/\pi$ ], that the width of the Kondo resonance scales linearly with the QP weight  $Z$ . As we will demonstrate below, in the Hund regime of  $J$ , this holds for the spin Kondo scale, i.e.  $Z \propto T_K^{\text{sp}}$  for  $J > J_{c1}^*$ .

We replot the data of Fig. 8(c,d) in Fig. 12, but now with focus on  $T_K^{\text{orb}}$  and  $T_K^{\text{sp}}$  instead of  $Z$  on a linear [Fig. 12(a,c)] and a semi-logarithmic [Fig. 12(b,d)] scale. For reference, we also replot our  $Z$  data, but rescale it by a factor  $a(J) \equiv T_K^{\text{sp}}/Z$  [indicated by the dotted grey curve in Fig. 12(c)], which is essentially the same for all values of  $\Delta_b$ . Fig. 12(a,b) show that for fixed  $J$ ,  $T_K^{\text{sp}}$  and  $Z$  have the same dependence on  $\Delta_b$ , i.e.  $T_K^{\text{sp}} = a(J)Z$ , with a proportionality factor,  $a(J) \simeq 0.36$ , for  $J > J_{c1}^*$  and increasing values of  $a(J) > 0.36$  for decreasing  $J < J_{c1}^*$  [see  $a(J)$  in Fig. 12(c)]. Analogously, for fixed  $\Delta_b$  and varying but sizeable  $J > J_{c1}^*$  in Fig. 12(c,d), we find that  $T_K^{\text{sp}} \approx 0.36 Z$ .

We thus conclude, as a major result of this work, that *the reduction of  $Z$  in the Hund-metal regime of Fig. 1 at  $n_d = 2$  is directly linked to the reduction of  $T_K^{\text{sp}}$  due to SOS*, and that all insights gained for  $Z$  hold for  $T_K^{\text{sp}}$ , and vice versa, specifically so for sizeable  $J$ . Based on the knowledge that the 3HHM at  $n_d = 2$  has a FL ground state, it is of course expected that  $Z$  is a measure of the coherence scale using Landau's FL theory (see Luttinger theorem above), as e.g. also pointed out in Refs. [47, 50, 53]. In this work, we have now demonstrated *quantitatively* that and how  $Z$  and  $T_K^{\text{sp}}$  are connected. Additionally, we have conclusively identified the origin of low  $Z$  and the physical mechanism causing the bad-metallic transport – spin-orbital separation.

Fig. 12(a,b) demonstrate again the important insight that SOS is absent for  $J = 0$  for all values of  $\Delta_b$  ( $U$ ):  $T_K^{\text{orb}} = T_K^{\text{sp}}$  (black filled big circles and black open squares lie approximately on top of each other; the small difference is due to the fact that  $|\chi''_{\text{orb}}(\omega)|$  was obtained from a calculation with different NRG parameters, i.e. stronger truncation due to numerical cost; we checked that using the same (stronger) truncation leads to exactly  $T_K^{\text{orb}} = T_K^{\text{sp}}$ ). But also here,  $T_K^{\text{orb}} = a(J)Z$  with  $a(J) > 1$  [see dotted grey line in Fig. 12(c)] due to the FL ground state. In contrast, for nonzero  $J$ , SOS with  $T_K^{\text{orb}} \gg T_K^{\text{sp}}$  occurs: with increasing  $J$ ,  $T_K^{\text{orb}}$  is only moderately reduced, while  $T_K^{\text{sp}}$  and thus  $Z$  are strongly reduced (at fixed  $\Delta_b$ ). More importantly, *the slope of the linear function  $T_K^{\text{sp}}(\Delta_b)$  and thus  $Z(\Delta_b)$  is strongly reduced with increasing  $J$*  [solid lines in Fig. 12(a)], *while the slope of the linear function  $T_K^{\text{orb}}(\Delta_b)$  is approximately  $J$ -independent* [dashed lines in

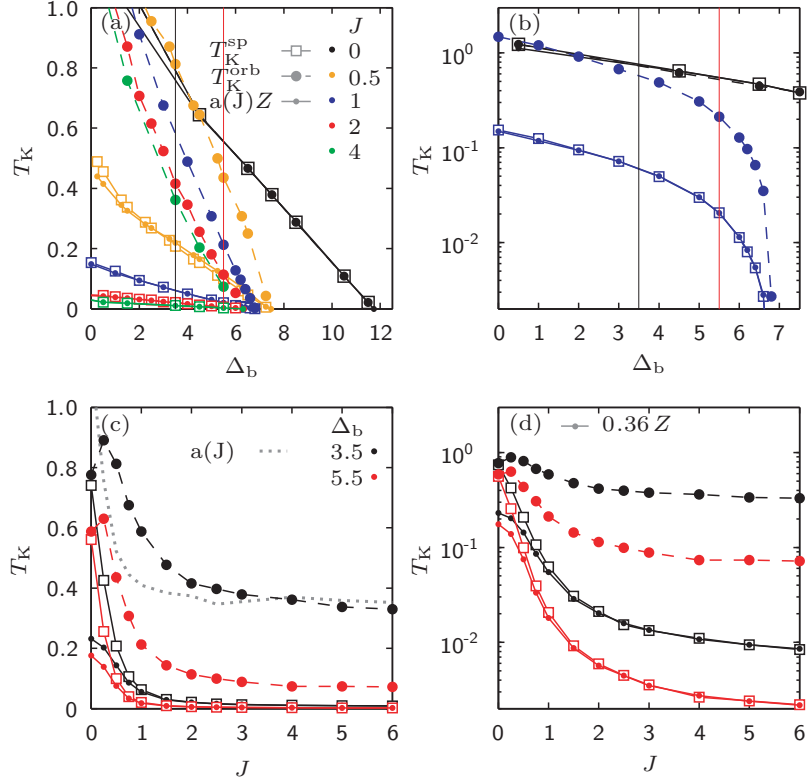


Figure 12: The orbital Kondo scale,  $T_K^{\text{orb}}$  (dashed curves with big filled circles), the spin Kondo scale,  $T_K^{\text{sp}}$  (solid curves with open squares), and the rescaled QP weight,  $a(J)Z$  (dotted grey curve), plotted as a function of  $\Delta_b$  for various values of  $J$  using (a) linear scale and (b) logarithmic scales for the y-axis. Both  $T_K^{\text{orb}}$  and  $T_K^{\text{sp}}$  decrease linearly with  $\Delta_b$ , with a larger slope for  $T_K^{\text{orb}}$  if  $J > 0$ . The slope of  $T_K^{\text{sp}}$  strongly decreases with  $J$ , whereas the slope of  $T_K^{\text{orb}}$  is rather  $J$ -independent. SOS,  $T_K^{\text{orb}} \gg T_K^{\text{sp}}$ , occurs for all  $\Delta_b \leq \Delta_b^{c2}$  at  $J > 0$ , but is more prominent at smaller  $\Delta_b$ . (c,d) Same quantities as in (a,b) now plotted as a function of  $J$  for two values of  $\Delta_b$  [indicated by vertical lines in (a)]. When  $J$  is turned on, both  $T_K^{\text{orb}}$  and  $T_K^{\text{sp}}$  decrease strongly, but differently, opening up the SOS regime at small  $J < J_{c1}^*$ , and saturating at  $J > J_{c1}^*$ .

Fig. 12(a)]. Far away from the MIT, at small to moderate  $\Delta_b$ , this leads to a broad SOS regime which is extended from very low up to very large energy scales (comparable to the bare atomic excitations). When approaching the MIT with increasing  $\Delta_b$ , both  $T_K^{\text{orb}}$  and  $T_K^{\text{sp}}$  decrease linearly, but with different slopes: the SOS regime shrinks and is shifted to lower energies [compare values of  $T_K^{\text{orb}}$  and  $T_K^{\text{sp}}$  at  $\Delta_b = 3.5$  (black vertical line) and  $\Delta_b = 5.5$  (red vertical line) for a fixed  $J > 0$  in Fig. 12(a); see also the black ( $\Delta_b = 3.5$ ) and red ( $\Delta_b = 5.5$ ) curves in Fig. 12(c): for  $J > J_{c1}^*$ , the distance between dashed and solid line is smaller for larger  $\Delta_b = 5.5$ ]. During this process the ratio  $T_K^{\text{orb}}/T_K^{\text{sp}}$  first remains constant, as can be observed on a semi-logarithmic scale in Fig. 12(b) (blue curves). Very close to the MIT both  $T_K^{\text{orb}}$  and  $T_K^{\text{sp}}$  (and thus also  $Z$ ) vanish together. Clearly, the DMFT self-consistency affects the QPP as a whole and finally destroys the QPP – including its internal structure – at the MIT.

We now also discuss in more detail the behavior of the Kondo scales and  $Z$  for fixed  $\Delta_b$  and varying  $J$  [see Fig. 12(c,d)]. At small  $J$ , spin-orbital separation is turned on. The broad  $SU(6)$  Kondo QPP with large  $T_K^{\text{orb}} = T_K^{\text{sp}}$  splits very abruptly with increasing  $J$  into a  $SU(3)$  and a  $SU(2)$  Kondo resonance, reducing, after a slight decrease of  $T_K^{\text{orb}}$ , both  $T_K^{\text{sp}}$  and  $T_K^{\text{orb}}$ . As  $T_K^{\text{sp}}$  is affected much stronger, the ratio  $T_K^{\text{orb}}/T_K^{\text{sp}}$  grows with increasing  $J$ , eventually saturating for sizeable  $J > J_{c1}^*$ . In the latter large- $J$  regime, we observe that both  $T_K^{\text{orb}}$  and  $T_K^{\text{sp}}$  ( $Z$ ) are only slightly reduced with increasing  $J$  [as already observed in Fig. 8(d) for  $Z$ ], and  $a(J) \approx 0.36$  is  $J$ -independent, i.e. SOS is fully developed and quite stable for sizeable  $J$ , and thus  $Z$  is low. Therefore, the main reason for lowering  $T_K^{\text{sp}}$  and  $Z$  upon turning on  $J$  can be heuristically ascribed to the

following effect: the ground state multiplet degeneracy is lifted by blocking orbital fluctuations through the selection of high-spin multiplets, as discussed in Sec. 2.6.1. The resulting orbital degeneracy is still much larger than the spin degeneracy. Consequently, local Kondo-type screening of orbital degrees of freedom occurs at much higher scales than spin screening.  $T_K^{\text{orb}}$  is only moderately whereas  $T_K^{\text{sp}}$  and thus  $Z$  are strongly lowered. As mentioned before, a quantitative analysis for a corresponding Kondo model is given in Refs. [31, 90]. As the degeneracy of the FL ground state changes when  $J$  is turned on, the factor  $a(J)$  is strongly reduced, as well, in the small- $J$  regime [see grey dotted curve in Fig. 12(c)]. The reduction of  $Z$  with increasing  $J$  is thus less severe than the reduction of  $T_K^{\text{sp}}$  (compare solid lines with small dots to solid lines with open squares).

Since  $Z \propto T_K^{\text{sp}}$ , also the behavior of  $\Delta_b^{c2}(U_{c2})$  is determined by SOS. For  $J \ll J_{c1}^*$ ,  $T_K^{\text{sp}}$  and thus  $\Delta_b^{c2}(U_{c2})$  first decrease with increasing  $J$  [see Fig. 12(c) and Fig. 8(b), respectively]. For  $J > J_{c1}^*$ ,  $T_K^{\text{sp}}$  plotted as a function of  $\Delta_b$  essentially saturates, accordingly also  $\Delta_b^{c2}$  saturates [see black dashed curves in Fig. 6(a) and Fig. 8(b)]. This explains why  $U_{c2}$  behaves non-monotonously, similar to  $U_{c1}$ , and shows that the bare gap,  $\Delta_b$ , can be used as a measure of Mottness at sizeable  $J$  both for a mS and an iS.

Let us summarize the main conclusion of Sec. 4. *The main effect to induce strong correlations in the Hund metal regime of the 3HHM at  $n_d = 2$  is Hundness rather than Mottness, i.e. the very abrupt turning-on of spin-orbital separation in the presence of nonzero (sizeable)  $J$ , independently of the value of  $\Delta_b$ , thus also far from the MIT.* The MIT itself, which is purely induced by the DMFT self-consistency, is an additional but subleading effect in the system, that only further lowers the spin and orbital Kondo scales with increasing  $U$ . The formation of  $J$ -induced large spins is, in principle, a local process occurring on individual lattice sites. In contrast, the formation of a charge gap is a highly non-local process that needs to self-consistently incorporate the whole lattice dynamics (via a gapped hybridization function). As a consequence of Hundness, the nature of the incoherent transport is governed by ‘‘Hund metal physics’’ in the SOS regime at  $n_d = 2$ : large slowly fluctuating spins are non-trivially coupled to screened orbitals (see definition in Sec. 3.1).

But when SOS is a generic effect in the metallic regime of the 3HHM (and presumably of all particle-hole asymmetric degenerate multi-band Hund models), in which sense do Hund- and Mott-correlated systems then differ in nature?

#### 4.9. Hund- versus Mott-correlated bad metals

Indeed, for the 3HHM at fixed and sizeable  $J$ , the features occurring for instance in  $A(\omega)$ , differ, in principle, only quantitatively when  $U$  is varied: the Kondo scales shift as a function of  $U$ , but the qualitative structure of the QPP does not change. However, we argue that the ratio of the bare atomic scales and the Kondo scales (in particular  $T_K^{\text{orb}}$ ), or phrased differently, the ratio of the characteristic energy scale of the Hubbard bands and the overall width of the QPP, sets the framework for a meaningful characterization of Mott- and Hund-correlated systems: this ratio is much larger in Mott than in Hund systems (see Fig. 13), leading to qualitative different signatures, as demonstrated for temperature-dependent quantities in Ref. [37].

Hund metals (characterized by moderate  $U$ , but sizeable  $J$ ) are by definition far from the MIT. Their lowest bare atomic excitation scales,  $\omega_h$  and  $\omega_{e1}$  are small [see discussion following Eqs. (3b)]. The Hubbard bands still overlap for moderate values of  $U$  and form a broad incoherent background in a range estimated by  $\omega_{e2} - \omega_h$ , having  $\omega_h < 0 < \omega_{e1} < \omega_{e2}$ . While  $T_K^{\text{sp}}$  and thus  $Z$  are considerably reduced,  $T_K^{\text{orb}}$  is comparable to the bare atomic excitation scales. This implies a ratio of order one between  $T_K^{\text{orb}}$  and the bare atomic excitation scales [see Fig. 13(b)]. As a consequence, the incoherent SOS window,  $T_K^{\text{sp}} < |\omega| < T_K^{\text{orb}}$ , is broad and ‘‘Hund metal physics’’ is relevant in a large energy window in Hund metals. For instance, the temperature-dependent local spin susceptibility of a Hund metal shows Curie-like behavior in the incoherent regime revealing large localized spins [37]. The low  $Z$  of Hund metals thus implies spin localization but no charge localization. Impurity physics dominates.

Multi-band Mott systems (characterized by  $U$  being large compared to  $J$ ) are by definition close to the MIT. Their lowest bare atomic excitation scales,  $\omega_h$  and  $\omega_{e1}$  are large, thus the Hubbard bands are pronounced and well separated. Both Kondo scales are small and thus the QPP narrow. Together this implies that the bare atomic scales are much larger than  $T_K^{\text{orb}}$  [see Fig. 13(c)]. Further, the incoherent SOS window,  $T_K^{\text{sp}} < |\omega| < T_K^{\text{orb}}$ , is very small and ‘‘Hund metal physics’’ is almost not observable. Similar to

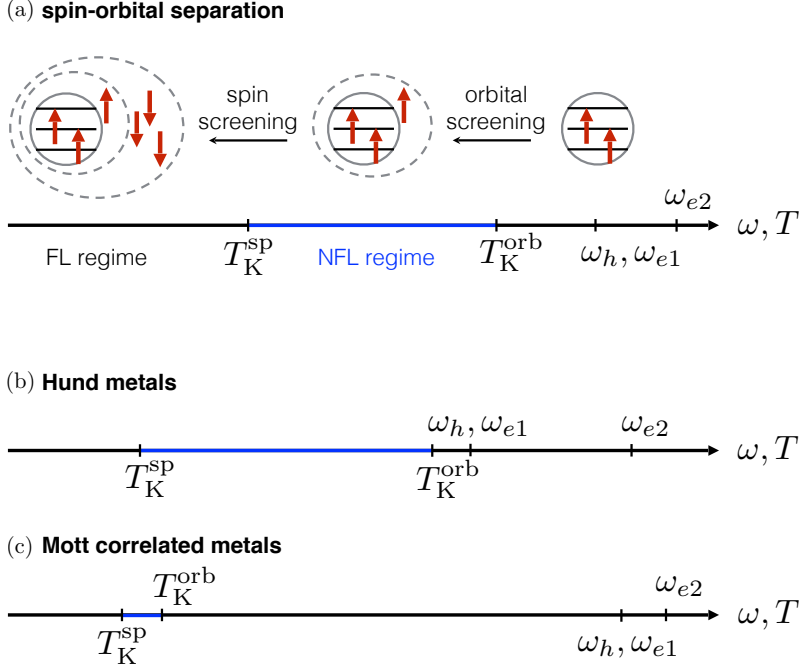


Figure 13: (a) Schematic depiction of the two-stage screening process of SOS at filling  $n_d = 2$ . First the orbital degrees of freedom are screened below the orbital Kondo scale,  $T_K^{\text{orb}}$ , by the formation of a large, effective, Hund’s-coupling induced  $3/2$ -spin including a bath spin degree of freedom. Then, at a lower spin Kondo scale,  $T_K^{\text{sp}}$ , this effective  $3/2$ -spin is fully screened by the three bath channels of the 3HHM (see also the discussion for Fig. 16 in Sec. 5.5). Incoherent NFL behavior is found for  $T_K^{\text{sp}} < |\omega|, T < T_K^{\text{orb}}$ , and FL behavior at energies below  $T_K^{\text{sp}}$ . (b) In Hund metals, bare atomic excitation scales,  $\omega_h$  and  $\omega_{e1}$ , and the overall width of the QPP,  $T_K^{\text{orb}}$ , are comparable in magnitude, while  $T_K^{\text{sp}}$  and thus  $Z$  are much smaller, opening a large relevant NFL regime in the system. (c) In Mott-correlated metals, we find  $T_K^{\text{sp}} \sim T_K^{\text{orb}} \ll \omega_h, \omega_{e1}$ , such that  $Z$  is reduced while SOS is not important.

one-band Mott systems,  $Z$  is low because charge fluctuations are suppressed. In sum, typical Mott physics, i.e. the DMFT self-consistency, dominates.

Finally, we note that the physics of Hund metals also strongly differs from that of generic one-band (or multi-band) Hubbard models (with  $J = 0$ ) which are far from the MIT. First, the latter are weakly correlated, whereas a Hund system is strongly correlated, despite being far away from the MIT. Second, SOS and thus incoherent ‘‘Hund metal physics’’ only occurs for particle-hole asymmetric *multi*-orbital systems with at least three-bands, fillings of  $1 < n_d < 2N_c - 1$  with  $n_d \neq N_c$ , and, most importantly, *nonzero*  $J$ .

## 5. Proximity to the half-filled MIT: Hundness versus Mottness at $2 < n_d < 3$

We now study the doping-dependence of the QP weight,  $Z$ , and of the electronic compressibility,  $\kappa_{e1} \equiv \frac{\partial n_d}{\partial \mu}$ . In particular, we demonstrate that SOS also occurs for  $2 < n_d < 3$ , and that it determines the low  $Z$ -behavior there, as well. In particular, we focus on the question how Mottness of type (iii), i.e. the MIT at  $n_d = 3$ , affects SOS and whether (i) Hundness or (iii) Mottness is the key player to induce strong correlations in the Hund-metal regime for  $n_d \gtrsim 2$ . Further, we will show that, for all parameters studied, no Hund’s-coupling-induced Fermi-liquid instabilities (negative compressibilities) occur near the half-filled MIT of the 3HHM, in contrast to suggestions in Ref. [58].

### 5.1. MIT at $n_d = 3$

As mentioned before, at half-filling  $n_d = 3$ ,  $U_c^{(3)}$  is much smaller than at other fillings. This is now explicitly demonstrated in Fig. 14(a), where we plotted  $A(\omega)$  at  $n_d = 3$ , and  $J = 1$  for various values of  $U$ ,

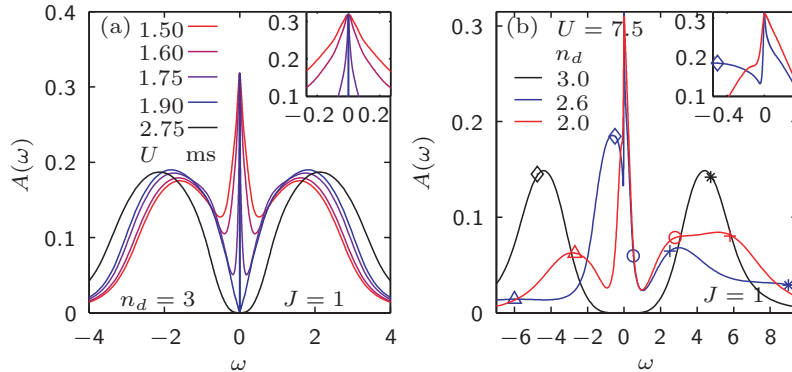


Figure 14: The zero-temperature local spectral function,  $A(\omega)$ , (a) for  $n_d = 3$ ,  $J = 1$  and various values of  $U$ , revealing an MIT with very small  $2 < U_{c2}^{(3)} < 2.25$ , and (b) for  $U = 7.5$ ,  $J = 1$  and varying  $n_d$ , revealing how the structure of the Hubbard side bands changes with filling. The five different markers represent the energy of the atomic multiplet excitations at given  $n_d$  [for  $n_d = 2$ , see Eqs. (3); for  $n_d = 3$ , see (5) for details and an assignment of the markers; for  $n_d = 2.6$ , the excitation energies are adapted to  $\mu(n_d)$ ]. The insets in (a,b) zoom into the QPP.

revealing the MIT at  $n_d = 3$ . Starting from an mS and using  $J = 1$ , we deduce from our real-frequency data the extrapolated value  $U_{c2}^{(3)} \sim 2.1 \pm 0.1$  at  $n_d = 3$ , which is strongly lowered compared to  $U_{c2}^{(2)} = 8.8$  at  $n_d = 2$ . While the region of low  $Z$  around  $n_d = 2$  reaches down to moderate values of  $U$  far below  $U_{c2}^{(2)}$ , i.e. far away from the MIT at  $n_d = 2$  in Fig. 1, these  $U$  values are still larger than  $U_{c2}^{(3)}$ . Therefore, Refs. [32, 50] have argued that the MIT at  $n_d = 3$  might be the reason for the low  $Z$  at moderate  $U \ll U_{c2}^{(2)}$  (even at  $n_d = 2$ ) – a statement that will be investigated in this section.

Further, we observe that also the structure of the Hubbard bands at  $n_d = 3$  differs completely from those at  $n_d = 2$  [compare red and black curves in Fig. 14(b)]. Specifically, in contrast to the  $n_d = 2$  results of Sec. 4, the spectral functions of Fig. 14(a) are particle-hole symmetric and the QPP has no shoulder, only slight kinks (see inset). In a pictorial language, in the case of  $n_d = 3$  for larger  $J$ , the only local multiplet is the  $3/2$  spin, with a singlet orbital character. Hence orbital Kondo physics is absent (or quenched up to energies on the order of the local multiplet excitations, i.e. the Hubbard bands). Therefore SOS features, as revealed for  $n_d = 2$ , are absent at half-filling.

### 5.2. Peak structure of Hubbard bands at $2 \leq n_d \leq 3$

At integer filling  $n_d = 2$  [red curve in Fig. 14(b)]  $A(\omega)$  consists of three peaks away from  $\omega = 0$ , while at  $n_d = 3$  it has only two pronounced peaks [black curve in Fig. 14(b)] that are particle-hole symmetric with respect to  $\omega = 0$ . The peak positions at finite frequency can be understood simply from the underlying atomic multiplet transition energies listed in Eqs. (3) for  $n_d = 2$  and Eqs. (5) for  $n_d = 3$ , assuming sizeable  $J$ .

In order to study scenarios (i) and (iii) at intermediate fillings,  $2 < n_d < 3$ , we start by investigating the structure of the Hubbard side bands for a filling,  $n_d = 2.6$  [blue curve in Fig. 14(b)]. We find that they are composed of all five types of atomic multiplet excitations from both the  $n_d = 2$  and  $n_d = 3$  ground states (5 peaks altogether) with their excitation energies adapted to  $\mu(n_d = 2.6)$ . Overall, at intermediate fillings,  $n_d = 2 \rightarrow 3$ , we find a smooth crossover in the structure of the Hubbard bands between their shape at  $n_d = 2$  and  $n_d = 3$ , respectively, caused by the smooth level transformation of eigenstates in the spectrum of the local Hamiltonian with changing  $\mu(n_d)$ , interchanging the ground state and varying the probability of one-particle multiplet excitations. In contrast, the shape of the Kondo resonances at  $\omega = 0$  change drastically when moving from  $n_d = 2$  to  $n_d = 3$ .

### 5.3. Spin-orbital separation at $2 < n_d < 3$ as the origin of low $Z$

Next we gain insights from the structure of the QPP with varying  $n_d$ . Similar to Fig. 4, we study the filling dependence of  $T_K^{\text{orb}}$  (dashed curves) and  $T_K^{\text{sp}}$  (solid curves) in Fig. 15(a) and its inset, now for three

different values of  $U$ . With increasing  $n_d$  (decreasing distance to half-filling,  $3 - n_d$ ), we observe an increasing separation of both Kondo scales, i.e. an increasing ratio of  $T_K^{\text{orb}}/T_K^{\text{sp}}$ , for all values of  $U$ . Thus SOS emerges for all fillings  $1 < n_d < 3$  in the metallic phase (as already indicated in Sec. 3 and the inset of Fig. 3(f) in Ref. [33]). We will show, however, that the “nature” of SOS changes with  $n_d$ . We remark that the behavior of  $T_K^{\text{sp}}$  plotted versus  $n_d$  in the inset of Fig. 15(a) corroborates earlier results of Ref. [7].

We begin by considering  $n_d = 1$ . We note that, in the absence of charge fluctuations, i.e. for the pure Kondo limit of the AHM, and if the energy scale of charge fluctuations is much larger than the Kondo scales in the 3HHM (or AHM), the Hund’s coupling  $J$  just becomes an energy offset and hence irrelevant, such that the  $SU(6)$  symmetry remains intact. Therefore it holds at  $n_d = 1$  that  $T_K^{\text{orb}} = T_K^{\text{sp}}$  independent of  $J$  (as demonstrated for the impurity AHM in the inset of Fig. 3(f) in Ref. [33] and for a Kanamori model in Fig. 6 of Ref. [76]). In the presence of charge fluctuations at higher energies, it still holds  $T_K^{\text{orb}} \approx T_K^{\text{sp}}$ . For example, in Fig. 15(a) for the self-consistent 3HHM,  $T_K^{\text{orb}}$  is shifted by about a factor of 2 towards larger values compared to  $T_K^{\text{sp}}$ , especially for lower values of  $U$  which encourages larger charge fluctuations (see e.g. black curves). For  $n_d$  near 1, the Kondo scales are large in energy and comparable to the bare atomic multiplet excitations scales. Thus, signatures of the QP and of bare atomic physics merge in  $\chi''_{\text{orb}}$  and  $\chi''_{\text{sp}}$  [see Fig. 16(d)]. As both quantities are affected differently by the charge fluctuations due to Hund’s coupling, their maxima,  $T_K^{\text{orb}}$  and  $T_K^{\text{sp}}$ , become shifted in energy with respect to each other.

As the local occupation increases towards  $n_d = 2$ , SOS is turned on, i.e. the impurity’s ground state  $SU(6)$  symmetry is split, and  $T_K^{\text{sp}}$  decreases by more than a factor of 2 for  $U = 2.25$  (solid black curve), of 5 for  $U = 5$  (solid blue curve) and of 10 for  $U = 7.5$  (solid red curve). At the same time,  $T_K^{\text{orb}}$  first slightly increases, reaching a maximum at around  $n_d = 1.5$ , and then (slightly) decreases again. For the largest  $U = 7.5$ , this leads to a reduction of  $T_K^{\text{orb}}$  by a factor of about 4 (dashed red curve; see also inset). There at  $n_d = 2$ , a strong minimum develops in  $T_K^{\text{orb}}$  and a shoulder in  $T_K^{\text{sp}}$ , respectively, with increasing  $U$  (red curves) due to the growing influence of the MIT at  $n_d = 2$ , lowering both Kondo scales (as explained in Sec. 4). For  $n_d \rightarrow 3$ , similar to the behavior in the inset of Fig. 3(f) in Ref. [33] for the impurity AHM,  $T_K^{\text{sp}}$  drops below the lowest relevant energy scale. On the contrary,  $T_K^{\text{orb}}$  grows up to energy scales comparable to the bare atomic scales in the system. This shows that orbital fluctuations are suppressed right away together with charge fluctuations. Hence no orbital Kondo physics can develop. What is left at half-filling, is a large spin  $S=3/2$  on the impurity that needs to be screened dynamically.

Figure 15(a) also shows  $Z$  (dotted curves) as a function of  $n_d$ . We find that, similar to the case of  $n_d = 2$  in Sec. 4,  $Z$  essentially follows the behavior of  $T_K^{\text{sp}}$  for  $2 \leq n_d < 3$  with  $T_K^{\text{sp}}/Z \approx 0.4$ , reflecting the fact that the ground state is a FL. Throughout this regime, *the small values of  $Z$  can be understood, via their proportionality to  $T_K^{\text{sp}}$ , to be a direct consequence of SOS, which ensures that  $T_K^{\text{sp}} \ll T_K^{\text{orb}}$* . For  $n_d \rightarrow 1$  the ratio  $T_K^{\text{sp}}/Z$  changes, due to strong changes in the ground state degeneracy [see deviations between dotted and solid curves for  $n_d < 2$  in the inset of Fig. 15(a)], reminiscent of the behavior of  $Z$  for small  $J$  in Fig. 12(c).

We remark that from the behavior of  $T_K^{\text{sp}}(n_d)$  we cannot deduce any indication for a relation between the physics at  $n_d = 2$  and the physics at  $n_d = 3$ . On the contrary, we see markedly different physical behavior for  $n_d = 3$  as compared to  $n_d = 2$ , e.g. with the absence of Kondo physics in the orbital sector, and in this sense the absence of SOS for  $n_d = 3$ . Further, the Hund-metal regime, (hatched area in Fig. 1) is special in that there we have not only SOS with  $T_K^{\text{sp}} \ll T_K^{\text{orb}}$ , but in addition also a dynamically generated, fairly small value of  $T_K^{\text{orb}}$ . Thus, conditions there are optimal for the Hund’s coupling to align spins in different orbitals without forming an orbital singlet from the outset, allowing for a non-trivial interplay between both spin and orbital degrees of freedom, which induces SOS. We thus argue that *the MIT at  $n_d = 3$  does not trigger the low  $Z$  around  $n_d = 2$* .

#### 5.4. Spin-orbital separation at $2 \leq n_d < 3$ : QPP structure

Next we study the qualitative change in the structure of the low-energy quasi-particle peak due to SOS with filling in more detail. In Fig. 15 (b,c,d) we plotted  $A(\omega)$  with focus on the QPP, and in Fig. 15 (e,f)  $\text{Im}\Sigma(\omega)$  for  $U = 5$ ,  $J = 1$  and various fillings,  $1 \leq n_d < 3$ .

In Fig. 15 (b), for  $n_d > 2$ ,  $A(\omega)$  is shown on a linear frequency scale and we marked the multiplet excitations of Sec. 2.6.1 and Sec. 2.6.2 [with the excitation energies adapted to  $\mu(n_d)$ ], as some of these (diamonds



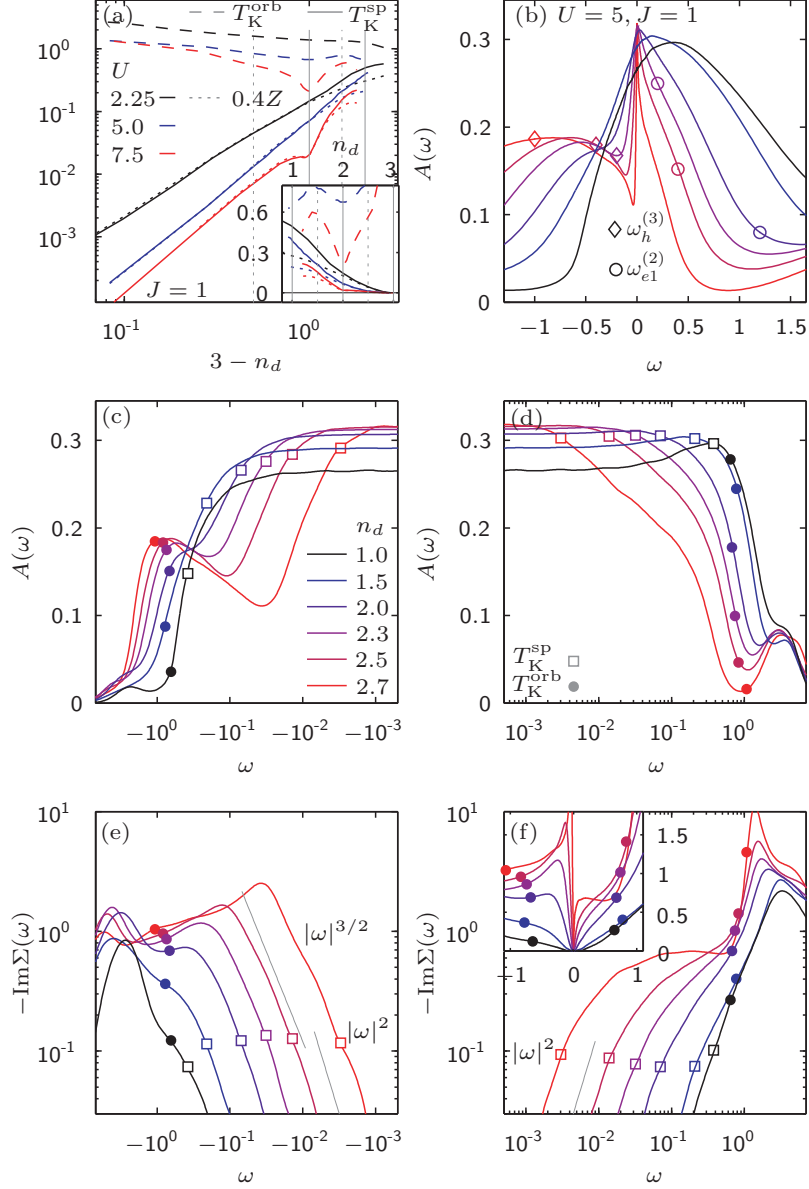


Figure 15: (a) The orbital and spin Kondo scales,  $T_K^{\text{orb}}$  (dashed) and  $T_K^{\text{sp}}$  (solid), on a log-log plot versus the distance to half-filling,  $3 - n_d$ , reveal the filling-dependence of SOS. The low QP weight  $Z$  (dotted curves) essentially follows the behavior of  $T_K^{\text{sp}}$  for  $2 \leq n_d < 3$ , and is thus determined by SOS. The inset shows the same data plotted versus  $n_d$  on a linear scale. (b-d) The local spectral function  $A(\omega)$  for  $U = 5, J = 1$  and various choices of  $n_d$ , shown on (b) linear and (c,d) logarithmic frequency scales for (c) negative and (d) positive frequencies. The symbols in (b) indicate atomic multiplet excitations at given  $n_d$  [for  $n_d = 2$ , see Eqs. (3); for  $n_d = 3$ , see (5) for details and an assignment of the markers; for  $2 < n_d < 3$ , the excitation energies are adapted to  $\mu(n_d)$ ]. For  $n_d \rightarrow 3$ , the  $\omega_h^{(3)}$  excitations (diamonds) gain weight and replace the SOS shoulder in  $A(\omega)$ , which is clearly present as a pure QP-like feature at  $n_d = 2$ . (e,f) The imaginary part of the self-energy,  $\text{Im}\Sigma(\omega)$ , plotted versus (e) negative and (f) positive frequencies. Solid grey guide-to-the-eye lines indicate  $|\omega|^2$  FL power-law behavior and apparent  $|\omega|^{3/2}$  behavior at  $\omega < 0$ . The latter fractional power-law presumably originates just from a cross-over behavior.

and circles) are rather low in energy and therefore might influence the shape of the QPP. Complementary to this, in Fig. 15 (c,d),  $A(\omega)$  [and in Fig. 15 (e,f)  $\text{Im}\Sigma(\omega)$ ] is shown on a logarithmic frequency scale and  $T_K^{\text{orb}}$  and  $T_K^{\text{sp}}$  are marked by open squares and filled circles, respectively [see legend in (d)]. Clearly, with increasing  $n_d$ , the SOS regime opens up: while there is no substructure in the QPP in  $A(\omega)$  for  $n_d \lesssim 1.5$  [black and blue curve in Fig. 15 (b,c,d)], a pronounced shoulder develops with increasing  $n_d \gtrsim 2$  for  $\omega < 0$  and a kink for  $\omega > 0$ . Accordingly, a shoulder (kink) emerges in  $\text{Im}\Sigma(\omega)$  for  $n_d > 1.5$  ( $\omega > 0$ ) which develops to a pronounced bump (plateau) for  $n_d > 2.5$  [see Fig. 15 (e,f)]. In a sense, the behavior of the SOS features with increasing  $1 < n_d < 3$  seems reminiscent of their behavior with increasing  $J$ . We note however that the character of the shoulder in  $A(\omega)$  changes for  $n_d$  well beyond 2: the shoulder gradually transforms into a Hubbard side band at the atomic hole excitation  $\omega_h^{(3)}$  for  $\omega < 0$  [diamonds in magenta and red curve in Fig. 15 (b); see also inset of Fig. 14]. In contrast, the QPP substructure narrows significantly, e.g. for  $\omega > 0$ , giving rise to a single albeit still strongly asymmetric Kondo peak at  $n_d = 2.7$ . A true QP-like shoulder only occurs for fillings  $n_d \lesssim 2.5$ , which we have checked in pure impurity AHM calculations, where the Kondo scales can be tuned to lower values and QP-like and atomic-like features are well separated.

### 5.5. Spin-orbital separation at $2 \leq n_d < 3$ : NRG flow diagrams

The nature of SOS is best revealed by the RG flows accessible to NRG via finite-size level spectra, aka. energy flow diagrams [see Fig. 16(a-c)]. Technically, they show how the lowest-lying rescaled eigenlevels of a length- $l$  Wilson chain [92, 93] evolve with  $l$ , where “rescaled” means given in units of  $\omega_l \propto \Lambda^{-l/2}$  (in the convention of Ref. [35], where  $\Lambda > 1$  is the NRG discretization parameter; see supplement of Ref. [33]). Conceptually, these levels represent the finite-size spectrum of the impurity+bath put in a spherical box of radius  $R_l \propto \Lambda^{l/2}$ , centered on the impurity [92, 94]: as  $l$  increases, the finite-size level spacing  $\omega_l \propto 1/R_l$  decreases exponentially. The corresponding flow of the finite-size spectrum is stationary ( $l$ -independent) while  $\omega_l$  lies within an energy regime governed by one of the fixed points, but changes when  $\omega_l$  traverses a crossover between two fixed points. As the rescaled ground state energy of a Wilson chain differs for even and odd numbers  $l$  of sites due to fermionic parity, the RG flow of the system is separated into an “even” and “odd” NRG flow diagram, both reflecting the same physics of the system. In Fig. 16(a-c), we purely concentrate on the even flow, since this permits the energetically favored global (Kondo) singlet ground state as  $l \rightarrow \infty$ . We fully exploited the symmetries  $U(1)_{\text{ch}} \times \text{SU}(2)_{\text{sp}} \times \text{SU}(3)_{\text{orb}}$  of the 3HHM in our NRG. Hence each line represents a multiplet and the color of each line specifies a well-defined symmetry sector  $(Q, S, q_1 q_2)$ , where the total charge  $Q$  is measured relative to half-filling,  $S$  is the total  $\text{SU}(2)$  spin multiplet sector, and  $q \equiv (q_1 q_2)$  is the  $\text{SU}(3)$  orbital label.

The multiplets with significant spin or orbital character behave qualitatively differently in the flow diagrams in Figs. 16(a-c) at finite  $J$  at the crossover scales  $T_K^{\text{sp}}$  and  $T_K^{\text{orb}}$  (vertical dashed lines). The energy range in between defines the SOS regime. We emphasize that *the SOS regime is an entirely new intermediate phase, which is absent for  $J = 0$  [see inset in Fig. 16(a)], and opens up right at the Kondo scale in the NRG flow diagram when turning on  $J$ , while the energy flow at large energies and the FL fixed point towards  $\omega_l \rightarrow 0$  remains exactly the same.* At  $n_d = 2$ , the spacing between  $T_K^{\text{orb}}$  and  $T_K^{\text{sp}}$ , though, only spans about an order of magnitude which is too small for the level flow to display a stationary intermediate fixed point.

Above  $T_K^{\text{orb}}$  the spectra correspond to the high energy physics of the Hubbard bands. Below  $T_K^{\text{sp}}$  the excitation spectra reach a FL-fixed point with qualitatively identical multiplet eigenlevel structures for all values of  $n_d$ ,  $U$ , and  $J$ : they can be interpreted in terms of non-interacting single-particle excitations [see also the  $|\omega|^1$ -scaling of  $\chi''_{\text{orb}}$  and  $\chi''_{\text{sp}}$  in Fig. 16(d)].

We now focus on Fig. 16(a) for  $n_d = 2$ ,  $U = 5$  and sizeable  $J = 1$  (similar to Fig. 3(g) in Ref. [33]). As  $\omega_l$  drops below  $T_K^{\text{orb}}$ , orbital screening sets in, favoring orbital singlets  $q = (00)$  [black and orange curves], hence other multiplets rise in energy. For the same charge  $Q$ , large-spin multiplets lie lower in energy (green curve lies below red one for  $Q = -2$ , and orange below bright blue for  $Q = -3$ ). As  $\omega_l$  drops below  $T_K^{\text{sp}}$ , spin screening sets in, favoring spin singlets and pushing up multiplets with  $S \neq 0$ . Now, multiplets with same particle number but different spins become degenerate (compare again green and red curves for  $Q = -2$ , and orange and bright blue curves for  $Q = -3$ ).

Interestingly, with increasing  $n_d$ , where the spin-orbital regime becomes wider, a new flow behavior slowly emerges at energies entering from (just above)  $T_K^{\text{orb}}$ : the multiplet with large spin  $S = 3/2$  and singlet

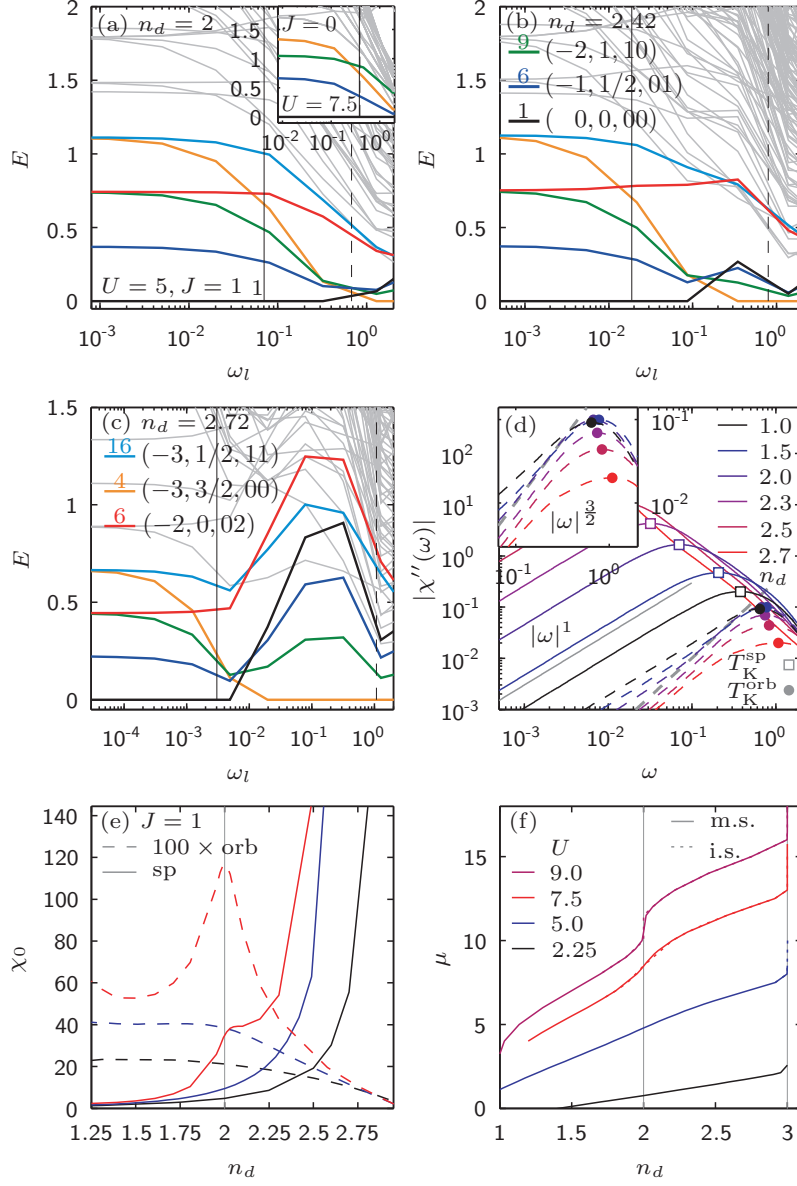


Figure 16: (a-c) Even NRG flow diagrams for different fillings, (a)  $n_d = 2$ , (b)  $n_d = 2.42$ , and (c)  $n_d = 2.7$ . The data represents rescaled energies of the lowest-lying eigenmultiplets of a Wilson chain of length  $l$  plotted versus the characteristic level spacing  $\omega_l \propto \Lambda^{-l/2}$  (see text). NRG parameters:  $\Lambda = 4$ ,  $E_{\text{trunc}} = 9$ , thus keeping up to  $D^* \lesssim 5,000$   $U(1)_{\text{charge}} \times \text{SU}(2)_{\text{sp}} \times \text{SU}(3)_{\text{orb}}$  multiplets (corresponding to about  $D = 155,000$  states) [35, 36]. The color specifies the symmetry sectors ( $Q, S, q_1 q_2$ ) (see text) as given in the legend. Numbers above lines in the legend give multiplet degeneracies. Solid (dashed) vertical lines mark the spin (orbital) Kondo scale,  $T_K^{\text{sp}}$  ( $T_K^{\text{orb}}$ ), respectively, where the range  $T_K^{\text{sp}} < |\omega| < T_K^{\text{orb}}$  represents the SOS regime. The inset of (a) shows, for comparison, the NRG flow for  $J = 0$  at  $U = 7.5$ . (d) The imaginary parts of the dynamical impurity orbital and spin susceptibilities,  $|\chi''_{\text{orb}}(\omega)|$  (dashed) and  $|\chi''_{\text{sp}}(\omega)|$  (solid) for  $U = 5$ ,  $J = 1$  and various choices of  $n_d$ .  $T_K^{\text{orb}}$  (filled circles) and  $T_K^{\text{sp}}$  (open squares) are defined from the maxima of  $\chi''_{\text{orb}}(\omega)$  and  $\chi''_{\text{sp}}(\omega)$ , respectively.  $\chi''_{\text{orb}}(\omega)$  follows an apparent  $|\omega|^{3/2}$  power law in the SOS regime (dashed grey guide-to-the-eye line) for fillings  $2 \lesssim n_d \lesssim 2.5$ , which is likely just a cross-over behavior as seen from the flows in (a,b). Below  $T_K^{\text{sp}}$ , the  $|\omega|^1$  FL power-law behavior sets in, indicated by a solid grey guide-to-the-eye line. The inset is a zoom of  $\chi''_{\text{orb}}(\omega)$ , revealing different “slopes” of  $\chi''_{\text{orb}}(\omega)$  in the SOS regime for different  $n_d$ . (e) The static local orbital and spin susceptibilities,  $\chi_0^{\text{orb}}$  (dashed) and  $\chi_0^{\text{sp}}$  (solid) are plotted as a function of  $n_d$  for three different values of  $U$  and  $J = 1$ . (f) The chemical potentials,  $\mu$ , are plotted as functions of the filling  $n_d$ , for  $J = 1$  and various values of  $U$  to study the behavior of the electronic compressibility  $\kappa_{\text{el}}$ .

orbital character  $q = (00)$  [orange curve Figs. 16(a-c)], which is still outside the SOS regime at  $n_d = 2$  [Fig. 16(a)], moves into the SOS regime at  $n_d = 2.42$  [Fig. 16(b)], and takes over the ‘SOS regime’ at  $n_d = 2.72$  [Fig. 16(c)]. At the same time, the  $T_K^{\text{orb}}$  moved upward and merges with the bare atomic energy scales. At  $T_K^{\text{sp}}$ , finally, a FL develops: the large spin  $S = 3/2$  is screened and moves upward, crossing multiple lines. The new ground state at energies below  $T_K^{\text{sp}}$  is the Kondo spin singlet (black line).

Note that the crossing of the large spin state (orange line) starts just above  $T_K^{\text{orb}}$  at  $n_d = 2$ , and has moved all the way down to  $T_K^{\text{sp}}$  at  $n_d = 2.72$ . In particular, we also emphasize that the shoulder in  $A(\omega)$  for  $n_d = 2$  in Fig. 15(c) emerges precisely around this crossing region. Therefore this qualitative change in the energy flow diagram is responsible that *the intermediate SOS regime strongly changes its character as the filling is increased towards  $n_d = 3$* . At  $n_d = 3$  the SOS becomes trivial in the sense that the orbital blocking is immediately present due to the given filling.

Importantly, the structure of the flow below the crossing region, i.e the transition behavior with decreasing  $\omega_l$  from the NFL into the FL fixed point is the same for all fillings  $2 \leq n_d < 3$ . It is therefore natural to assume that also in the SOS regime at  $n_d = 2$ , the physics is governed by an underlying NFL fixed point (i.e. a fixed point that would show up for a larger SOS region as observed in a new analysis [90] of the Kondo limit of the 3HHM), which also enforces the reversion of the lowest few multiplets compared to the FL fixed point and has a  $S = 3/2$  and  $(q_1 q_2) = (00)$  multiplet as ground state.

From the NRG flow analysis we deduce the following generic screening mechanism of SOS, which is visualized in Fig. 13(a) for  $n_d = 2$ .

*SOS is a two-stage screening process. First the orbital degrees of freedom are quenched below the orbital Kondo scale,  $T_K^{\text{orb}}$ .* In a Kondo-screening language, described in the following for  $n_d = 2$ , we have  $S = 1$  in the spin sector, while in the orbital sector, we have the fundamental representation  $q = (10)$  with dimension 3 [green lines in Figs. 16(a-c)], coupled to the 3 channels, leading to full orbital screening. As a result of this screening process *the impurity binds one electron from the bath to form an orbital singlet*. This electron has a spin  $1/2$ , which combines with the local spin 1 – due to ferromagnetic Hund’s coupling – to a spin  $3/2$ . *Then, at a lower spin Kondo scale,  $T_K^{\text{sp}}$ , this effective  $3/2$  spin is fully screened by the three bath channels of the 3HHM.* The formation of the orbital singlet causes the orbital susceptibility to reach a maximum. The resulting free spin enhances the spin susceptibility as the frequency decreases [see Fig. 9(a), Fig. 10(a) and also Fig. 16(d)]. Since a bath electron with a specific orbital degree of freedom is included in the orbital screening process, *spin and orbital degrees of freedom are still coupled, leading to a highly intertwined NFL in the SOS regime at  $n_d = 2$* . The same screening process occurs, in principle, for  $2 \leq n_d < 3$  as well, but the details vary with filling. For  $n_d$  approaching 3, the  $3/2$  spin is increasingly composed purely from the impurity spin, which facilitates the formation of the orbital singlet [ $T_K^{\text{orb}}$  grows in Fig. 15(a)], but is harder to be screened [ $T_K^{\text{sp}}$  decreases in Fig. 15(a)]. Thus the contribution of the bath electron in the screening process becomes less important, and the dynamics of the spin and orbital degrees of freedom get more and more decoupled. For  $n_d = 3$ , the orbital singlet is directly and locally formed from the impurity  $3/2$  spin without any involvement from bath degrees of freedom. Accordingly, in a weak coupling analysis [31] of the 3HHM, it is emphasized that the spin Kondo scale depends *explicitly* on the representations of the spin and the orbital isospin, which is unusual and only occurs for complex Kondo models in which spins and orbitals are coupled.

### 5.6. Spin-orbital separation at $2 \leq n_d < 3$ : susceptibilities

In Fig. 16(d), we analyze the behavior of the imaginary parts of the dynamical impurity orbital and spin susceptibilities  $\chi''_{\text{orb}}$  and  $\chi''_{\text{sp}}$ , for various fillings  $n_d$  at  $U = 5$ ,  $J = 1$ , and in Fig. 16(e) the behavior of the static local orbital and spin susceptibilities  $\chi_0 \equiv \chi(0)$  for various  $U$  at fixed  $J = 1$ . As already seen in Fig. 4(c), with increasing filling between  $1 \leq n_d < 3$  in Fig. 16(d), the maxima of  $\chi''_{\text{sp}}$  ( $T_K^{\text{sp}}$ , marked by open squares) increase in height and decrease in  $|\omega|$ , and accordingly  $\chi_0^{\text{sp}}$  [solid curves in Fig. 16(e)] grows with  $n_d$  for all values of  $U$ . For  $n_d \leq 2$ , the enhancement of  $\chi_0^{\text{sp}}$  is small and just part of an upward trend if  $U \ll U_{c2}^{(2)}$  (black and blue curves), but develops into a shoulder if  $U$  is close to the MIT at  $n_d = 2$  (red curve). For  $n_d > 2$ ,  $\chi_0^{\text{sp}}$  increases very strongly with growing  $n_d$ , almost diverging. In contrast, with increasing filling,  $n_d \leq 2$ , the maxima of  $\chi''_{\text{orb}}$  almost coincide [see filled circles in Fig. 16(d)], and  $\chi_0^{\text{orb}}$  is approximately

constant for  $U \leq 5$  [see dashed black and blue curves in Fig. 16(e)]. Only for  $U = 7.5$  much closer to  $U_{c2}^{(2)}$ ,  $\chi_0^{\text{orb}}$  first decreases and then strongly increases near the MIT at  $n_d = 2$ , indicating the presence of strong orbital fluctuations. With increasing filling,  $n_d > 2$ , the height of the maxima of  $\chi_{\text{orb}}''$  declines [see filled circles in Fig. 16(d)] and  $\chi_0^{\text{orb}}$  drops to zero when approaching  $n_d = 3$ , for all values of  $U$  [see dashed curves in Fig. 16(e)], reflecting the absence of orbital fluctuations at this point. We remark that the occurrence of a maximum in  $\chi_0^{\text{orb}}$  has also been shown in DMFT+QMC calculations [7].

In Fig. 16(d),  $|\omega|^1$ -FL-scaling is clearly observed in  $\chi_{\text{orb}}''$  and  $\chi_{\text{sp}}''$  below  $T_K^{\text{sp}}$  for all values of  $n_d$ , as indicated by the solid grey guide-to-the-eye line. Within the SOS regime  $T_K^{\text{sp}} < \omega < T_K^{\text{orb}}$ ,  $\chi_{\text{orb}}''$  shows NFL behavior (no  $|\omega|^1$ -scaling) [see also inset of Fig. 16(d)]. With increasing  $n_d > 1$  and widening SOS regime, the “slope” of  $\chi_{\text{orb}}''$  (on a log-log plot) becomes steeper than in the FL regime, i.e. an approximate power-law would have a power larger than 1. For  $2 \lesssim n_d \lesssim 2.5$ ,  $\chi_{\text{orb}}''$  reaches an approximate power of  $\frac{3}{2}$ . This, however, is presumably not a pure power law, since the SOS regime is not wide enough, i.e. the RG flows of Fig. 16(a-c) are yet far from reaching a stationary fixed point in the SOS regime. For  $n_d > 2.5$ , however, the slope is again lowered to almost 1.

*Based on these observation and the RG flows we argue that intriguing NFL behavior with relevance for Hund metals occurs mainly in the filling regime of approximately  $1.5 \lesssim n_d \lesssim 2.5$ . Only there, a complex two-stage screening process couples the dynamics of spin and orbital degrees of freedom by the formation of a large, effective Hund’s-coupling induced  $3/2$  spin including a bath spin degree of freedom. Although fully screened, the orbital degrees of freedom still “feel” the slowly fluctuating, large local moments, which is reflected in the fact that, in the SOS regime in Fig. 16(d), the “slope” of  $\chi_{\text{orb}}''$  is increased compared to FL scaling.*

To summarize, *we argue that the suppression of  $Z$  in the Hund metal regime around  $n_d \gtrsim 2$  at moderate  $U \ll U_{c2}^{(2)}$  is mainly caused by SOS, and thus by the presence of a sizeable Hund’s coupling in the system. It is not triggered by Mottness (iii), the proximity to the MIT at half-filling,  $n_d = 3$ . Of course, as also known from the MIT in the one-band Hubbard model,  $Z$  is further lowered by the proximity to the MIT at  $n_d = 3$ , but this effect is strong only close to  $n_d = 3$  and is subleading in the Hund-metal regime. Further, the physics close to  $n_d = 3$  is dominated by fully blocked orbital degrees of freedom while for Hund metals the orbital degrees of freedom play a subtle role in the nature of the NFL physics.*

We remark that our insights might be relevant to better understand the physics of iron pnictides with hole and electron doping [14, 19]. For instance, for BaFe2As2 (with a nominal  $d6$  occupation in the parent compound) correlations are enhanced upon approaching half filling with hole-doping, achieved by replacing Ba with K, and reduced upon electron doping, achieved by replacing Fe with Co [65].

### 5.7. Filling dependence of the compressibility, $\kappa_{\text{el}}$

We finish this section with a discussion of the compressibility in Fig. 16(f). We plot  $\mu$  versus  $n_d$  to access the zero-temperature behavior of the electronic compressibility,  $\kappa_{\text{el}} = \frac{\partial n_d}{\partial \mu}$ , for finite  $J = 1$  and for several values of  $U$ , varying from slightly above  $U_{c2}^{(3)}$  to slightly above  $U_{c2}^{(2)}$ . Solid (dashed) lines are the results for a mS (iS), respectively. Normally,  $\kappa_{\text{el}}$  has finite, positive values for metals and vanishes for insulators. We would like to investigate whether  $\kappa_{\text{el}}$  remains positive throughout, or becomes negative for  $n_d$  close to the MIT at  $n_d = 2$  or close to the MIT at  $n_d = 3$ . The latter scenario, a zone of Hund’s-coupling-induced negative compressibility in the  $n_d$ - $U$  phase diagram, has been observed in a slave-boson study [58] of degenerate and non-degenerate multi-band Hund models, for nonzero  $J$  and  $U \geq U_c$  at  $T = 0$ . The divergence of  $\kappa_{\text{el}}$ , when  $\kappa_{\text{el}}$  changes sign, has been assumed to be connected to the enhanced critical  $T_c$  of HTCS. However, for the 3HHM, for all parameters studied in Fig. 16(f),  $\mu$  clearly increases monotonically with  $n_d$ . Hence the slope,  $\kappa_{\text{el}}$ , is positive for all non-integer fillings, also close to the insulating phase at  $n_d = 2$  and  $n_d = 3$ , where  $n_d$  is fixed and thus incompressible for varying  $\mu$ , i.e.  $\kappa_{\text{el}} = 0$ . We summarize that, for our study, *no negative (or divergent) compressibility has been observed for the 3HHM*. We note, though, that in principle a compressibility divergence can occur very close to a MIT in certain situations [41].

## 6. Conclusion

In this work, we studied the full phase diagram of the 3HHM at zero temperature with real-frequency DMFT+NRG data. Our main goal was to reveal the origin of the bad-metallic behavior (characterized by a low quasiparticle weight  $Z$ ) in the Hund-metal regime (hatched area in Fig. 1) and to establish a global picture of SOS.

As a main result we demonstrated that, for nonzero  $J$  and for fillings  $1 < n_d < 3$ , SOS is a generic feature in the *whole* metallic (and coexistence) phase of the 3HHM, independently of  $U$ : turning on  $J$  opens up a new incoherent energy regime,  $T_K^{\text{orb}} > |\omega|, T > T_K^{\text{sp}}$ , in the system. Interestingly, for fillings around  $n_d = 2$  (i.e approximately in the regime  $1.5 \lesssim n_d \lesssim 2.5$ ) the SOS is special, as has been pointed out in Ref. [7]. There, orbital and spin degrees of freedom are *coupled* and thus behave very distinctly: orbital degrees of freedom are (mostly) quenched below  $T_K^{\text{orb}}$  and fluctuate rapidly, whereas spin degrees of freedom are unquenched, form large local moments, and fluctuate extremely slowly. Below, the strongly reduced spin Kondo scale,  $T_K^{\text{sp}}$ , both orbital *and* spin degrees of freedoms are fully screened and FL behavior sets in.

We confirm in detail that the suppression of  $T_K^{\text{sp}}$  with increasing  $J$  can be explained from a qualitative change in the underlying local multiplet spectrum, involving a reduction in the atomic ground state degeneracy.  $Z$  is explicitly shown to be proportional to  $T_K^{\text{sp}}$ , and thus small due to SOS.

In agreement with the analysis in the Kondo regime of the 3HHM [31], we argue that SOS is a non-trivial two-stage screening process, in which orbital and spin degrees of freedom are explicitly coupled: below  $T_K^{\text{orb}}$ , the orbital degrees of freedom form an orbital singlet through the formation of a large, effective, Hund's-coupling induced  $3/2$  spin – *including* a bath spin degree of freedom; and below  $T_K^{\text{sp}}$ , the latter is fully screened by the three bath channels of the 3HHM.

In the real-frequency spectral function, SOS results in a "two-tier" QPP peak with a narrow needle (width  $\propto T_K^{\text{sp}}$ ) on top of a wide base (width  $\propto T_K^{\text{orb}}$ ).

Based on the SOS analysis we conclude, as major result of this work, that in the Hund-metal regime, at sizeable  $J$ , moderate  $U$  well below  $U_c^{(2)}$  and fillings close to  $n_d = 2$ , i.e far from any MIT, Hundness, i.e scenario (i), is the origin of bad-metallic behavior and governs the physics of Hund metals. This constitutes a new route towards strong correlations very distinct from Mottness: while in the latter case charges are localized in close proximity to an MIT, Hundness implies the localization of spins but not the localization of charges. For Hund-correlated metals,  $T_K^{\text{orb}}$  is comparable in magnitude to bare atomic energy scales of the system, while  $T_K^{\text{sp}}$  (and thus  $Z$ ) is strongly reduced, leading to low FL coherence scales and to a broad incoherent SOS regime. Hundness is thus physics governed by the QP needle being narrow, while the QP base remains wide. Importantly, this regime is characterized by the non-trivial interplay of orbital and spin degrees of freedom, induced by the special two-stage SOS screening process, which essentially dominates the normal-state incoherence of Hund metals. We remark that Mottness of type (ii) does affect the SOS when the distance to the MIT is decreased at fixed  $n_d = 2$ , by further lowering  $T_K^{\text{orb}}$  and  $T_K^{\text{sp}}$ , while their ratio remains constant. Whereas  $T_K^{\text{orb}}$  governs the Mott transition (which requires the full QPP to disappear),  $T_K^{\text{sp}}$ , being proportional to  $Z$ , governs the strength of correlations.

Mott-correlated metals, close to the MIT at  $n_d \approx 2$ , are dominated by Mottness, while the SOS regime is strongly downscaled and becomes negligible.

Close to the MIT at  $n_d = 3$ , the SOS regime widens up because the orbital degrees of freedom get blocked by the formation of a  $3/2$  impurity spin, but its nature changes: the orbital and spin dynamics get decoupled. Thus, Mottness of type (iii) does not mediate the low  $Z$  in the Hund-metal regime.

In sum, our DMFT+NRG results corroborate the physical picture of Hund metals established in Refs. [6, 7, 31, 47] and enabled the quantitative analysis of the real-frequency properties of their unusual incoherent SOS regime. We showed that the spin-freezing phenomenon [51] and the Janus-faced influence of Hund's rule coupling can be consistently explained in the framework of SOS. We also explicitly demonstrated that no Hund's-coupling-induced FL instabilities (negative compressibilities) [58] occurs in our study of the 3HHM phase diagram.

## Appendix A. Methods

We treat the 3HHM of Eq. (1) with single-site DMFT and use full-density-matrix (fdm)NRG [34] as real-frequency impurity solver.

### Appendix A.1. Single-site Dynamical Mean-Field Theory

Single-site DMFT is a widely-used non perturbative many-body approach to strongly correlated systems [82]. Its basic idea is to approximate the full non local self-energy of the correlated lattice model by the purely local, but still frequency-dependent self-energy,  $\Sigma(\omega)$ , of the corresponding self-consistently determined quantum impurity model. In our case, we iteratively map the lattice 3HHM of Eq. (1) onto a three-band Anderson-Hund model (AHM) of the form

$$\hat{H}_{\text{AHM}} = \hat{H}_{\text{imp}} + \hat{H}_{\text{bath+hyb}}, \quad (\text{A.1a})$$

$$\hat{H}_{\text{imp}} = \varepsilon_d \hat{N} + \hat{H}_{\text{int}}[\hat{d}_\nu^\dagger] \quad (\text{A.1b})$$

with the same local interaction term,  $\hat{H}_{\text{int}}$ , as in Eq. (1b). Within this mapping process, the hybridization function  $\Gamma(\varepsilon) = \pi \sum_k |V_k|^2 \delta(\varepsilon - \varepsilon_k)$  is determined self-consistently and eventually fully characterizes the interplay of the impurity and the non-interacting three-band spinful bath,

$$H_{\text{bath+hyb}} = \sum_{k\nu} \left( \varepsilon_k c_{k\nu}^\dagger \hat{c}_{k\nu} + V_k [\hat{d}_\nu^\dagger \hat{c}_{k\nu} + \hat{c}_{k\nu}^\dagger \hat{d}_\nu] \right). \quad (\text{A.2})$$

Here  $d_\nu^\dagger$  creates a local (“impurity”) electron of flavor  $\nu$  with energy  $\varepsilon_d = -\mu$ . The total spin operator  $\hat{\mathbf{S}}$  (and  $\hat{\mathbf{S}}_i$ , respectively) are lattice sums over  $(\hat{n}_i - N_c)$ , i.e. charge relative to half-filling. The average local site occupation number  $n_d \equiv \langle \hat{n}_i \rangle$  is a measure of the lattice filling per site.

The lattice dynamics is fully captured by the local retarded lattice Green’s function,  $G_{\text{latt}}(\omega)$ , which is – after the self-consistent mapping – equal to the retarded impurity Green’s function,  $G_{\text{imp}}(\omega) = \langle \hat{d}_\nu | \hat{d}_\nu^\dagger \rangle_\omega$ , imposing the self-consistency condition:  $G_{\text{latt}}(\omega) = G_{\text{imp}}(\omega) \equiv G(\omega)$ . Note that we consistently drop the flavor index  $\nu$  for all correlation functions as they are identical by symmetry for all spins and orbitals.

In this work, we study Hund metals only on the Bethe lattice, i.e. we use the semi-elliptic density of states that occurs in this limit of infinite lattice coordination and neglect realistic band-structure effects, to investigate the pure correlation effects of multi-orbital Mott and Hund physics. The self-consistency condition can then be simplified to,

$$\Gamma(\omega) = -t^2 \text{Im} G(\omega). \quad (\text{A.3})$$

The approximation of a purely local self-energy in single-site DMFT is strictly valid only in the artificial limit of infinite lattice coordination number. However, if interactions act only locally in a lattice system with finite coordination number, as in the case of Hund’s rule coupling which is adopted from local atomic physics, single-site DMFT is assumed to be an appropriate method to reproduce the correct physics. This assumption is supported by recent cluster-DMFT calculations for Hund metals [95]. Further, single-site DMFT is in general able to capture basic strong correlations effects of finite dimensional systems (like the MIT) due to its non-perturbative character: through the energy-dependence of the local self-energy both the itinerant and localized nature of electrons, and thus both weak and strong correlations, can be handled on equal footing.

This is considered to be of utmost importance for the description of iron-based HTSCs and other Hund metals, as very likely, neither pure atomic physics nor pure band theory does apply. In these bad-metallic multi-orbital systems, the existence and interplay of itinerant, but strongly renormalized electrons *and* strongly, but not fully localized large spin moments have to be analyzed without any method-induced bias – even far from any Mott insulating state [19, 46, 49, 96].

### Appendix A.2. Numerical Renormalization Group

In each step of the DMFT self-consistency loop, we solve the quantum-impurity problem Eq. (A.3) with `fdmNRG`, a powerful impurity solver that offers numerically exact real-frequency spectral resolution at arbitrarily low energies and temperatures for multi-band impurity models [34, 36, 97] and lattice models in the DMFT context [33, 85, 98].

NRG [36, 92, 93] has a longstanding and successful history as the standard tool to deal with impurity models. Its basic idea goes back to Wilson’s fundamental insight [92] to introduce a logarithmic discretization of the noninteracting bath Eq. (A.2) of an impurity model Hamiltonian and map the discretized bath onto a 1D semi-infinite, tight-binding chain, a “Wilson chain”, with the interacting impurity site coupled to one end. The hopping matrix elements then decay exponentially down the Wilson chain and introduce an energy-scale separation that allows for an iterative RG solution scheme based on successive diagonalization and truncation of high-energy states. The size of the Fock state space can thus be kept fixed with increasing chain length while still obtaining an exponentially increased resolution of the low-energy part of the spectrum. The resolution at high energies is, however, more coarse-grained. Nevertheless, our approach captures all essential high-energy features [34].

In recent years, significant progress has been made in developing NRG into an efficient high-quality multi-band DMFT impurity solver [33, 85, 97, 98]. Our `fdmNRG` solver is implemented based on the `QSpace` tensor library [36] applied to matrix product states (MPS) [35, 99] as generated in NRG. In the `QSpace` tensor library, Abelian and non-Abelian symmetries are implemented on a generic level: the state space is organized into symmetry multiplets, and tensors “factorize” into two parts, acting in the reduced multiplet space and the Clebsch Gordon coefficient space, respectively. Diagonalization of the NRG Hamiltonian at each iteration step can then be done in multiplet space rather than state space, significantly reducing the matrix sizes and hence computational cost. NRG calculations with three and even more *degenerate* bands [36, 90, 97] became feasible, also in the DMFT context [33, 98]. For solving our 3HHM in Eq. (1), we explicitly exploit its  $U(1)_{\text{ch}} \times SU(2)_{\text{sp}} \times SU(3)_{\text{orb}}$  symmetries. We note that also models with three (or even more) *non-degenerate* bands are within the reach of NRG, using `iNRG`, the “interleaved” version of NRG [97]. It is thus also possible to study orbital differentiation with DMFT+`iNRG`, as will be demonstrated elsewhere [67].

The `fdmNRG` solver is established on a complete basis set [100, 101], constructed from the discarded states of all NRG iterations. Spectral functions for the discretized model are given from the Lehmann representation as a sum of poles, and can be calculated accurately directly on the real-frequency axis in sum-rule conserving fashion [102] at zero or arbitrary finite temperature. Continuous spectra are obtained by broadening the discrete data with a standard log-gaussian Kernel of frequency-dependent width [34, 93].

To improve the resolution of spectral data, we “z-average” over the results obtained from several, differing NRG runs, for which the logarithmic discretization of the bath has been uniformly shifted with respect to each other [87, 103]. We note that, within DMFT, the NRG discretization scheme (originally developed for the flat hybridization function  $\Gamma(\varepsilon) = \Gamma\Theta(D - |\varepsilon|)$  of quantum impurity models with half-bandwidth  $D=1$ ) has to be adapted to optimally discretize the frequency-dependent hybridization functions that emerge in every step of the self-consistency loop. Here, we use a numerically stable implementation [104] of the scheme in Refs. [87, 105] to accurately represent the nontrivial continuous baths in terms of discrete bath states.

Within the DMFT+NRG approach, the resolution of spectral data can be further improved by applying the so-called self-energy trick [106]. In every step of the iterative mapping, the self-energy is calculated as the ratio of two NRG correlation functions [106]

$$\Sigma(\omega) = \frac{F(\omega)}{G(\omega)}, \quad (\text{A.4})$$

where  $F(\omega) = \langle [\hat{d}_\nu, \hat{H}_{\text{int}}[\hat{d}_\nu^\dagger]] \parallel \hat{d}_\nu^\dagger \rangle_\omega$ . The imaginary parts of both correlators,  $F(\omega)$  and  $G(\omega)$ , are `fdmNRG` spectral functions while the real-parts are obtained from their Kramers-Kronig transformations, respectively. Instead of using the raw NRG result  $G(\omega)$  for the self-consistency condition Eq. (A.3), an improved version of the (lattice) Green’s function is calculated via the simple analytic form

$$G_{\text{impr}}(\omega) = \frac{1}{2t^2} \left( \xi - \sqrt{\xi^2 - 4t^2} \right) \quad (\text{A.5})$$



with  $\xi = \omega + \mu - \Sigma(\omega)$ , valid only for the Bethe lattice. In this work we only refer to the improved Green's function and therefore drop the index from now on:  $G(\omega) \equiv G_{\text{impr}}(\omega)$ .

From the improved Green's function, we have direct access to the real-frequency spectral function, also called local density of states:

$$A(\omega) = -\frac{1}{\pi} \text{Im} G^R(\omega). \quad (\text{A.6})$$

All computational parameters and further details of our DMFT+NRG calculations are listed in the Supplementary material of Ref. [33].

In Ref. [33] we have already demonstrated that DMFT+NRG is perfectly suited for the investigation of the 3HHM. The exponentially enhanced resolution around the Fermi level resolves spectral features down to the lowest relevant energy scale of the system. In contrast to QMC solvers, the NRG solver thus reaches the strongly reduced FL ground state in a  $T = 0^+$  simulation of the model. At the same time atomic-like features which constitute the Hubbard side bands are well reproduced, e.g. as shown in Sec. 4 and Sec. 5. The access to real-frequency quantities helps us to understand the nature of the incoherent regime together with NRG eigenlevel renormalization group (RG) flow diagrams that reveal the relevant physics at all energy scales.

## References

- [1] Y. Kamihara, H. Hiramatsu, M. Hirano, R. Kawamura, H. Yanagi, T. Kamiya, H. Hosono, Iron-Based Layered Superconductor: LaOFeP, *Journal of the American Chemical Society* 128 (31) (2006) 10012–10013, URL <https://doi.org/10.1021/ja063355c>.
- [2] Y. Kamihara, T. Watanabe, M. Hirano, H. Hosono, Iron-Based Layered Superconductor La[O<sub>1-x</sub>F<sub>x</sub>]FeAs ( $x = 0.05 - 0.12$ ) with  $T_c = 26\text{K}$ , *Journal of the American Chemical Society* 130 (11) (2008) 3296–3297, URL <https://doi.org/10.1021/ja800073m>.
- [3] Z.-A. Ren, G.-C. Che, X.-L. Dong, J. Yang, W. Lu, W. Yi, X.-L. Shen, Z.-C. Li, L.-L. Sun, F. Zhou, Z.-X. Zhao, Superconductivity and phase diagram in iron-based arsenic-oxides ReFeAsO<sub>1- $\delta$</sub>  (Re = rare-earth metal) without fluorine doping, *EPL (Europhysics Letters)* 83 (1) (2008) 17002, URL <http://stacks.iop.org/0295-5075/83/i=1/a=17002>.
- [4] Z. A. Ren, J. Yang, W. Lu, W. Yi, G. C. Che, X. L. Dong, L. L. Sun, Z. X. Zhao, Superconductivity at 52 K in iron based F doped layered quaternary compound Pr[O<sub>1-x</sub>F<sub>x</sub>]FeAs, *Materials Research Innovations* 12 (3) (2008) 105–106, URL <https://doi.org/10.1179/143307508X333686>.
- [5] G. Wu, Y. L. Xie, H. Chen, M. Zhong, R. H. Liu, B. C. Shi, Q. J. Li, X. F. Wang, T. Wu, Y. J. Yan, J. J. Ying, X. H. Chen, Superconductivity at 56K in samarium-doped SrFeAsF, *Journal of Physics: Condensed Matter* 21 (14) (2009) 142203, URL <http://stacks.iop.org/0953-8984/21/i=14/a=142203>.
- [6] K. Haule, G. Kotliar, Coherence-incoherence crossover in the normal state of iron oxypnictides and importance of Hund's rule coupling, *New J. Phys.* 11 (2009) 025021, URL <http://iopscience.iop.org/1367-2630/11/2/025021>.
- [7] Z. P. Yin, K. Haule, G. Kotliar, Fractional power-law behavior and its origin in iron-chalcogenide and ruthenate superconductors: Insights from first-principles calculations, *Phys. Rev. B* 86 (2012) 195141, URL <http://link.aps.org/doi/10.1103/PhysRevB.86.195141>.
- [8] M. Yi, D. H. Lu, R. Yu, S. C. Riggs, J.-H. Chu, B. Lv, Z. K. Liu, M. Lu, Y.-T. Cui, M. Hashimoto, S.-K. Mo, Z. Hussain, C. W. Chu, I. R. Fisher, Q. Si, Z.-X. Shen, Observation of Temperature-Induced Crossover to an Orbital-Selective Mott Phase in A<sub>x</sub>Fe<sub>2-y</sub>Se<sub>2</sub> (A=K, Rb) Superconductors, *Phys. Rev. Lett.* 110 (2013) 067003, URL <https://link.aps.org/doi/10.1103/PhysRevLett.110.067003>.
- [9] F. Hardy, A. E. Böhmer, D. Aoki, P. Burger, T. Wolf, P. Schweiss, R. Heid, P. Adelmann, Y. X. Yao, G. Kotliar, J. Schmalian, C. Meingast, Evidence of Strong Correlations and Coherence-Incoherence Crossover in the Iron Pnictide Superconductor KFe<sub>2</sub>As<sub>2</sub>, *Phys. Rev. Lett.* 111 (2013) 027002, URL <https://link.aps.org/doi/10.1103/PhysRevLett.111.027002>.
- [10] K. Haule, J. H. Shim, G. Kotliar, Correlated Electronic Structure of LaO<sub>1-x</sub>F<sub>x</sub>FeAs, *Phys. Rev. Lett.* 100 (2008) 226402, URL <https://link.aps.org/doi/10.1103/PhysRevLett.100.226402>.
- [11] A. Liebsch, H. Ishida, Correlation-induced spin freezing transition in FeSe: A dynamical mean field study, *Phys. Rev. B* 82 (2010) 155106, URL <https://link.aps.org/doi/10.1103/PhysRevB.82.155106>.
- [12] H. Ishida, A. Liebsch, Fermi-liquid, non-Fermi-liquid, and Mott phases in iron pnictides and cuprates, *Phys. Rev. B* 81 (2010) 054513, URL <https://link.aps.org/doi/10.1103/PhysRevB.81.054513>.
- [13] M. Aichhorn, S. Biermann, T. Miyake, A. Georges, M. Imada, Theoretical evidence for strong correlations and incoherent metallic state in FeSe, *Phys. Rev. B* 82 (2010) 064504, URL <https://link.aps.org/doi/10.1103/PhysRevB.82.064504>.
- [14] P. Werner, M. Casula, T. Miyake, F. Aryasetiawan, A. J. Millis, S. Biermann, Satellites and large doping and temperature dependence of electronic properties in hole-doped BaFe<sub>2</sub>As<sub>2</sub>, *Nature Physics* 8 (2012) 331 – 337, URL <http://dx.doi.org/10.1038/nphys2250>.
- [15] A. A. Schafgans, S. J. Moon, B. C. Pursley, A. D. LaForge, M. M. Qazilbash, A. S. Sefat, D. Mandrus, K. Haule, G. Kotliar, D. N. Basov, Electronic Correlations and Unconventional Spectral Weight Transfer in the High-Temperature

- Pnictide  $\text{BaFe}_{2-x}\text{Co}_x\text{As}_2$  Superconductor Using Infrared Spectroscopy, Phys. Rev. Lett. 108 (2012) 147002, URL <https://link.aps.org/doi/10.1103/PhysRevLett.108.147002>.
- [16] J. Fink, A. Charnukha, E. D. L. Rienks, Z. H. Liu, S. Thirupathiah, I. Avigo, F. Roth, H. S. Jeevan, P. Gegenwart, M. Roslova, I. Morozov, S. Wurmehl, U. Bovensiepen, S. Borisenko, M. Vojta, B. Büchner, Non-Fermi-liquid scattering rates and anomalous band dispersion in ferropnictides, Phys. Rev. B 92 (2015) 201106, URL <https://link.aps.org/doi/10.1103/PhysRevB.92.201106>.
- [17] M. Yi, Z.-K. Liu, Y. Zhang, R. Yu, J. X. Zhu, J. J. Lee, R. G. Moore, F. T. Schmitt, W. Li, S. C. Riggs, J. H. Chu, B. Lv, J. Hu, M. Hashimoto, S. K. Mo, Z. Hussain, Z. Q. Mao, C. W. Chu, I. R. Fisher, Q. Si, Z. X. Shen, D. H. Lu, Observation of universal strong orbital-dependent correlation effects in iron chalcogenides, Nature Communications 6 (2015) 7777, URL <http://dx.doi.org/10.1038/ncomms8777>.
- [18] H. Gretarsson, A. Lupascu, J. Kim, D. Casa, T. Gog, W. Wu, S. R. Julian, Z. J. Xu, J. S. Wen, G. D. Gu, R. H. Yuan, Z. G. Chen, N.-L. Wang, S. Khim, K. H. Kim, M. Ishikado, I. Jarrige, S. Shamoto, J.-H. Chu, I. R. Fisher, Y.-J. Kim, Revealing the dual nature of magnetism in iron pnictides and iron chalcogenides using x-ray emission spectroscopy, Phys. Rev. B 84 (2011) 100509, URL <https://link.aps.org/doi/10.1103/PhysRevB.84.100509>.
- [19] J. Pellicciari, Y. Huang, K. Ishii, C. Zhang, P. Dai, G. F. Chen, L. Xing, X. Wang, C. Jin, H. Ding, P. Werner, T. Schmitt, Magnetic moment evolution and spin freezing in doped  $\text{BaFe}_2\text{As}_2$ , Scientific Reports 7 (2017) 8003, URL <https://doi.org/10.1038/s41598-017-07286-6>.
- [20] S. Lafuerza, H. Gretarsson, F. Hardy, T. Wolf, C. Meingast, G. Giovannetti, M. Capone, A. S. Sefat, Y.-J. Kim, P. Glatzel, L. de' Medici, Evidence of Mott physics in iron pnictides from x-ray spectroscopy, Phys. Rev. B 96 (2017) 045133, URL <https://link.aps.org/doi/10.1103/PhysRevB.96.045133>.
- [21] M. M. Qazilbash, J. J. Hamlin, R. E. Baumbach, L. Zhang, D. J. Singh, M. B. Maple, D. N. Basov, Electronic correlations in the iron pnictides, Nature Physics 5 (2009) 647–650, URL <http://dx.doi.org/10.1038/nphys1343>.
- [22] T. Terashima, M. Kimata, N. Kurita, H. Satsukawa, A. Harada, K. Hazama, M. Imai, A. Sato, K. Kihou, C.-H. Lee, H. Kito, H. Eisaki, A. Iyo, T. Saito, H. Fukazawa, Y. Kohori, H. Harima, S. Uji, Fermi Surface and Mass Enhancement in  $\text{KFe}_2\text{As}_2$  from de Haas–van Alphen Effect Measurements, Journal of the Physical Society of Japan 79 (5) (2010) 053702, URL <https://doi.org/10.1143/JPSJ.79.053702>.
- [23] T. Terashima, M. Kimata, H. Satsukawa, A. Harada, K. Hazama, M. Imai, A. Sato, S. Uji, K. Kihou, C.-H. Lee, H. Kito, H. Eisaki, A. Iyo, H. Fukazawa, Y. Kohori, H. Harima, De Haas–van Alphen oscillations in  $\text{KFe}_2\text{As}_2$ , Physica C: Superconductivity and its Applications 470 (2010) S351 – S352, ISSN 0921-4534, URL <http://www.sciencedirect.com/science/article/pii/S0921453409007163>.
- [24] A. Tamai, A. Y. Ganin, E. Rozbicki, J. Bacsá, W. Meevasana, P. D. C. King, M. Caffio, R. Schaub, S. Margadonna, K. Prassides, M. J. Rosseinsky, F. Baumberger, Strong Electron Correlations in the Normal State of the Iron-Based  $\text{FeSe}_{0.42}\text{Te}_{0.58}$  Superconductor Observed by Angle-Resolved Photoemission Spectroscopy, Phys. Rev. Lett. 104 (2010) 097002, URL <https://link.aps.org/doi/10.1103/PhysRevLett.104.097002>.
- [25] A. Yamasaki, Y. Matsui, S. Imada, K. Takase, H. Azuma, T. Muro, Y. Kato, A. Higashiya, A. Sekiyama, S. Suga, M. Yabashi, K. Tamasaku, T. Ishikawa, K. Terashima, H. Kobori, A. Sugimura, N. Umeyama, H. Sato, Y. Hara, N. Miyagawa, S. I. Ikeda, Electron correlation in the FeSe superconductor studied by bulk-sensitive photoemission spectroscopy, Phys. Rev. B 82 (2010) 184511, URL <https://link.aps.org/doi/10.1103/PhysRevB.82.184511>.
- [26] S. V. Borisenko, V. B. Zabolotnyy, D. V. Evtushinsky, T. K. Kim, I. V. Morozov, A. N. Yaresko, A. A. Kordyuk, G. Behr, A. Vasiliev, R. Follath, B. Büchner, Superconductivity without Nesting in  $\text{LiFeAs}$ , Phys. Rev. Lett. 105 (2010) 067002, URL <https://link.aps.org/doi/10.1103/PhysRevLett.105.067002>.
- [27] T. Terashima, N. Kurita, M. Kimata, M. Tomita, S. Tsuchiya, M. Imai, A. Sato, K. Kihou, C.-H. Lee, H. Kito, H. Eisaki, A. Iyo, T. Saito, H. Fukazawa, Y. Kohori, H. Harima, S. Uji, Fermi surface in  $\text{KFe}_2\text{As}_2$  determined via de Haas–van Alphen oscillation measurements, Phys. Rev. B 87 (2013) 224512, URL <https://link.aps.org/doi/10.1103/PhysRevB.87.224512>.
- [28] T. Yoshida, S.-i. Ideta, I. Nishi, A. Fujimori, M. Yi, R. Moore, S.-K. Mo, D. Lu, Z.-X. Shen, Z. Hussain, K. Kihou, C. H. Lee, A. Iyo, H. Eisaki, H. Harima, Orbital character and electron correlation effects on two- and three-dimensional Fermi surfaces in  $\text{KFe}_2\text{As}_2$  revealed by angle-resolved photoemission spectroscopy, Frontiers in Physics 2 (2014) 17, URL <https://www.frontiersin.org/article/10.3389/fphy.2014.00017>.
- [29] J. Orenstein, A. J. Millis, Advances in the Physics of High-Temperature Superconductivity, Science 288 (5465) (2000) 468–474, ISSN 0036-8075, URL <http://science.sciencemag.org/content/288/5465/468>.
- [30] P. A. Lee, N. Nagaosa, X.-G. Wen, Doping a Mott insulator: Physics of high-temperature superconductivity, Rev. Mod. Phys. 78 (2006) 17–85, URL <https://link.aps.org/doi/10.1103/RevModPhys.78.17>.
- [31] C. Aron, G. Kotliar, Analytic theory of Hund's metals: A renormalization group perspective, Phys. Rev. B 91 (2015) 041110, URL <https://link.aps.org/doi/10.1103/PhysRevB.91.041110>.
- [32] L. Fanfarillo, E. Bascones, Electronic correlations in Hund metals, Phys. Rev. B 92 (2015) 075136, URL <https://link.aps.org/doi/10.1103/PhysRevB.92.075136>.
- [33] K. M. Stadler, Z. P. Yin, J. von Delft, G. Kotliar, A. Weichselbaum, Dynamical Mean-Field Theory Plus Numerical Renormalization-Group Study of Spin-Orbital Separation in a Three-Band Hund Metal, Phys. Rev. Lett. 115 (2015) 136401, URL <https://link.aps.org/doi/10.1103/PhysRevLett.115.136401>.
- [34] A. Weichselbaum, J. von Delft, Sum-Rule Conserving Spectral Functions from the Numerical Renormalization Group, Phys. Rev. Lett. 99 (7) 076402, URL <http://link.aps.org/abstract/PRL/v99/e076402>.
- [35] A. Weichselbaum, Tensor networks and the numerical renormalization group, Phys. Rev. B 86 (2012) 245124, URL <http://link.aps.org/doi/10.1103/PhysRevB.86.245124>.
- [36] A. Weichselbaum, Non-abelian symmetries in tensor networks: A quantum symmetry space approach, Annals of Physics

- 327 (2012) 2972–3047, URL <http://www.sciencedirect.com/science/article/pii/S0003491612001121>.
- [37] X. Deng, K. M. Stadler, K. Haule, A. Weichselbaum, J. von Delft, G. Kotliar, Signatures of Mottness and Hundness in archetypal correlated metals, arXiv:1708.05752 [cond-mat.str-el] URL <https://arxiv.org/abs/1708.05752v2>.
- [38] N. F. MOTT, Metal-Insulator Transition, *Rev. Mod. Phys.* 40 (1968) 677–683, URL <https://link.aps.org/doi/10.1103/RevModPhys.40.677>.
- [39] M. J. Rozenberg, G. Kotliar, H. Kajueter, G. A. Thomas, D. H. Rapkine, J. M. Honig, P. Metcalf, Optical Conductivity in Mott-Hubbard Systems, *Phys. Rev. Lett.* 75 (1995) 105–108, URL <https://link.aps.org/doi/10.1103/PhysRevLett.75.105>.
- [40] G. Kotliar, Landau theory of the Mott transition in the fully frustrated Hubbard model in infinite dimensions, *Eur. Phys. J. B* 11 (1) (1999) 27–39, URL <https://doi.org/10.1007/s100510050914>.
- [41] G. Kotliar, S. Murthy, M. J. Rozenberg, Compressibility Divergence and the Finite Temperature Mott Transition, *Phys. Rev. Lett.* 89 (2002) 046401, URL <https://link.aps.org/doi/10.1103/PhysRevLett.89.046401>.
- [42] D. B. McWhan, T. M. Rice, J. P. Remeika, Mott Transition in Cr-Doped  $V_2O_3$ , *Phys. Rev. Lett.* 23 (1969) 1384–1387, URL <https://link.aps.org/doi/10.1103/PhysRevLett.23.1384>.
- [43] D. B. McWhan, A. Menth, J. P. Remeika, W. F. Brinkman, T. M. Rice, Metal-Insulator Transitions in Pure and Doped  $V_2O_3$ , *Phys. Rev. B* 7 (1973) 1920–1931, URL <https://link.aps.org/doi/10.1103/PhysRevB.7.1920>.
- [44] D. B. McWhan, J. P. Remeika, J. P. Maita, H. Okinaka, K. Kosuge, S. Kachi, Heat Capacity of Vanadium Oxides at Low Temperature, *Phys. Rev. B* 7 (1973) 326–332, URL <https://link.aps.org/doi/10.1103/PhysRevB.7.326>.
- [45] P. Hansmann, A. Toschi, G. Sangiovanni, T. Saha-Dasgupta, S. Lupi, M. Marsi, K. Held, Mott-Hubbard transition in  $V_2O_3$  revisited, *physica status solidi (b)* 250 (7) (2013) 1251–1264, URL <https://onlinelibrary.wiley.com/doi/abs/10.1002/pssb.201248476>.
- [46] Z. P. Yin, K. Haule, G. Kotliar, Kinetic frustration and the nature of the magnetic and paramagnetic states in iron pnictides and iron chalcogenides, *Nature Mat.* 10 (2011) 932 – 935.
- [47] A. Georges, L. d. Medici, J. Mravlje, Strong Correlations from Hund’s Coupling, *Annual Rev. of Cond. Mat. Phys.* 4 (1) (2013) 137–178, URL <https://doi.org/10.1146/annurev-conmatphys-020911-125045>.
- [48] N. Lanatà, H. U. R. Strand, G. Giovannetti, B. Hellsing, L. de’ Medici, M. Capone, Orbital selectivity in Hund’s metals: The iron chalcogenides, *Phys. Rev. B* 87 (2013) 045122, URL <https://link.aps.org/doi/10.1103/PhysRevB.87.045122>.
- [49] E. Bascones, B. Valenzuela, M. J. Calderón, Magnetic interactions in iron superconductors: A review, *Comptes Rendus Physique* 17 (1) (2016) 36 – 59, ISSN 1631-0705, URL <http://www.sciencedirect.com/science/article/pii/S1631070515000924>.
- [50] L. de’ Medici, M. Capone, Modeling Many-Body Physics with Slave-Spin Mean-Field: Mott and Hund’s Physics in Fe-Superconductors, Springer International Publishing, Cham, ISBN 978-3-319-56117-2, 115–185, URL [https://doi.org/10.1007/978-3-319-56117-2\\_4](https://doi.org/10.1007/978-3-319-56117-2_4), 2017.
- [51] P. Werner, E. Gull, M. Troyer, A. J. Millis, Spin freezing transition and non-Fermi-liquid self-energy in a three-orbital model, *Phys. Rev. Lett* 101 (2008) 166405, URL <http://journals.aps.org/prl/abstract/10.1103/PhysRevLett.101.166405>.
- [52] J. Mravlje, M. Aichhorn, T. Miyake, K. Haule, G. Kotliar, A. Georges, Coherence-Incoherence Crossover and the Mass-Renormalization Puzzles in  $Sr_2RuO_4$ , *Phys. Rev. Lett.* 106 (2011) 096401, URL <http://journals.aps.org/prl/abstract/10.1103/PhysRevLett.106.096401>.
- [53] L. de’ Medici, J. Mravlje, A. Georges, Janus-Faced Influence of Hund’s Rule Coupling in Strongly Correlated Materials, *Phys. Rev. Lett.* 107 (2011) 256401, URL <https://link.aps.org/doi/10.1103/PhysRevLett.107.256401>.
- [54] D. Stricker, J. Mravlje, C. Berthod, R. Fittipaldi, A. Vecchione, A. Georges, D. van der Marel, Optical Response of  $Sr_2RuO_4$  Reveals Universal Fermi-Liquid Scaling and Quasiparticles Beyond Landau Theory, *Phys. Rev. Lett.* 113 (2014) 087404, URL <https://link.aps.org/doi/10.1103/PhysRevLett.113.087404>.
- [55] J. Mravlje, A. Georges, Thermopower and Entropy: Lessons from  $Sr_2RuO_4$ , *Phys. Rev. Lett.* 117 (2016) 036401, URL <https://link.aps.org/doi/10.1103/PhysRevLett.117.036401>.
- [56] T. Kroll, S. Bonhommeau, T. Kachel, H. A. Dürr, J. Werner, G. Behr, A. Koitzsch, R. Hübel, S. Leger, R. Schönfelder, A. K. Ariffin, R. Manzke, F. M. F. de Groot, J. Fink, H. Eschrig, B. Büchner, M. Knupfer, Electronic structure of  $LaFeAsO_{1-x}F_x$  from x-ray absorption spectroscopy, *Phys. Rev. B* 78 (2008) 220502, URL <https://link.aps.org/doi/10.1103/PhysRevB.78.220502>.
- [57] L. de’ Medici, Hund’s coupling and its key role in tuning multiorbital correlations, *Phys. Rev. B* 83 (2011) 205112, URL <https://link.aps.org/doi/10.1103/PhysRevB.83.205112>.
- [58] L. de’ Medici, Hund’s Induced Fermi-Liquid Instabilities and Enhanced Quasiparticle Interactions, *Phys. Rev. Lett.* 118 (2017) 167003, URL <https://link.aps.org/doi/10.1103/PhysRevLett.118.167003>.
- [59] L. de’ Medici, S. R. Hassan, M. Capone, X. Dai, Orbital-Selective Mott Transition out of Band Degeneracy Lifting, *Phys. Rev. Lett.* 102 (2009) 126401, URL <https://link.aps.org/doi/10.1103/PhysRevLett.102.126401>.
- [60] R. Yu, Q. Si,  $U(1)$  slave-spin theory and its application to Mott transition in a multiorbital model for iron pnictides, *Phys. Rev. B* 86 (2012) 085104, URL <https://link.aps.org/doi/10.1103/PhysRevB.86.085104>.
- [61] R. Yu, Q. Si, Orbital-Selective Mott Phase in Multiorbital Models for Alkaline Iron Selenides  $K_{1-x}Fe_{2-y}Se_2$ , *Phys. Rev. Lett.* 110 (2013) 146402, URL <https://link.aps.org/doi/10.1103/PhysRevLett.110.146402>.
- [62] T. Misawa, K. Nakamura, M. Imada, Ab Initio Evidence for Strong Correlation Associated with Mott Proximity in Iron-Based Superconductors, *Phys. Rev. Lett.* 108 (2012) 177007, URL <https://link.aps.org/doi/10.1103/PhysRevLett.108.177007>.
- [63] E. Bascones, B. Valenzuela, M. J. Calderón, Orbital differentiation and the role of orbital ordering in the magnetic state of Fe superconductors, *Phys. Rev. B* 86 (2012) 174508, URL <https://link.aps.org/doi/10.1103/PhysRevB.86.174508>.

- [64] L. Huang, L. Du, X. Dai, Complete phase diagram for three-band Hubbard model with orbital degeneracy lifted by crystal field splitting, *Phys. Rev. B* 86 (2012) 035150, URL <https://link.aps.org/doi/10.1103/PhysRevB.86.035150>.
- [65] L. de' Medici, G. Giovannetti, M. Capone, Selective Mott Physics as a Key to Iron Superconductors, *Phys. Rev. Lett.* 112 (2014) 177001, URL <https://link.aps.org/doi/10.1103/PhysRevLett.112.177001>.
- [66] S. Hoshino, P. Werner, Electronic orders in multiorbital Hubbard models with lifted orbital degeneracy, *Phys. Rev. B* 93 (2016) 155161, URL <https://link.aps.org/doi/10.1103/PhysRevB.93.155161>.
- [67] F. Kugler, S.-S. Lee, G. Kotliar, J. von Delft, A. Weichselbaum, to be published .
- [68] Z. P. Yin, K. Haule, G. Kotliar, Magnetism and charge dynamics in iron pnictides, *Nature Physics* 7 (2011) 294–297, URL [http://www.nature.com/nphys/journal/v7/n4/abs/nphys1923.html?lang=en?WT.ec\\_id=NPHYS-201104](http://www.nature.com/nphys/journal/v7/n4/abs/nphys1923.html?lang=en?WT.ec_id=NPHYS-201104).
- [69] A. J. Kim, H. O. Jeschke, P. Werner, R. Valentí, J Freezing and Hund's Rules in Spin-Orbit-Coupled Multiorbital Hubbard Models, *Phys. Rev. Lett.* 118 (2017) 086401, URL <https://link.aps.org/doi/10.1103/PhysRevLett.118.086401>.
- [70] S. Hoshino, P. Werner, Superconductivity from Emerging Magnetic Moments, *Phys. Rev. Lett.* 115 (2015) 247001, URL <https://link.aps.org/doi/10.1103/PhysRevLett.115.247001>.
- [71] A. Kowalski, A. Hausoel, M. Wallerberger, P. Gunacker, G. Sangiovanni, State- and superstate-sampling in hybridization-expansion continuous-time quantum Monte Carlo, arXiv:1807.00361 [cond-mat.str-el] URL <https://arxiv.org/abs/1807.00361>.
- [72] E. Bascones, M. J. Calderón, B. Valenzuela, Low Magnetization and Anisotropy in the Antiferromagnetic State of Undoped Iron Pnictides, *Phys. Rev. Lett.* 104 (2010) 227201, URL <https://link.aps.org/doi/10.1103/PhysRevLett.104.227201>.
- [73] T. Sudayama, Y. Wakisaka, T. Mizokawa, S. Ibusa, R. Morinaga, T. J. Sato, M. Arita, H. Namatame, M. Taniguchi, N. L. Saini, Doping-Dependent and Orbital-Dependent Band Renormalization in  $\text{Ba}(\text{Fe}_{1-x}\text{Co}_x)_2\text{As}_2$  Superconductors, *Journal of the Physical Society of Japan* 80 (11) (2011) 113707, URL <https://doi.org/10.1143/JPSJ.80.113707>.
- [74] F. Hardy, A. E. Böhmer, L. de' Medici, M. Capone, G. Giovannetti, R. Eder, L. Wang, M. He, T. Wolf, P. Schweiss, R. Heid, A. Herbig, P. Adelmann, R. A. Fisher, C. Meingast, Strong correlations, strong coupling, and s-wave superconductivity in hole-doped  $\text{BaFe}_2\text{As}_2$  single crystals, *Phys. Rev. B* 94 (2016) 205113, URL <https://link.aps.org/doi/10.1103/PhysRevB.94.205113>.
- [75] L. Dworin, A. Narath, Orbital Paramagnetism of Localized Nonmagnetic Impurities in Metals, *Phys. Rev. Lett.* 25 (1970) 1287–1291, URL <https://link.aps.org/doi/10.1103/PhysRevLett.25.1287>.
- [76] A. Horvat, R. Žitko, J. Mravlje, Low-energy physics of three-orbital impurity model with Kanamori interaction, *Phys. Rev. B* 94 (2016) 165140, URL <https://link.aps.org/doi/10.1103/PhysRevB.94.165140>.
- [77] M. Aichhorn, L. Pourovskii, V. Vildosola, M. Ferrero, O. Parcollet, T. Miyake, A. Georges, S. Biermann, Dynamical mean-field theory within an augmented plane-wave framework: Assessing electronic correlations in the iron pnictide  $\text{LaFeAsO}$ , *Phys. Rev. B* 80 (2009) 085101, URL <https://link.aps.org/doi/10.1103/PhysRevB.80.085101>.
- [78] K. Stadler, A. Weichselbaum, G. Kotliar, J. von Delft, Temperature-dependence of Hund metal physics, to be published .
- [79] P. Werner, S. Hoshino, H. Shinaoka, Spin-freezing perspective on cuprates, *Phys. Rev. B* 94 (2016) 245134, URL <https://link.aps.org/doi/10.1103/PhysRevB.94.245134>.
- [80] S. Florens, A. Georges, G. Kotliar, O. Parcollet, Mott transition at large orbital degeneracy: Dynamical mean-field theory, *Phys. Rev. B* 66 (2002) 205102, URL <https://link.aps.org/doi/10.1103/PhysRevB.66.205102>.
- [81] K. Inaba, A. Koga, Phase diagrams of the two-orbital Hubbard model with different bandwidths, *Phys. Rev. B* 73 (2006) 155106, URL <https://link.aps.org/doi/10.1103/PhysRevB.73.155106>.
- [82] A. Georges, G. Kotliar, W. Krauth, M. J. Rozenberg, Dynamical mean-field theory of strongly correlated fermion systems and the limit of infinite dimensions, *Rev. Mod. Phys.* 68 (1) (1996) 13.
- [83] E. Müller-Hartmann, The Hubbard model at high dimension: some exact results and weak coupling theory, *Z. Phys. B* 76 (1989) 211, URL <http://link.springer.com/article/10.1007%2FBF01312686#page-1>.
- [84] D. Bauernfeind, M. Zingl, R. Triebl, M. Aichhorn, H. G. Evertz, Fork Tensor-Product States: Efficient Multiorbital Real-Time DMFT Solver, *Phys. Rev. X* 7 (2017) 031013, URL <https://link.aps.org/doi/10.1103/PhysRevX.7.031013>.
- [85] S.-S. B. Lee, J. von Delft, A. Weichselbaum, Doublon-Holon Origin of the Subpeaks at the Hubbard Band Edges, *Phys. Rev. Lett.* 119 (2017) 236402, URL <https://link.aps.org/doi/10.1103/PhysRevLett.119.236402>.
- [86] S.-S. B. Lee, A. Weichselbaum, Adaptive broadening to improve spectral resolution in the numerical renormalization group, *Phys. Rev. B* 94 (2016) 235127, URL <https://link.aps.org/doi/10.1103/PhysRevB.94.235127>.
- [87] R. Žitko, T. Pruschke, Energy resolution and discretization artifacts in the numerical renormalization group, *Phys. Rev. B* 79 (8) 085106, URL <http://link.aps.org/abstract/PRB/v79/e085106>.
- [88] J. Hubbard, Electron correlations in narrow energy bands, *Proceedings of the Royal Society of London A: Mathematical, Physical and Engineering Sciences* 276 (1365) (1963) 238–257, ISSN 0080-4630, URL <http://rspa.royalsocietypublishing.org/content/276/1365/238>.
- [89] I. Okada, K. Yosida, Singlet Ground State of the Localized d-Electrons Coupled with Conduction Electrons in Metals, *Progress of Theoretical Physics* 49 (5) (1973) 1483–1502, URL <http://dx.doi.org/10.1143/PTP.49.1483>.
- [90] E. Walter, K. Stadler, G. Kotliar, A. Weichselbaum, J. von Delft, to be published .
- [91] X. Deng, A. Sternbach, K. Haule, D. N. Basov, G. Kotliar, Shining Light on Transition-Metal Oxides: Unveiling the Hidden Fermi Liquid, *Phys. Rev. Lett.* 113 (2014) 246404, URL <https://link.aps.org/doi/10.1103/PhysRevLett.113.246404>.
- [92] K. G. Wilson, The renormalization group: Critical phenomena and the Kondo problem, *Rev. Mod. Phys.* 47 (4) (1975) 773–840.
- [93] R. Bulla, T. A. Costi, T. Pruschke, Numerical renormalization group method for quantum impurity systems, *Reviews of*

- Modern Physics 80 (2) 395, URL <http://link.aps.org/abstract/RMP/v80/p395>.
- [94] J. von Delft, G. Zaránd, M. Fabrizio, Finite-Size Bosonization of 2-Channel Kondo Model: A Bridge between Numerical Renormalization Group and Conformal Field Theory, *Phys. Rev. Lett.* 81 (1) (1998) 196–199.
- [95] P. Sémon, K. Haule, G. Kotliar, Validity of the local approximation in iron pnictides and chalcogenides, *Phys. Rev. B* 95 (2017) 195115, URL <https://link.aps.org/doi/10.1103/PhysRevB.95.195115>.
- [96] N. Mannella, The magnetic moment enigma in Fe-based high temperature superconductors, *Journal of Physics: Condensed Matter* 26 (47) (2014) 473202, URL <http://stacks.iop.org/0953-8984/26/i=47/a=473202>.
- [97] K. M. Stadler, A. K. Mitchell, J. von Delft, A. Weichselbaum, Interleaved numerical renormalization group as an efficient multiband impurity solver, *Phys. Rev. B* 93 (2016) 235101, URL <https://link.aps.org/doi/10.1103/PhysRevB.93.235101>.
- [98] S.-S. B. Lee, J. von Delft, A. Weichselbaum, Filling-driven Mott transition in SU(N) Hubbard models, *Phys. Rev. B* 97 (2018) 165143, URL <https://link.aps.org/doi/10.1103/PhysRevB.97.165143>.
- [99] U. Schollwöck, The density-matrix renormalization group in the age of matrix product states, *Annals of Physics* 326 (1) (2011) 96 – 192, ISSN 0003-4916, URL <http://www.sciencedirect.com/science/article/pii/S0003491610001752>, january 2011 Special Issue.
- [100] F. B. Anders, A. Schiller, Real-Time Dynamics in Quantum-Impurity Systems: A Time-Dependent Numerical Renormalization-Group Approach, *Phys. Rev. Lett.* 95 (19) 196801, URL <http://link.aps.org/abstract/PRL/v95/e196801>.
- [101] F. B. Anders, A. Schiller, Spin precession and real-time dynamics in the Kondo model: Time-dependent numerical renormalization-group study, *Phys. Rev. B* 74 (2006) 245113, URL <https://link.aps.org/doi/10.1103/PhysRevB.74.245113>.
- [102] R. Peters, T. Pruschke, F. B. Anders, Numerical renormalization group approach to Green’s functions for quantum impurity models, *Phys. Rev. B* 74 (24) 245114, URL <http://link.aps.org/abstract/PRB/v74/e245114>.
- [103] W. C. Oliveira, L. N. Oliveira, Generalized numerical renormalization-group method to calculate the thermodynamical properties of impurities in metals, *Phys. Rev. B* 49 (1994) 11986–11994, URL <http://link.aps.org/doi/10.1103/PhysRevB.49.11986>.
- [104] S.-S. Lee, K. Stadler, J. von Delft, A. Weichselbaum, to be published .
- [105] R. Žitko, Adaptive logarithmic discretization for numerical renormalization group methods, *Computer Physics Communications* 180 (2009) 1271, URL <http://www.sciencedirect.com/science/article/pii/S0010465509000630>.
- [106] R. Bulla, A. C. Hewson, T. Pruschke, Numerical renormalization group calculations for the self-energy of the impurity Anderson model, *J. Phys.: Condens. Matter* 10 (1998) 8365, URL <http://iopscience.iop.org/0953-8984/10/37/021>.